National Library
of Canada

Bibliothèque nationale
du Canada

Canadian Theses Service

Service des thèses canadiennes

Ottawa, Canada
K1A 0N4

NOTICE

The quality of this microform is heavily dependent upon the quality of the original thesis submitted for microfilming. Every effort has been made to ensure the highest quality of reproduction possible.

If pages are missing, contact the university which granted the degree.

Some pages may have indistinct print especially if the original pages were typed with a poor typewriter ribbon or if the university sent us an inferior photocopy.

Reproduction in full or in part of this microform is governed by the Canadian Copyright Act, R.S.C. 1970, c. C-30, and subsequent amendments.

AVIS

La qualité de cette microforme dépend grandement de la qualité de la thèse soumise au microfilmage. Nous avons tout fait pour assurer une qualité supérieure de reproduction.

S'il manque des pages, veuillez communiquer avec l'université qui a conféré le grade.

La qualité d'impression de certaines pages peut laisser à désirer, surtout si les pages originales ont été dactylographiées à l'aide d'un ruban usé ou si l'université nous a fait parvenir une photocopie de qualité inférieure.

La reproduction, même partielle, de cette microforme est soumise à la Loi canadienne sur le droit d'auteur, SRC 1970, c. C-30, et ses amendements subséquents.

NL-339 (r. 88/04) c

Canada

UNIVERSITY OF ALBERTA

AN EXPERIMENTAL ND:YAG LASER SYSTEM

by

James A. Bauer

A THESIS

SUBMITTED TO THE FACULTY OF GRADUATE STUDIES AND
RESEARCH IN PARTIAL FULFILMENT OF THE REQUIREMENTS FOR
THE DEGREE OF MASTER OF SCIENCE

DEPARTMENT OF ELECTRICAL ENGINEERING

EDMONTON, ALBERTA

SPRING, 1991

National Library of Canada
Canadian Theses Service

Bibliothèque nationale du Canada
Service des thèses canadiennes

Ottawa, Canada
K1A 0N4

ISBN 0-315-66627-7

Abstract

The Nd:YAG (Neodymium: Yttrium Aluminum Garnet) laser has been used for some time in the fields of medicine and industry. The medical community has focused its attention primarily on the photocoagulative properties of the radiation produced by this type of laser. The industrial applications have for the most part been related to cutting, welding and similar materials processing activities. Although seemingly unrelated, there may be some crossover between the uses of the Nd:YAG laser in each field. This thesis describes the design, construction and subsequent testing of an experimental Nd:YAG laser system to be used to explore possible new uses. This experimental system provides facilities not available on commercially produced Nd:YAG laser systems.

Table of Contents

List of Tables

List of Figures

List of Photographs

1. Introduction

Laser oscillation in Nd:YAG (Neodymium: Yttrium Aluminum Garnet) was first observed by Geusic, Marcos and Van Uitert in 1964 [5]. In the years since, this crystal has become possibly the most widely used solid-state laser material available [1,2]. This is due to the remarkable combination of advantageous optical properties with several essential thermal and mechanical qualities. As a result of its popularity, the properties of this laser crystal have been exhaustively studied by numerous authors [1,2,6-21]. Commercial Nd:YAG laser systems with output powers ranging from less than one watt to several hundreds of watts are available. In general though, these units are rather application specific and as such do not lend themselves well experimental use.

The applications of Nd:YAG lasers have been primarily in the fields of medicine and industry. The industrial applications have for the most part been related to cutting, welding, and related materials processing activities. The medical community has focused its attention primarily on the photocoagulative properties of the standard 1.06μm radiation produced by this type of laser. Although seemingly unrelated, there is some crossover between the uses of the Nd:YAG laser in each field. The technique of using high peak power pulses for cutting and welding metals and other materials should prove to be similarly useful for cutting and welding biological tissue.

In addition, the availability of high peak powers will allow for experimentation with some of the lower gain transitions which have been

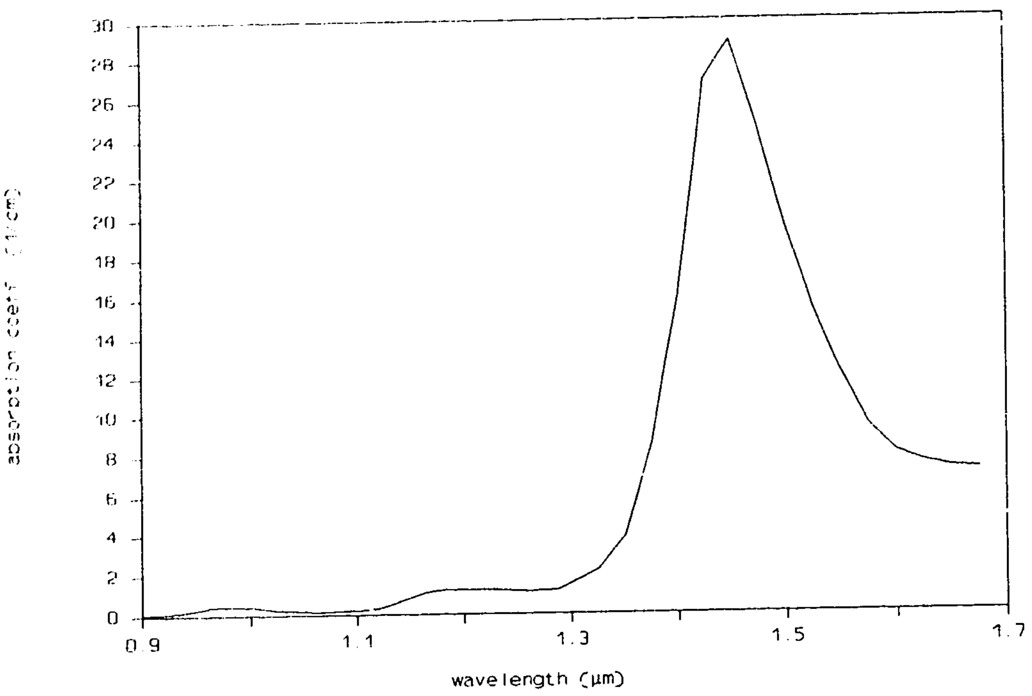

Figure 1.0.1: Absorption coefficient of water in the region of radiation produced by Nd:YAG laser.

identified in Nd:YAG [2,6,12-16]. One transition in particular produces radiation at a wavelength of 1.44μm which corresponds almost exactly with a major absorption peak of water. As water is the significant component of most biological tissue, it is proposed [33] that if this laser line can be made to oscillate, the Nd:YAG should prove to be an effective surgical laser as well as an established photocoagulator . Figure 1.0.1 illustrates the dramatic increase in the absorption coefficient of radiation in the 0.9 to 1.7μm region for water.

This thesis describes the design, construction and subsequent evaluation of an experimental Nd:YAG laser system which is to be used to explore possible new uses. This experimental laser system provides facilities not available on commercially available Nd:YAG laser systems. As shown in Figure 1.1.2, the basic laser system is composed of several interconnected subsystems.

1) Main Power Supply
2) Control Electronics
3) Support Subsystems
    - Cooling
    - High Voltage and Simmer
4) Laser Head Assembly

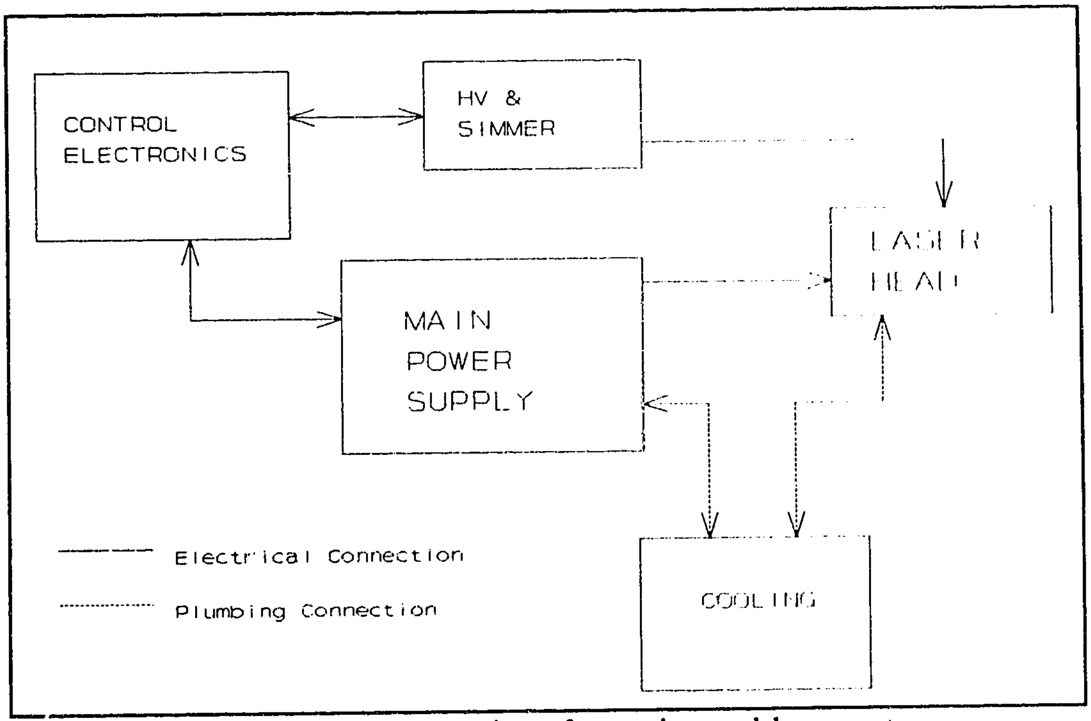

Figure 1.1.2: schematic representation of experimental laser system

The major enhancement provided by this experimental system is a versatile main power supply which is capable of delivering high peak power electrical pulses to the laser flashlamp. Conventional pulsed Nd:YAG lasers are driven via a pulse forming network to control the amplitude and width of the output pulse.

This technique is cumbersome when it comes to varying the pulse parameters in that it involves the physical replacement of the storage elements in the pulse forming network. In this experimental system the main power supply has the ability to interrupt the drive current directly allowing for easy control of the widths of the output pulses. In addition, the power supply can drive the laser in a continuous wave (CW) mode of operation.

When connected to the laser head, the output power range available in the CW mode is from 0 - 100 W at the standard 1.06μm wavelength. In pulsed mode the average output power is comparable to that in CW mode and the pulse width and repetition rate are controllable by the user. The nominal pulse rate varies from approximately 5 - 50 Hz at a 1:10 duty cycle corresponding to a peak output power at 1.06μm of approximately 1kW. The laser head assembly has been developed with flexibility towards future experiments in mind. The modularity of the design allows for the addition of various other apparatus such as Q-switches, frequency doublers and other modifications.

Similarly, the control circuitry necessary to operate the system has been designed to maximize ease of modifications. It was decided early in the project that a discrete controller rather than one based around a microcomputer, would be more suitable for the experimental nature of this system.

Each of the subsystems is discussed in detail in the following chapters.

2. Power Supply

2.1 Introduction

For the purposes of this project, a power supply capable of operating in a repetitive, high peak power pulse mode as well as a low ripple D.C. continuous mode is required. To this end, a "chopper" power supply was chosen. A chopper circuit basically switches a D.C. supply to the load as shown in Figure 2.1.1.

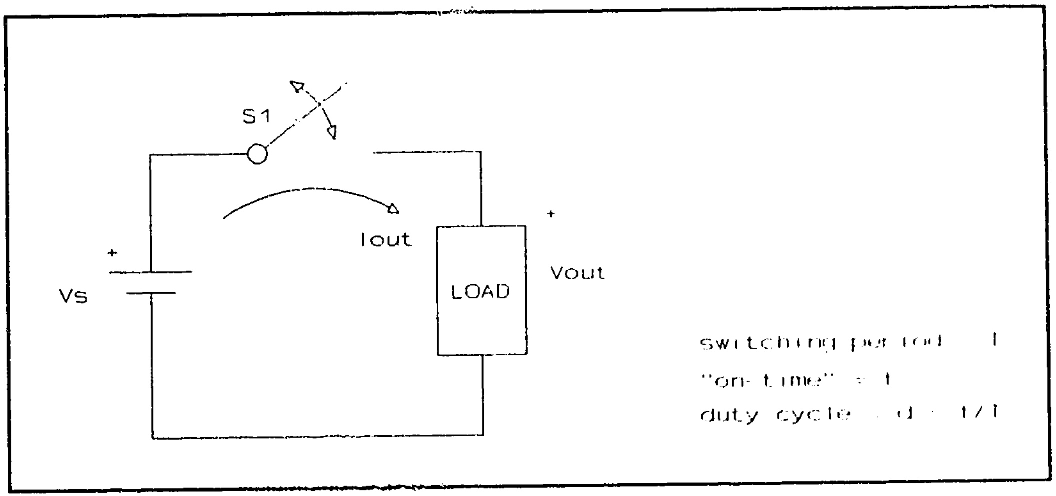

Figure 2.1.1: chopper - switch analogy

This switching will modulate the voltage at a particular duty cycle which in turn determines the average voltage at the load. By varying this duty cycle, whether by maintaining a fixed chopping frequency and varying the "on-time" or by fixing the "on" pulse duration and varying the operating frequency, the output voltage may be set to a chosen value. In order to realize the continuous mode of operation, the output can be smoothed by a simple LC filter. To keep these filter elements physically small, high frequency operation in continuous mode is advantageous. For pulse mode operation, the filter is switched out and the pulse width can be increased to provide the higher peak power required, as long as the maximum average power conditions are not exceeded. Figure 2.1.2 demonstrates the differences in output waveforms for the two operating modes.

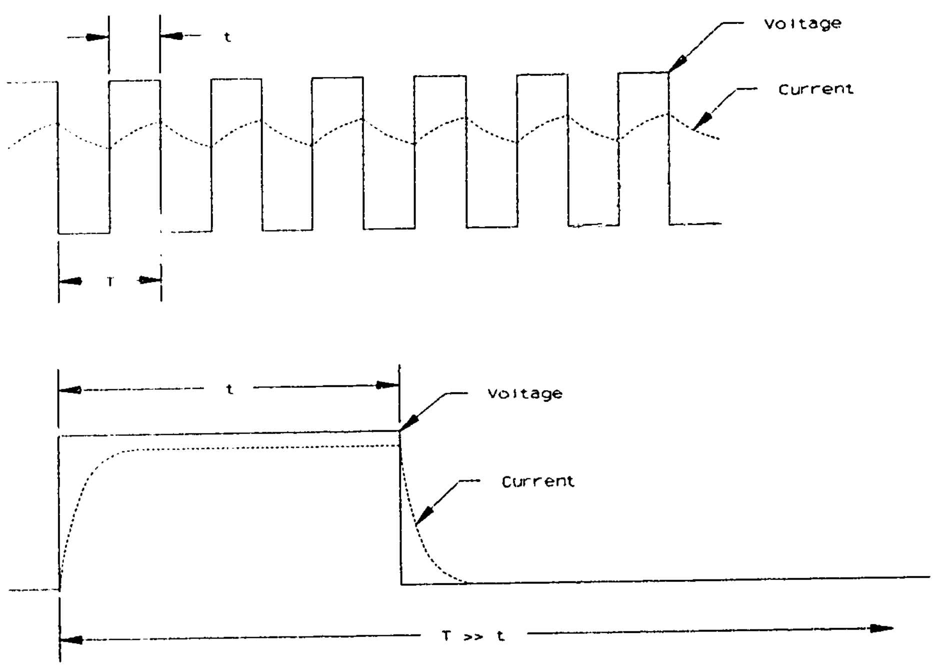

Figure 2.1.2: generic CW/Pulse waveforms (CW upper, Pulse lower)

This chapter outlines fundamental thyristor concepts pertinent to the design of such a circuit. This is followed by the design procedure and calculations for the power supply used in the experimental system. The performance of the power supply in the laser system is then discussed.

2.2 General thyristor (SCR) concepts

A thyristor, or for that matter a rectifier, can be considered simply to be nothing more than a switch. It is helpful, though, to distinguish between the various types of solid-state switches[34]. The first type, or basic solid-state switch, is commonly known as the diode or rectifier. This type of switch will conduct automatically when forward biased and will cease to conduct when reverse biased. With a switch of this type, there is no mechanism for controlling the point at which the switch is "turned-on". The second type of switch provides this element of control, and is thus often referred to as a silicon controlled rectifier (SCR). SCRs do not conduct when forward biased until they are initiated to do so by an external control signal. After this instant they behave in the same manner as an uncontrolled rectifier and can be "turned-off" only by being reverse biased. The third type of solid-state switch adds another level of control in that the forward current can be interrupted by the application of a control signal rather than requiring the device to be reverse biased. This class of solid-state switches includes transistors (bipolar and FET) and gate turn off thyristors (GTOs).

Ideally, the latter type of switch would meet the requirements of the power supply required for this project. At the present time unfortunately, devices of this type are costly, difficult to coordinate in their switching, and typically do not have the necessary power handling capabilities at high enough frequencies for this project. However, a circuit composed of switches of type two (SCRs) can be made to operate as a switch of the third type through a method of forced commutation. This is the method of control used in the power supply for this project, and is discussed in a following section.

The generic term *thyristor* refers to a solid-state device which behaves in the same fashion as a thyratron tube. This includes all solid-state devices which have two or more junctions, and are switchable between conducting states within at least one quadrant of the principal V-I curve. There are two common types of thyristors. The first is the reverse-blocking triode thyristor, commonly referred to as the SCR. The second type is the bidirectional triode thyristor, usually called a triac. The scope of this project will concentrate on the former type of thyristor, the SCR.

In its simplest realization, the SCR contains three internal p-n junctions in series, as illustrated in Figure 2.2.1.

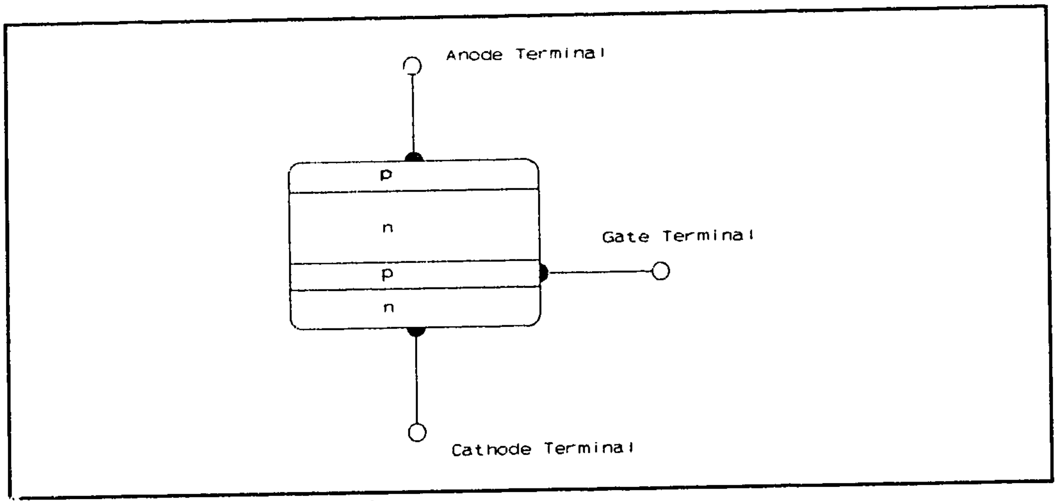

Figure 2.2.1: SCR block diagram

When the SCR is reverse biased (ie: anode negative with respect to the cathode), the centre junction is forward biased while the outer two junctions are reverse biased. This means that the SCR will block reverse current until the breakdown voltage of these outer junctions is exceeded. Similarly, when the SCR

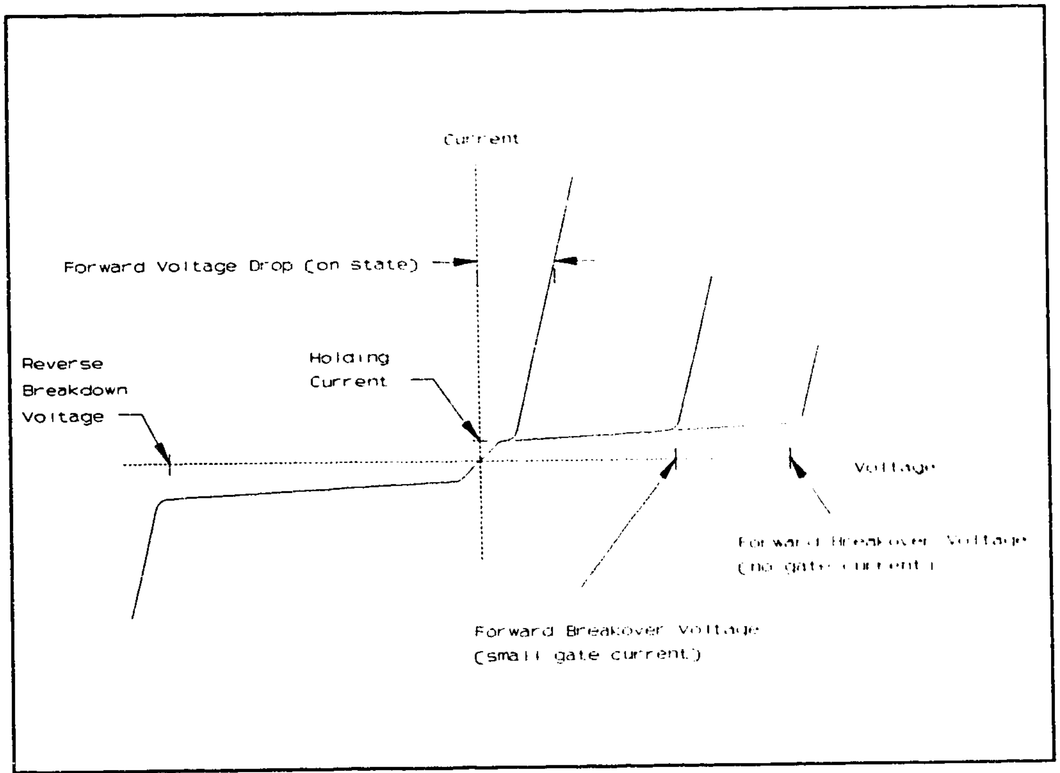

Figure 2.2.2: SCR steady-state V-I characteristics

is forward biased (ie: anode positive with respect to cathode), the outer junctions are forward biased but the centre junction is now reverse biased. Thus, the SCR will also block the forward current until the forward breakdown voltage is surpassed. If the gate terminal is made positive with respect to the cathode while the SCR is still forward biased, current will begin to flow through this junction. This current in turn initiates a regenerative internal action which allows current to flow across the reverse biased centre junction. Once forward current flow has been established, the device latches "on" until it is commutated by an external means.

The steady-state V-I characteristic curve for a generic SCR is shown in Figure 2.2.2. The reverse blocking state is very similar to that of a conventional rectifier, as is, by symmetry, the forward blocking characteristic. However, with the application of a gate current, the forward breakdown voltage is reduced and the SCR can "switch on" if the applied voltage exceeds this lower value.

2.3 Transient Considerations

When designing a commutating circuit it is necessary to have an understanding of how the devices being switched behave as they change state. There are several excellent manuals available which cover the many transitional parameters in great detail[1]. For the purpose of this thesis, however, only the "turn-on time" and the "turn-off time" will be discussed in any detail. The reader is however, encouraged to refer to these manuals for a more in depth discussion of the many other constraints involved in the switching of thyristors.

When a thyristor is directed to turn on by the application of a gating current pulse, there is a finite period of time until the device has in fact, turned on. As the device is turning on, the current is initially confined to a small area of the semiconductor pellet. With time, this area spreads (typically at a rate in the order of 0.1 mm/ μsec) until the entire thyristor area is conducting the forward current. This time period is referred to as the total turn-on time, t_{gt} and is comprised of two stages; a delay time t_d, and a rise time t_r, the relationship of which is shown in Figure 2.3.1.

While the turn-on time is somewhat dependent on the maximum off-state voltage and the maximum on-state current, the major dependency is on the magnitude of the gating current pulse. This stands to reason, in that as the gate current is increased, the area of the semiconductor pellet which is initially conducting will become larger. If the current density at the junction becomes

---

[1] - for example: RCA Solid-State Devices Manual, RCA Corporation, 1975.

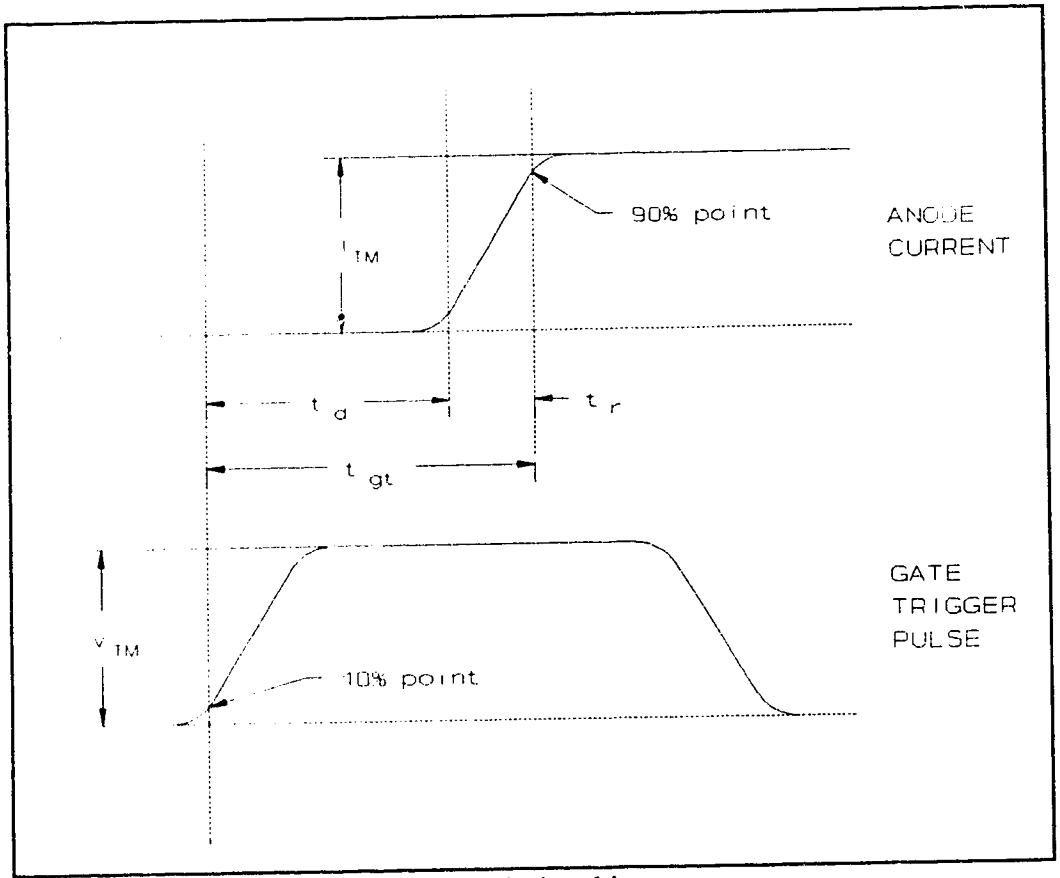

Figure 2.3.1: SCR turn-on timing relationship

excessive during the turn-on time, severe thermal stresses can be applied to the junction and if they are great enough, permanent damage will result. This critical current density, in conjunction with the turn-on time, will determine the limiting rate of current change, which is often referred to as the maximum allowable di/dt. To ensure that this maximum di/dt is not exceeded, a series inductance is often incorporated in the circuit design to limit the rate of change in the thyristor forward current.

The concept of turn-off time is of particular significance when considering the design of a circuit employing a forced commutation mechanism. As with the turn-on time, there are two stages associated with turning off a SCR. The first turn-off stage is referred to as the reverse recovery time t_{rr}, and the second, the gate recovery time t_{gr}. The relationship between t_{rr}, t_{gr} and the commutated turn-off time t_q, is illustrated in Figure 2.3.2.

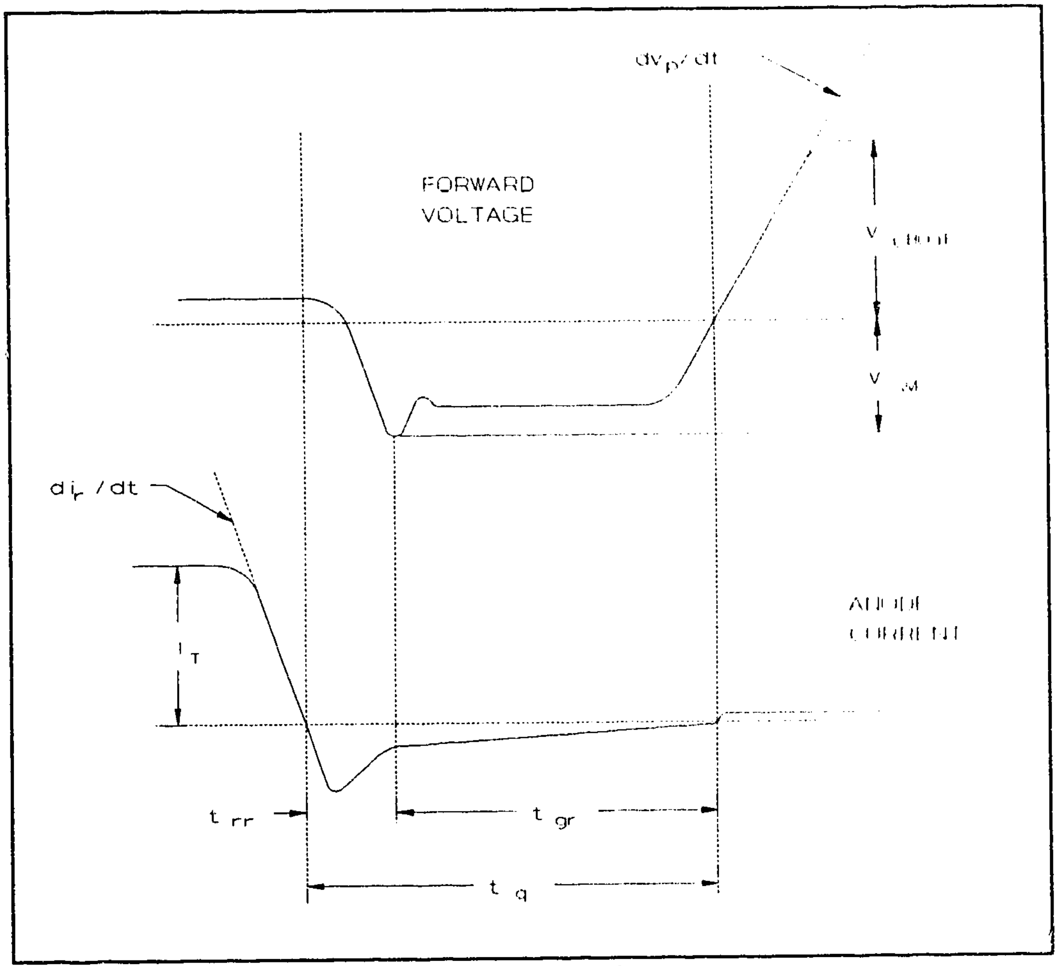

Figure 2.3.2: SCR turn-off timing relationship

When a junction that has been conducting a forward current is suddenly reverse biased, it will conduct in the reverse direction for a period of time due to the carriers which persist at the reverse blocking junction. The reverse recovery time is the time required to remove these carriers and establish a depletion region after this junction becomes reverse biased. Similarly, the gate recovery time is the time required to re-establish a depletion region at the centre (forward blocking) junction of the SCR. Typically, the gate recovery time is much greater than the reverse recovery time. Any re-application of a forward bias before the turn-off time has passed may lead to an unwanted re-firing of the SCR.

It is also important to note that the forward blocking junction is susceptible to unwanted firing due to a rapid change in the forward applied voltage. This junction forms a capacitance which can cause a current to be injected into the gate layer as:

$$i = C_j \, dv/dt \tag{2.1}$$

This injected current will behave as an externally applied gate current. Thus, if the SCR is forward biased and the dv/dt is greater than the maximum allowed, the device may fail to remain in its blocking state. The dv/dt experienced by the device can be reduced by the incorporation of a shunt R-C network often called a "snubber". The capacitor will limit the dv/dt seen by the device and the resistor will serve to limit the di/dt introduced by the capacitor. Suitable values of resistance and capacitance are often recommended by SCR manufacturers to provide a balance of allowable dv/dt, added di/dt and dissipation by the snubber.

2.4 Development of the VICC topology

As shown above, in order to turn off an SCR it is necessary to apply a reverse bias for a period of time which is at least as long as the turn-off time of the device. A simple way to do this would be to connect a capacitor which is charged to an appropriate voltage, as shown in Figure 2.4.1.

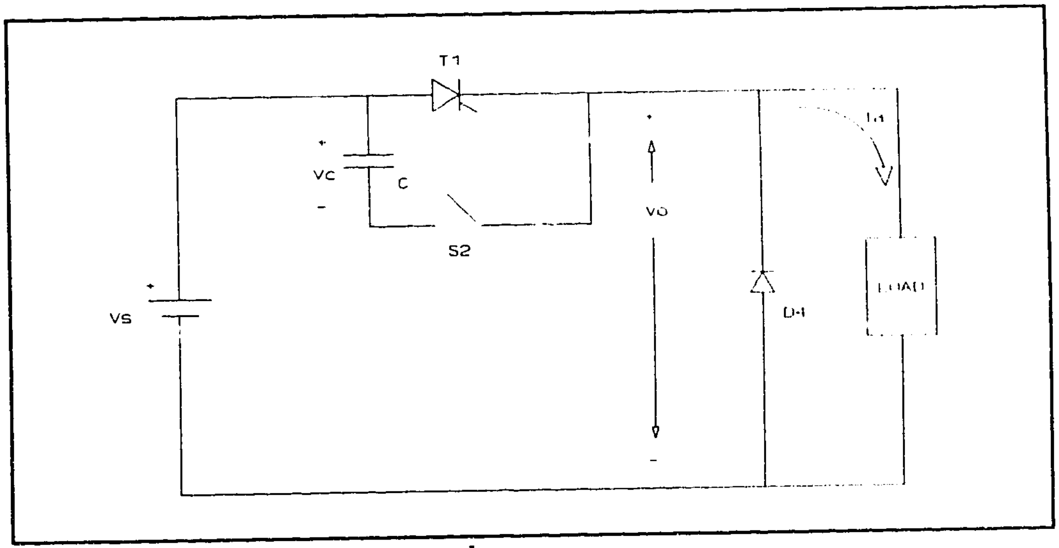

Figure 2.4.1: initial chopper topology

In this simplified example, it must be assumed that initially T_1 is conducting the load current I_a and that somehow the capacitor , C, has been charged to $V_{co} = -V_s$. When the switch is closed, T_1 is reverse biased by the capacitor and the current through T_1 will cease. However, for any realistically inductive load, the load current must continue to flow as determined by the value of L_{LOAD}. If this load inductance is sufficiently large to ensure that the load current can be considered to be constant over the commutation period, the capacitor voltage during this cycle will be described by:

$$V_c = -V_{co} + I_a t / C \qquad (2.2)$$

The SCR will be reverse biased only while the capacitor voltage is negative so, the turn-off time available to the SCR will be the time required for V_c to reach zero:

$$t_r = V_s C / I_a \tag{2.3}$$

For the circuit shown, the charging of the capacitor will continue until Vc $= +V_s$ (that is, $V_o = 0$) at which time the freewheeling diode D_4 will conduct the load current which is still flowing as L_{LOAD} would require.

Although at this point commutation has been achieved and the SCR is turned off, it would presumably be the case that one would want to repeat the cycle in order to effect some continuous control of the load. To accomplish this, some method of reversing the charge (ie: $V_{co} = -V_s$) on the capacitor is required. One such method would be to introduce an L-C resonant circuit to reestablish the negative charge on C when T_1 is re-fired.

Figure 2.4.2 illustrates how this L-C circuit may be incorporated. Now, when T_1 is fired to once again supply current to the load, an underdamped resonant path C-T_1-L_2-D_2 is formed. T_1 and D_2 will limit the direction of the current flow in this loop and as such the capacitor current will be a half-sinusoid. At the end of the charge reversal cycle the capacitor voltage will reverse to $V_c = -V_s$, assuming that there are no losses. Typical waveforms for the commutation and charge reversal cycles are shown in Figure 2.4.3.

The duration of the charge reversal cycle covers the period when there is current flowing in the capacitor, which is:

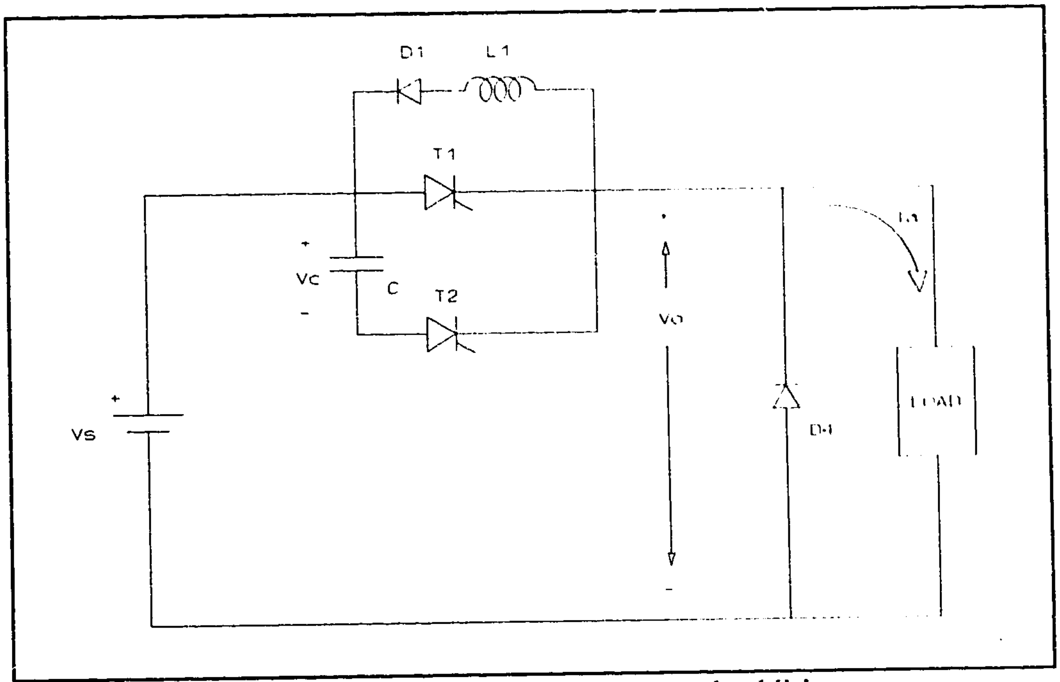

Figure 2.4.2: chopper topology with charge reversal addition

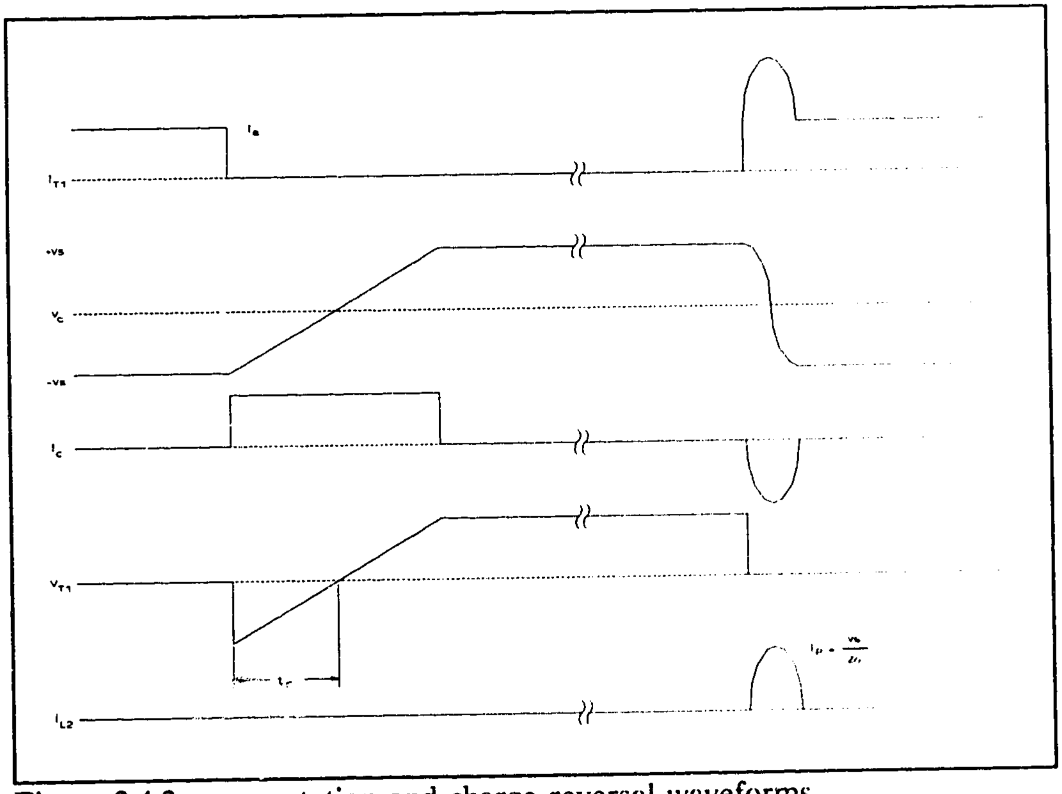

Figure 2.4.3: commutation and charge reversal waveforms

$$t_{REV} = \pi(LC)^{1/2} \tag{2.4}$$

and is independent of the load current. However, this is not the case for the total commutation time for the above circuit. During the commutation cycle the current flows in the capacitor for:

$$t_{COMM} = 2\,C\,V_s / I_a \tag{2.5}$$

which can be seen to become quite large for small values of load current. It would therefore be advantageous to employ a resonant circuit similar to that used in the charge reversal cycle in order to minimize this dependency on load current. The final chopper topology is shown in Figure 2.4.4 and the associated commutation and charge reversal waveforms are shown in Figure 2.4.5.

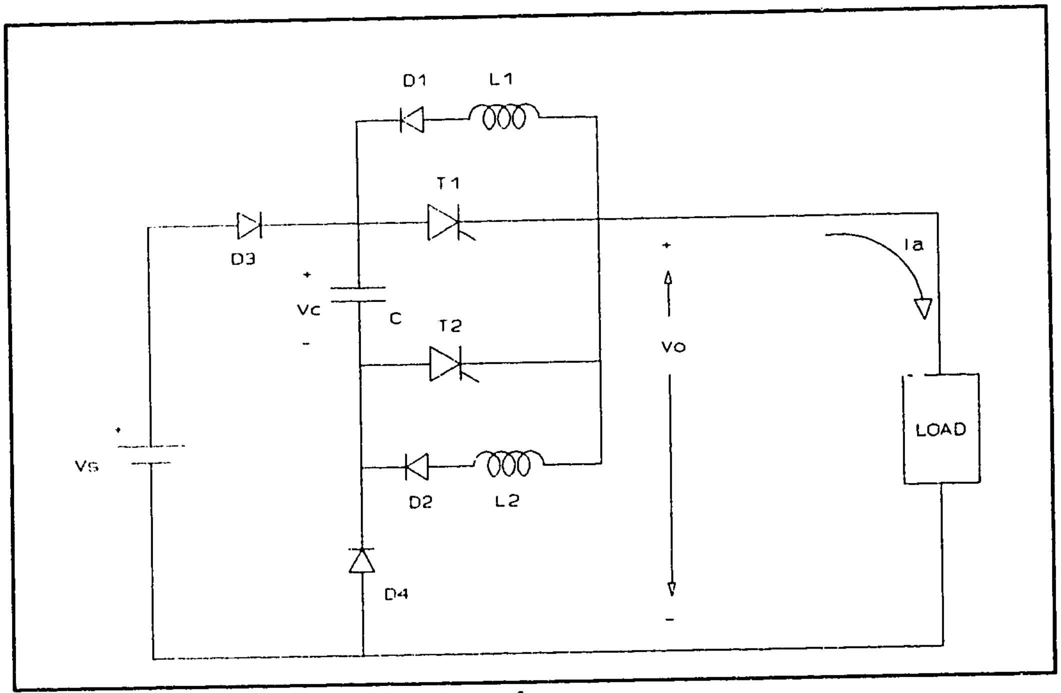

Figure 2.4.4: improved chopper topology

Consider now what takes place during one complete cycle for the circuit developed above. This time however, the cycle will begin from a so called "cold-start". That is, there is no established load current yet, and the commutation

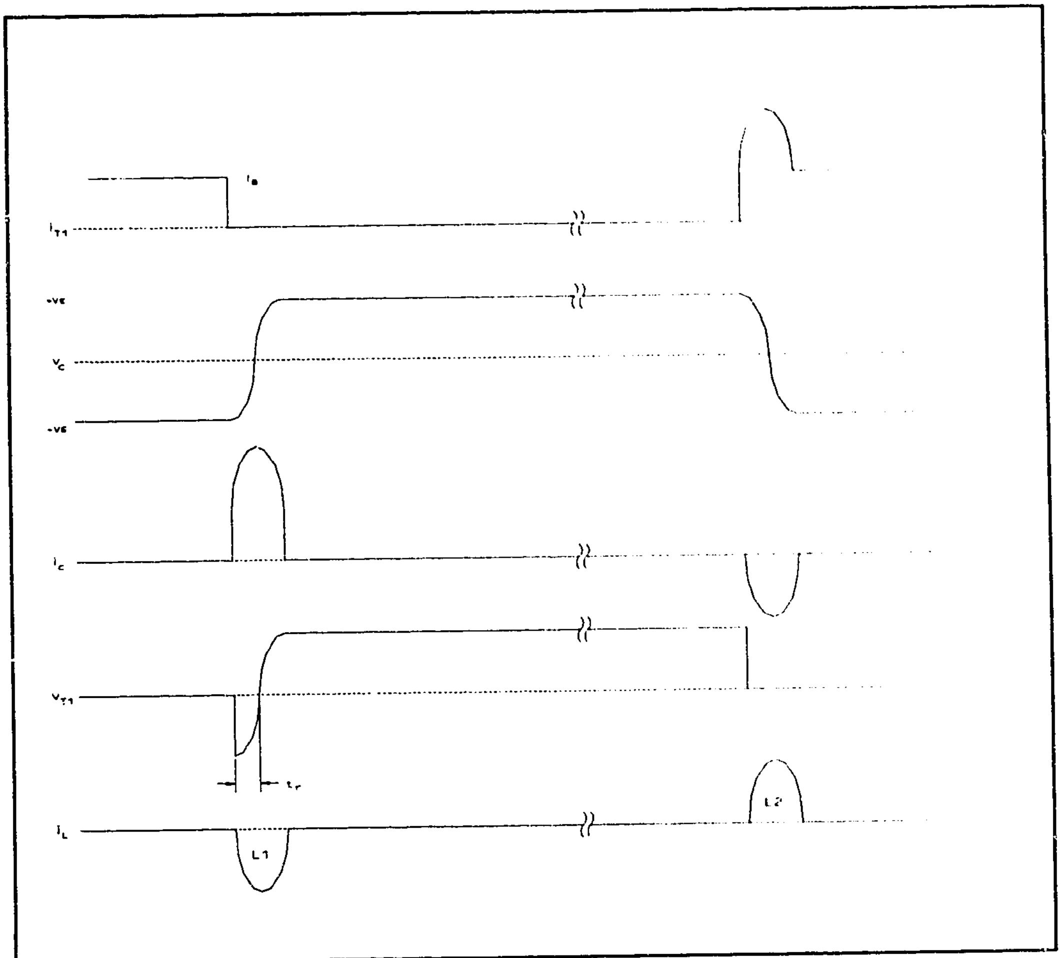

Figure 2.4.5: improved commutation and charge reversal waveforms

capacitor is not yet charged. Therefore, in order to start, T_2 must be turned on long enough to ensure that C_c has charged to $v_c = V_s$. With the capacitor now appropriately charged, T_1 can be turned on. Immediately T_2 is reverse biased and the load current is supplied through T_1. A resonant current pulse will flow through L_{c2}, D_2, C_c and T_1 to reverse the charge on C_c. When the current through D_2 and L_{c2} reaches zero, C_c stops charging and $v_c = -V_s$. This completes the charge reversal cycle. The chopper is now in the "on" state with T_1 supplying the load current from the source. The commutation cycle may now be initiated by triggering T_2. This applies a reverse bias to T_1, and now a resonant current

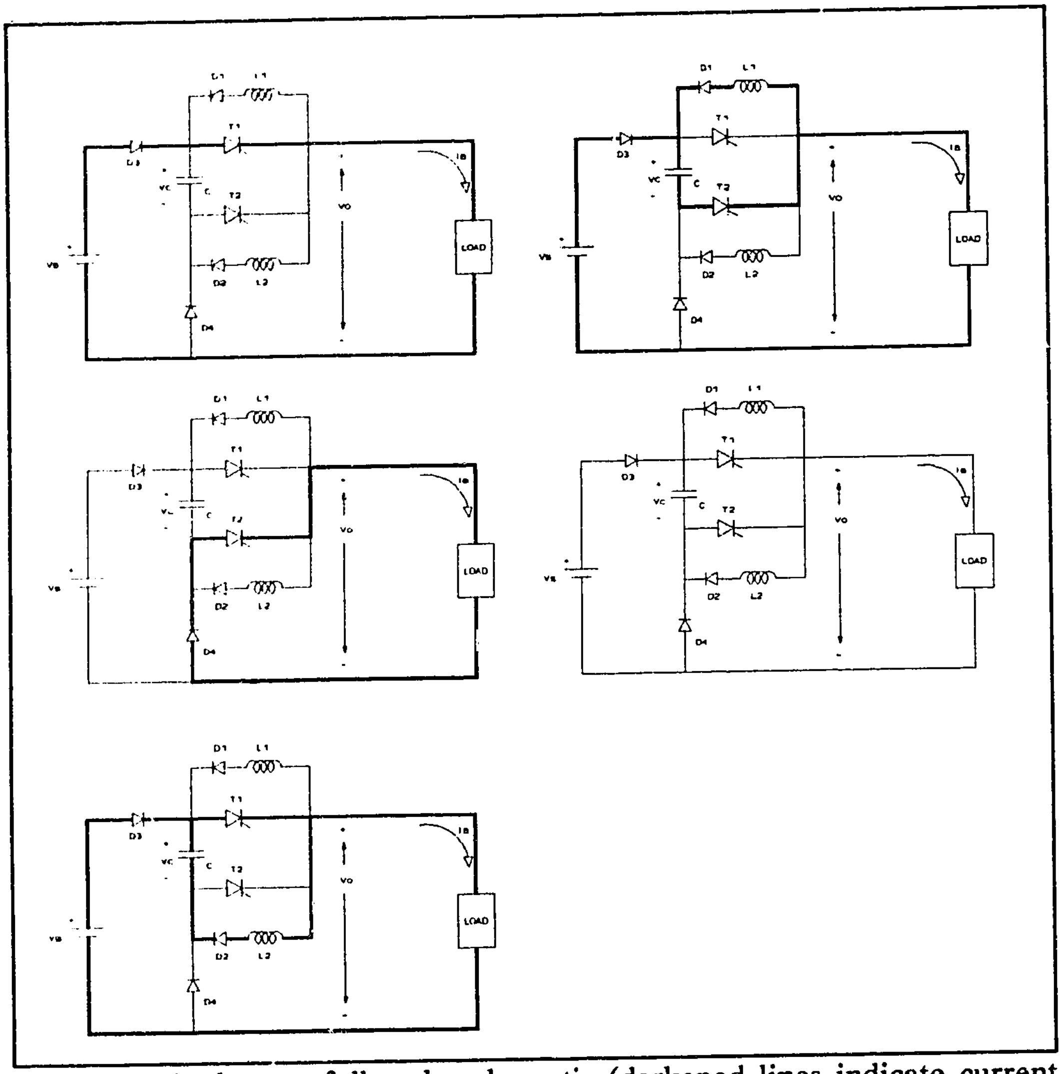

Figure 2.4.6: chopper full cycle schematic (darkened lines indicate current paths)

pulse flows through L_{c1}, D_1, C_c and T_2 to once again reverse the charge on C_c. The output voltage jumps to $V_o = V_s + (-v_c) = 2V_s$ when T_2 is fired, which then falls to zero as C_c continues to charge to $v_c = V_s$. This concludes the commutation cycle and the chopper is now in the "off state". The load current may continue to flow once again through the freewheeling diode D_4 as L_{load} requires. The next complete cycle can be commenced by triggering T_1 as before. The above process is represented schematically in Figure 2.4.6.

2.5 Design calculations

In order to establish the design equations for this chopper circuit, it will be necessary to break the total operating cycle down into its two main parts and look at the equivalent circuits for each. First, consider the charge reversal cycle. The equivalent circuit is shown in Figure 2.5.1.

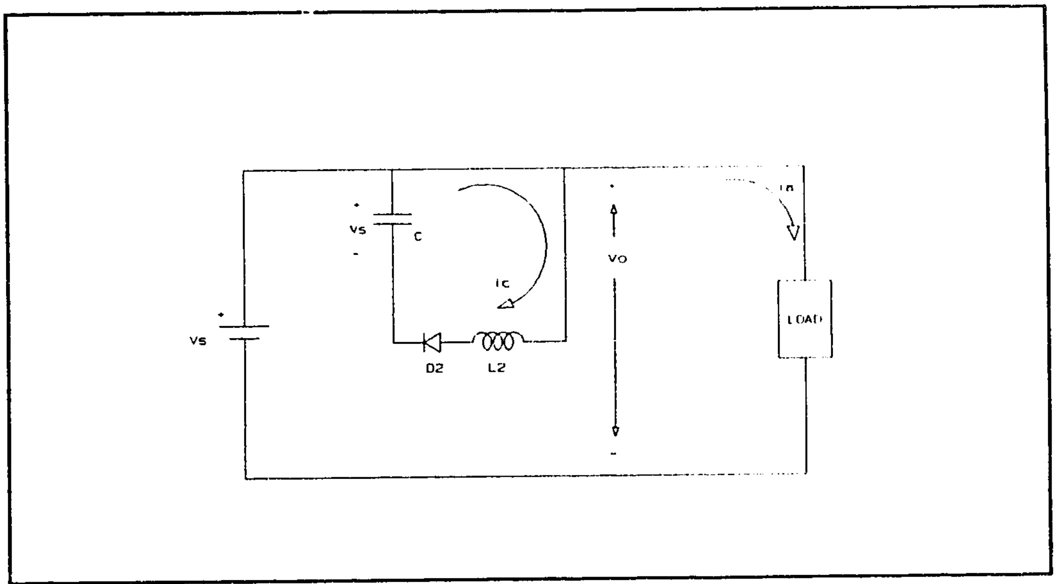

Figure 2.5.1: equivalent circuit for charge reversal cycle

For this circuit:

$$i_c = -C\,dv_c/dt = i_l,\; v_c = L\,di_l/dt \tag{2.6}$$

From which it follows that:

$$LC\,d^2v_c/dt^2 + v_c = 0 \tag{2.7}$$

Which has a solution of the form:

$$v_c = A\cos(w_0 t) + B\sin(w_0 t) \tag{2.8}$$

Thus:

$$i_c = Aw_oC \sin(w_ot) + Bw_oC \cos(w_ot) \qquad (2.9)$$

If the initial conditions are applied to solve for the constants A and B:

$$i_c(0^+) = 0 \;;\; B = 0$$

$$v_c(0^+) = V_s \;;\; A = V_s \qquad (2.10)$$

Finally:

$$v_c = V_s \cos(w_ot),\; i_c = V_sw_oC \sin(w_ot) = V_s /Z_o \sin(w_ot) \qquad (2.11)$$

Where:

$$Zo = (L/C)^{1/2},\; w_o = (LC)^{-1/2} \qquad (2.12)$$

The diode D_2 will block any reverse current ,so, the charge reversal cycle will end at:

$$w_ot_{cr} = \pi,\; v_c(\pi) = -V_s \qquad (2.13)$$

Next, consider the commutation cycle. The equivalent circuit for this cycle is shown in Figure 2.5.2.

Now:

$$i_c = i_l + I_a = C\, dv_c /dt,\; v_c = -L\, di_l /dt \qquad (2.14)$$

So that:

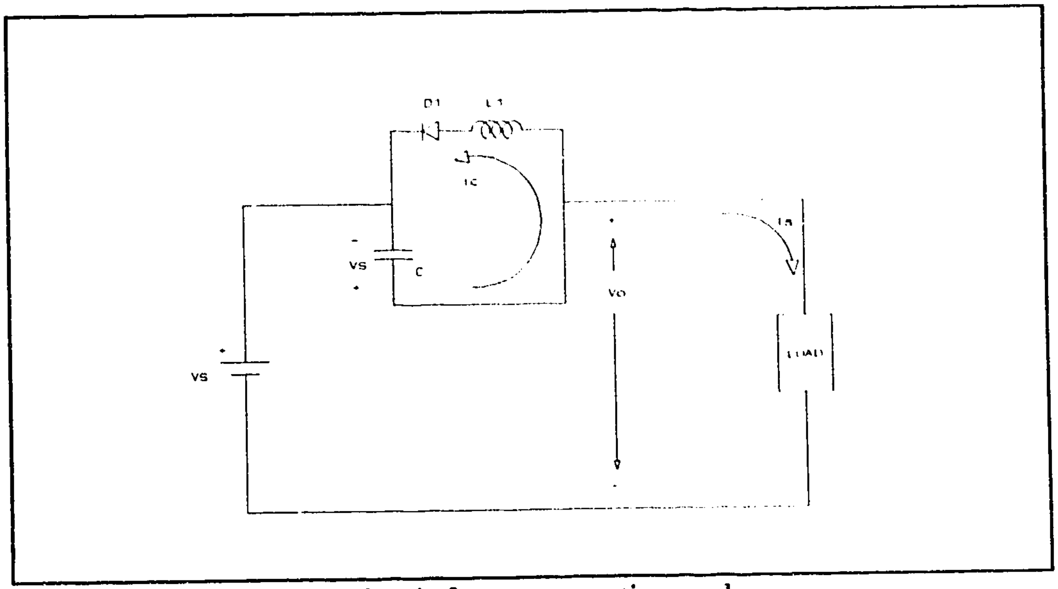

Figure 2.5.2: equivalent circuit for commutation cycle

$$v_c = -LC\, d^2v_c/dt^2 \qquad (2.15)$$

And again:

$$v_c = A\cos(w_0t) + B\sin(w_0t) \qquad (2.16)$$

With:

$$i_c = Aw_0C\sin(w_0t) + Bw_0C\cos(w_0t) \qquad (2.17)$$

Applying the initial conditions now yields:

$$v_c(0^+) = -V_s\,;\ A = -V_s$$

$$i_c(0^+) = I_a\,;\ B = I_a/(w_0C) = Z_0I_a \qquad (2.18)$$

So:

$$v_c = -V_s\cos(w_0t) + I_aZ_0\sin(w_0t) \qquad (2.19)$$

$$i_c = V_s/Z_o \sin(w_o t) + I_a \cos(w_o t) \tag{2.20}$$

$$i_l = V_s/Z_o \sin(w_o t) + I_a \{\cos(w_o t) - 1\} \tag{2.21}$$

From the above it can be seen that the recovery time available to the SCR is the time for $v_c < 0$. At t_r, $v_c = 0$. So,

$$V_s \cos(w_o t_r) = I_a Z_o \sin(w_o t_r) \tag{2.22}$$

Which leads to:

$$t_r = (LC)^{1/2} \tan^{-1}\{V_s/(I_a Z_o)\} \tag{2.23}$$

The commutation cycle ends when $i_l = 0$ (ie: $i_c = I_a$). So for the total mode time t_T:

$$-V_s/Z_o \sin(w_o t_T) = I_a \{\cos(w_o t_T) - 1\} \tag{2.24}$$

From which it can be found that:

$$t_T = (LC)^{1/2} \cos^{-1}\{(i_o^2-1)/(i_o^2+1)\} \tag{2.25}$$

Where:

$$i_o = I_a Z_o / V_s \tag{2.26}$$

The ideal case would be that at t_T, $i_c = I_a$ and $v_c = +V_s$. Since there is little if any variation in the load current in this application, an optimum i_o can be established by setting $v_c(t_T) = +V_s$. This procedure yields:

$$i_{oopt} = I_a / V_s \text{ (ie: } Z_o = 1) \tag{2.27}$$

Now, with this parameter and the above equation for t_r, the necessary commutation circuit design equations can be set out:

$$L = V_s t_r / I_a \, i_o / \tan^{-1}(1/i_o) \tag{2.28}$$

$$C = I_a t_r / V_s \, 1/i_o \tan^{-1}(1/i_o) \tag{2.29}$$

With, $i_o = i_{oopt}$ and t_r being the thyristor specified turn-off time.

For this project, it was determined that the power supply should be capable of delivering 300 A pulses from a 300 V source. The thyristors selected have a turn-off time of 20 μsec (the SCR and rectifier specifications are further discussed in the following section). This indicates an i_{oopt} of 1 and the values of L and C of:

$$L = 25.5\ \mu\text{H}$$

$$C = 25.5\ \mu\text{F}$$

2.6 Construction

Until this point the chopper has been considered as an independent, first order circuit. This is of course, not the case. The chopper is the central element of the main power supply but is not "free standing" and is composed of many components not indicated in the preceding discussion. Figure 2.6.1 is the complete schematic for the power supply used in this project.

The uncontrolled six pulse bridge (D_{a1} - D_{c2}) will rectify the incoming three phase voltage to a D.C. voltage with an average value of

$$V_{outavg} = 3\sqrt{3}/\pi \; V_p = 3\sqrt{3}/\pi \; (120\sqrt{2}) = 280 \text{ V} \tag{2.30}$$

and a peak of

$$V_{outpk} = \sqrt{3} \; V_p = 293 \text{ V}. \tag{2.31}$$

The rectifiers chosen for this bridge were International Rectifier 40HF60, 40Aavg, 600V devices. Capacitor bank C_1 is implemented to supply the peak current required during pulse mode. The capacity necessary was determined such that the bank voltage would not drop to less than 75% of its nominal value during the longest anticipated pulse. As a preliminary design value, a maximum allowable pulse width of 20 msec was selected. The load was found to have a dynamic resistance of roughly 1.2 Ω. From these criteria it can be calculated that a capacitor bank of 57.9 mF would be needed. To accomplish this, 40 x 1500 μF @ 450 Vdc Mallory HES series capacitors were used. This series is ideal for

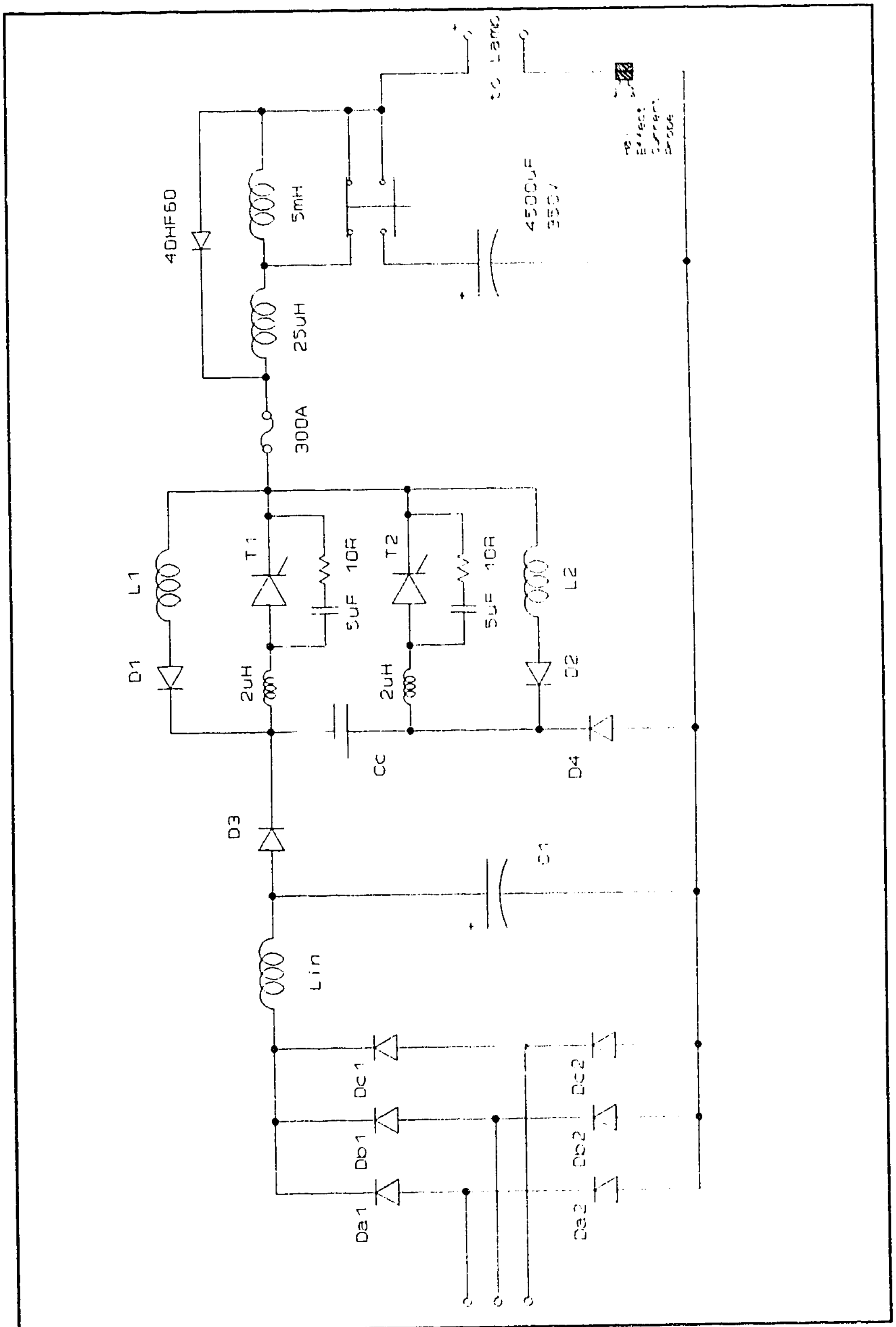

Figure 2.6.1: V.I.C.C. power supply schematic

pulse delivery due to a very low internal resistance. The bank capacitors were connected together using copper strapping for mechanical rigidity and low electrical losses. This capacitor bank was sufficiently large so as to also provide very good regulation for the continuous operating mode. Inductor L_1 is required to limit the initial charging current to C_1 and to reduce the line current surges in pulse mode. For this experimental system $L_1 = 5$ mH.

For the chopper section of the power supply, Westinghouse semiconductors were chosen. This was in part due to the relative availability from this manufacturer but the main consideration was the fast switching times claimed at the power levels of interest. While it is true that thyristor T_1 is the primary load carrying device, T_2 must also be able to handle the resonant switching current and in fact it must also carry the full load current for an interval during the commutation cycle. The main SCR must also be capable of conducting a continuous current pulse of 300 A for 20 msec at a repetition rate of 5 Hz. However, the maximum peak current through T_1 occurs during the commutation cycle and is the sum of the established load current and the peak resonant capacitor current. In the experimental system, this would indicate a peak primary thyristor current of 600 A. Based on this and the appropriate trapezoidal current pulse data available, T_1 and T_2 were selected to be Westinghouse T727063584DN fast switching SCRs. These are 600 V., 350 A. avg. thyristors with a specified 10 μsec turn-off time. The design value of a turn-off time of 20 μsec was used to ensure a wide margin of safety. To provide adequate cooling in as little space as possible, the SCRs were factory mounted in water cooling assemblies (the overall cooling strategy is discussed in detail in a following chapter). To specify the freewheeling and the chopper isolation diodes it is necessary to calculate the associated rms current involved. In pulse mode the output current is basically a square wave pulse train with a fixed duty cycle. For a pulse train of this type the rms value is simply:

$$i_{rms} = Ipk \sqrt{d} \qquad (2.32)$$

where d is the duty cycle. In this experimental system, the duty cycle was set at 1/10, that is, 20 msec ON at a rate of 5 Hz (T = 200 msec) this duty cycle is to be maintained at the higher repetition rate of 50 Hz so that the minimum pulse mode ON time is 2 msec. Therefore, the load current will have an rms value of 95 A. Data for trapezoidal current pulses were not available for the Westinghouse fast recovery rectifiers, so a selection was made to ensure the maximum performance of these devices was not exceeded. Westinghouse R6020625HSYA Soft-Fast recovery rectifiers were chosen for D_3 and D_4.

The current pulse amplitudes in each of the resonant loops are, for the most part, independent of the load current (see section 2.5 above). Therefore, in the case of the rectifiers required in these loops, the most severe stresses will occur in the continuous operating mode, when the highest operating frequencies are attained. For this mode then, the current pulse is a half sinusoid of width:

$$\tau = T/2 = \pi(LC)^{1/2} = 80\ \mu\text{sec} \qquad (2.33)$$

with a repetition rate of 1 kHz. Now

$$i_{rms} = I_{pk} \sqrt{(d/2)} \tag{2.34}$$

which corresponds to an rms current of roughly 60 A. Thus for the resonant loop clamping rectifiers, D_1 and D_2, Westinghouse R5020618FSWA Soft-Fast recovery rectifiers were chosen.

The 25 μF commutation capacitor, C_c, was assembled from five Westinghouse 26F6734FC 5 μF/1000V inverter grade capacitors in parallel. These capacitors were connected together using copper strapping.

The two 25 μH commutation inductors, L_1 and L_2, were fabricated from 27 turns of 3/8" copper tube on a 6" radius (air core). Copper tubing was used to limit the dissipation expected in continuous mode. Each inductor was constructed on an acrylic frame, which kept the windings isolated and provided mechanical stability.

The inherent symmetry of the voltage impulse commutated chopper helped to make the construction of this section very straightforward. The chopper module was built up on both sides of an 18" x 24" sheet of 3/8" phenolic. Where possible, components were connected directly together rather than with connecting wires. This was also done to limit dissipation and any noise associated with the large instantaneous current involved. When connecting wires could not be avoided, #2 awg welding cable was used with soldered, crimp type lugs. Brass rather than steel hardware was used throughout this module for all electrical connections. The completed chopper module is shown in photographs 2.6.1 - 4.

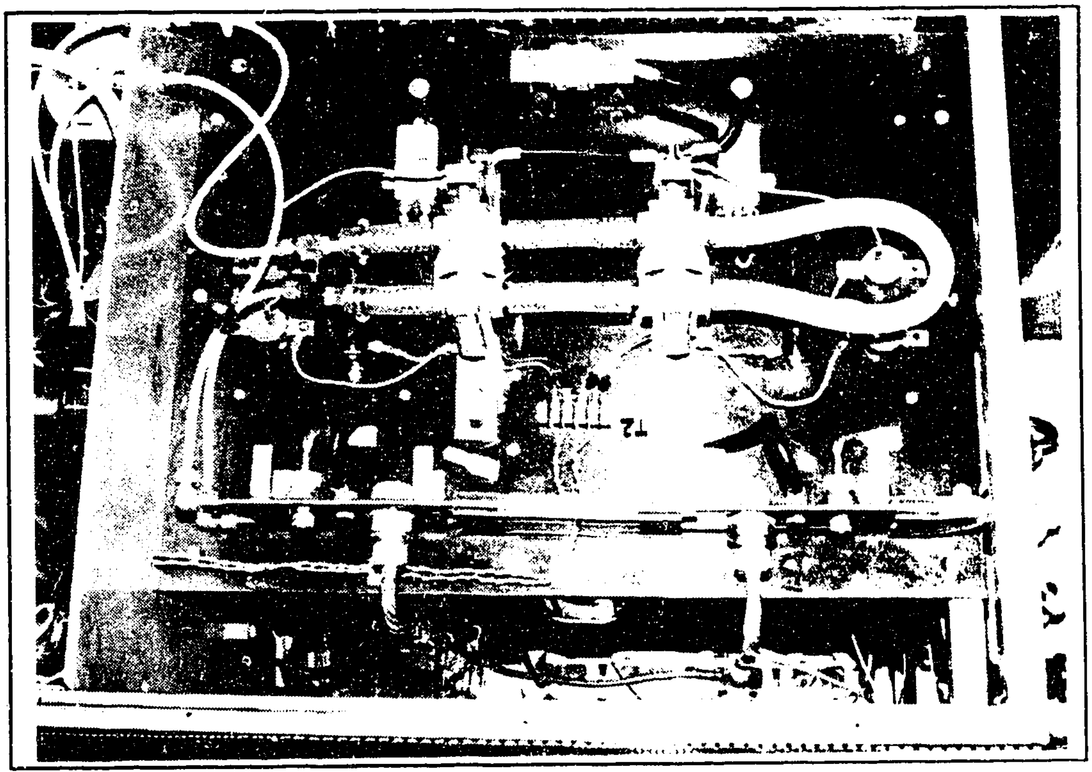

Photograph 2.6.1: power supply subassembly, top view.

Photo 2.6.1 shows a view from the top of the power supply module. Thyristors T1 and T2 are the large "hockey-puk" style devices in the centre of the picture. The gate drive signal wires can be seen coming onto the module from the left and connected at the terminal strip close to the main SCRs. The snubber capacitors and resistors as well as the over-voltage protection varistors are also mounted in close proximity to the devices. The commutation and free-wheeling diodes can be observed in the lower part of the photo. The cooling hoses are clearly identifiable on both SCR and diode heatsinks. The main output fuse is also shown at the top of the photo. In addition, a portion of the main capacitor bank can be seen below the phenolic circuit board at the bottom of the picture.

Photo 2.6.2 shows the module again from a different angle. In this photo the interconnection between components is perhaps better illustrated.

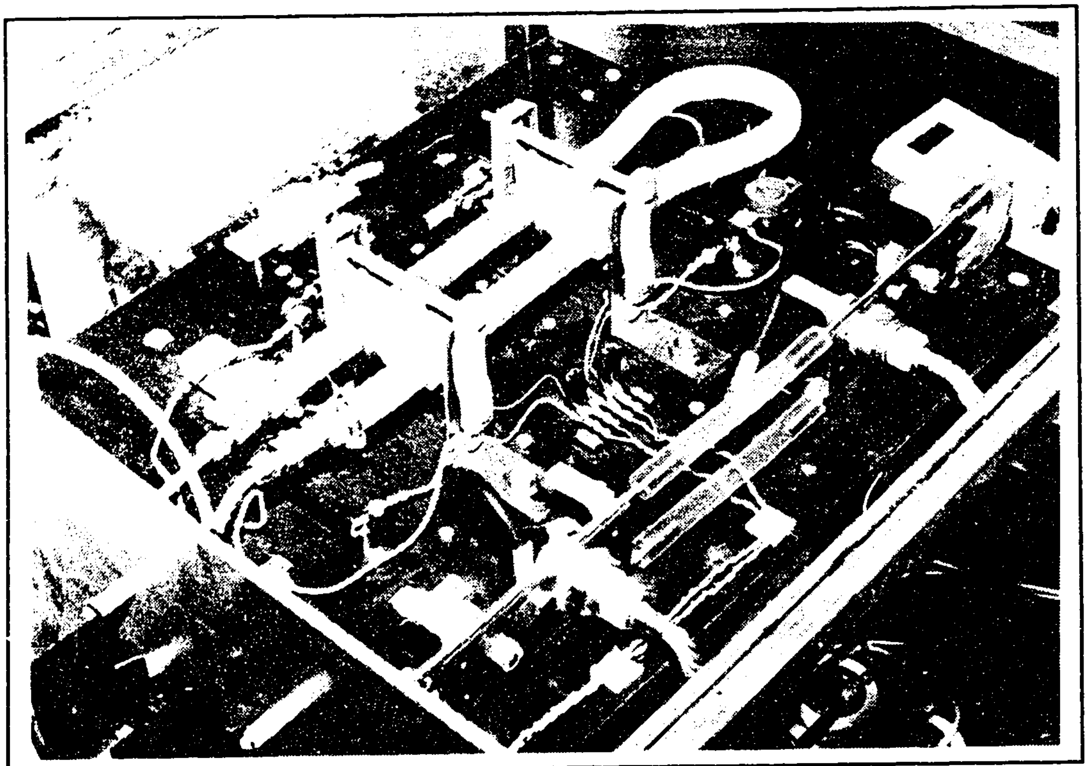

Photograph 2.6.2: power supply subassembly, alternate view.

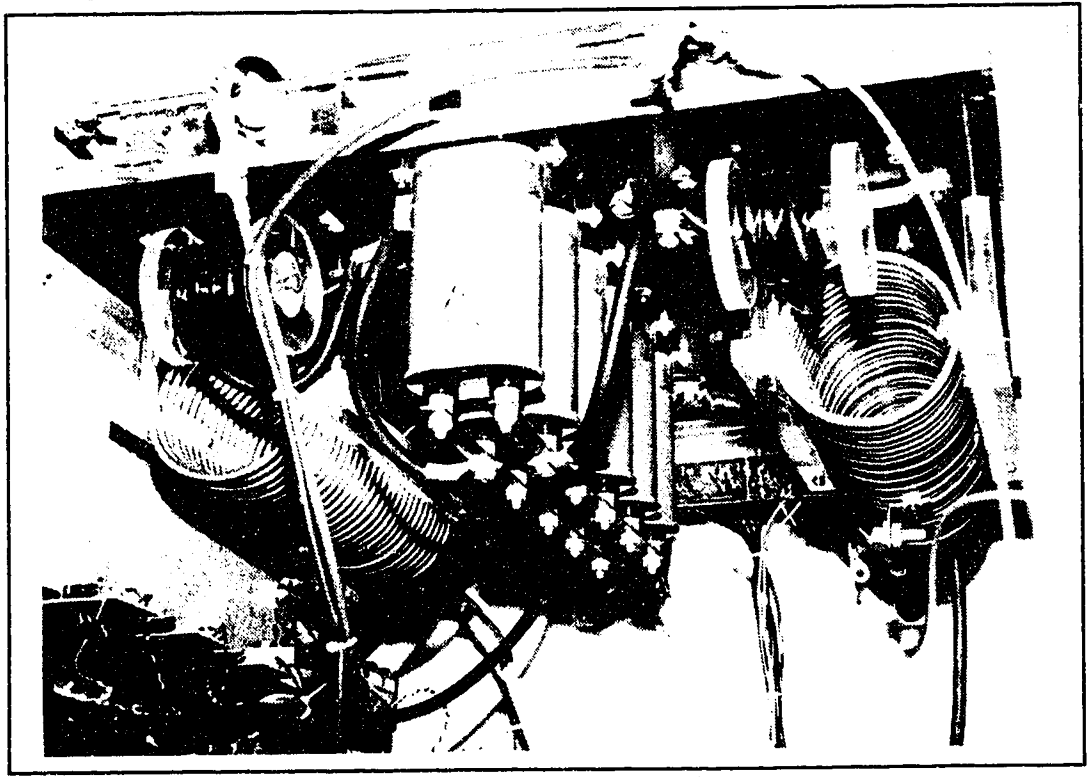

Photograph 2.6.3: power supply module, bottom view.

Connections from one side of the circuit board to the other are made via brass hardware which in most cases also provides the mechanical connection to the phenolic board.

This type of connection is once again shown in photograph 2.6.3. From this view, the commutation circuit elements are clearly seen, with the capacitor bank in the centre and the large copper tubing wound inductors at either side. The smaller snubber inductors are located in front of the commutation inductors. The main diode bridge can be seen at the bottom left of this photo.

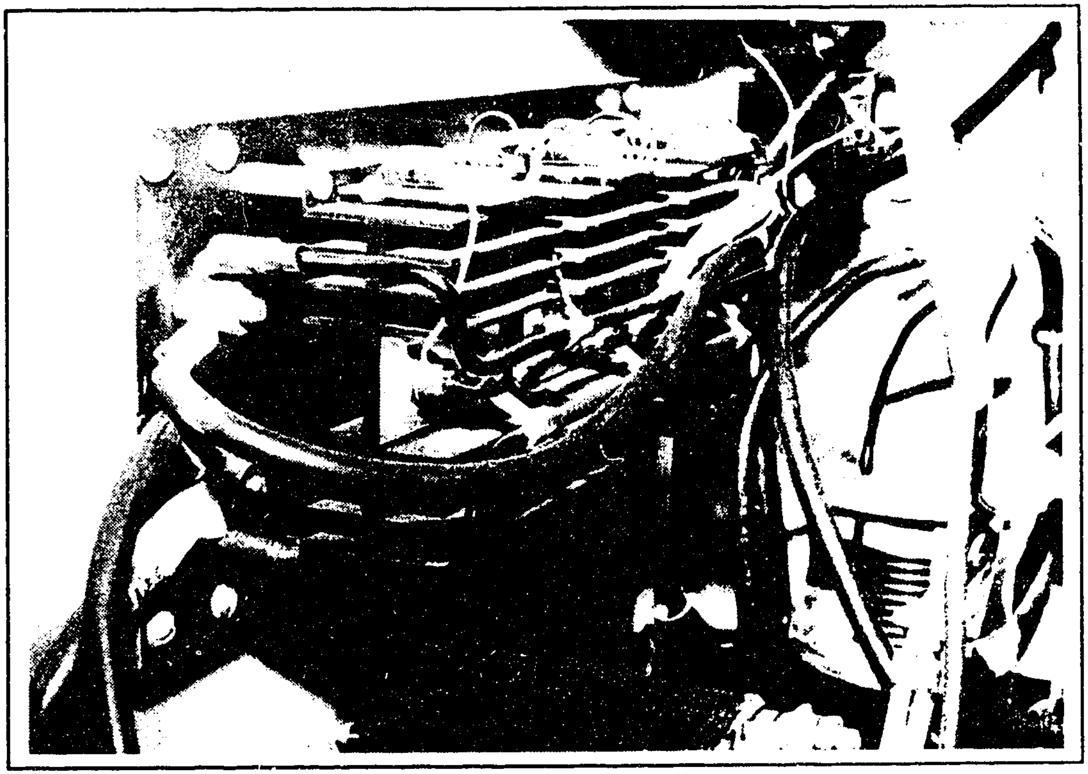

Photograph 2.6.4: three phase diode bridge detail.

Photograph 2.6.4 provides a close-up view of this sub-module. As can be seen, the bridge assembly is a free standing unit which can be easily removed for testing and modifications. Small snubber boards can be seen mounted to the tops of the heatsinks of each diode pair.

2.7 Power Supply Performance

The load for this power supply is an ILC L-2733 Krypton arc lamp inside the laser head. Following chapters deal with the necessary control and support signals required to accomplish this. However, for the purposes of this chapter, it will be assumed that the power supply is being appropriately controlled and that the lamp is running and well cooled.

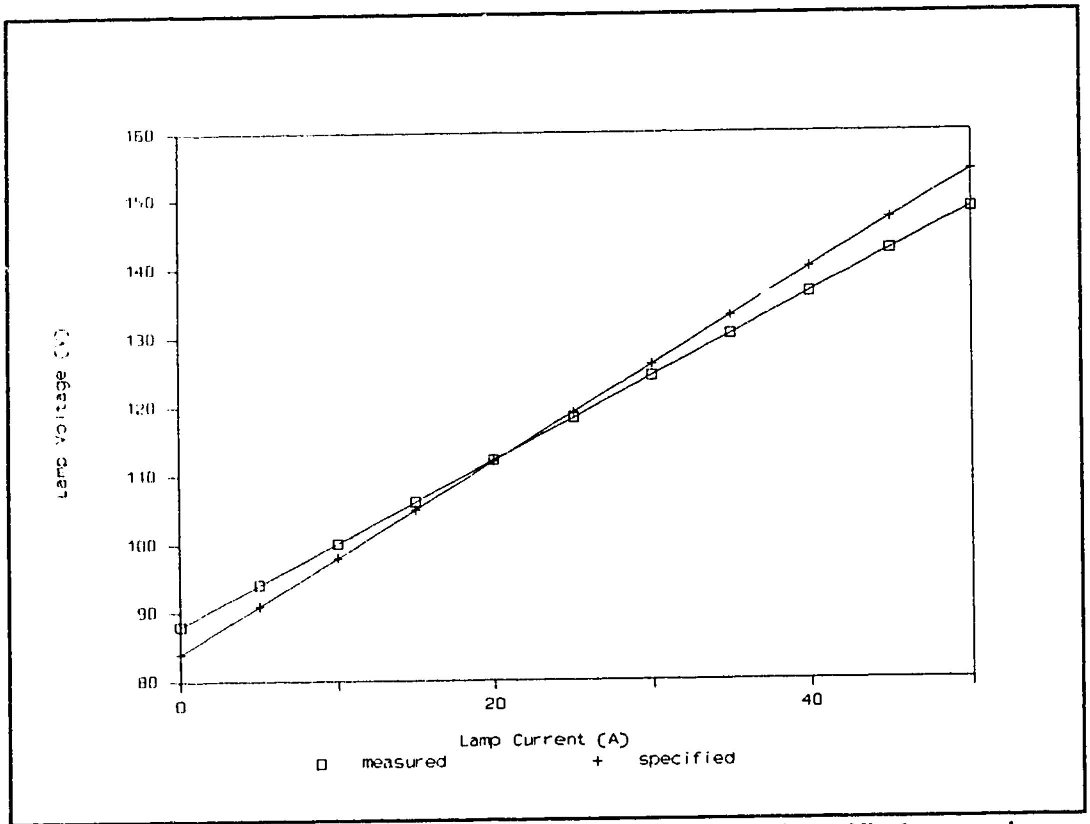

Figure 2.7.1: V-I characteristics of ILC L-2733 arc lamp. (specified operation as per ILC bulletin #1215)

The basic V-I response for the lamp used in the system is shown in Figure 2.7.1. The completed power supply was connected to this lamp and the operation of the overall power supply was then evaluated.

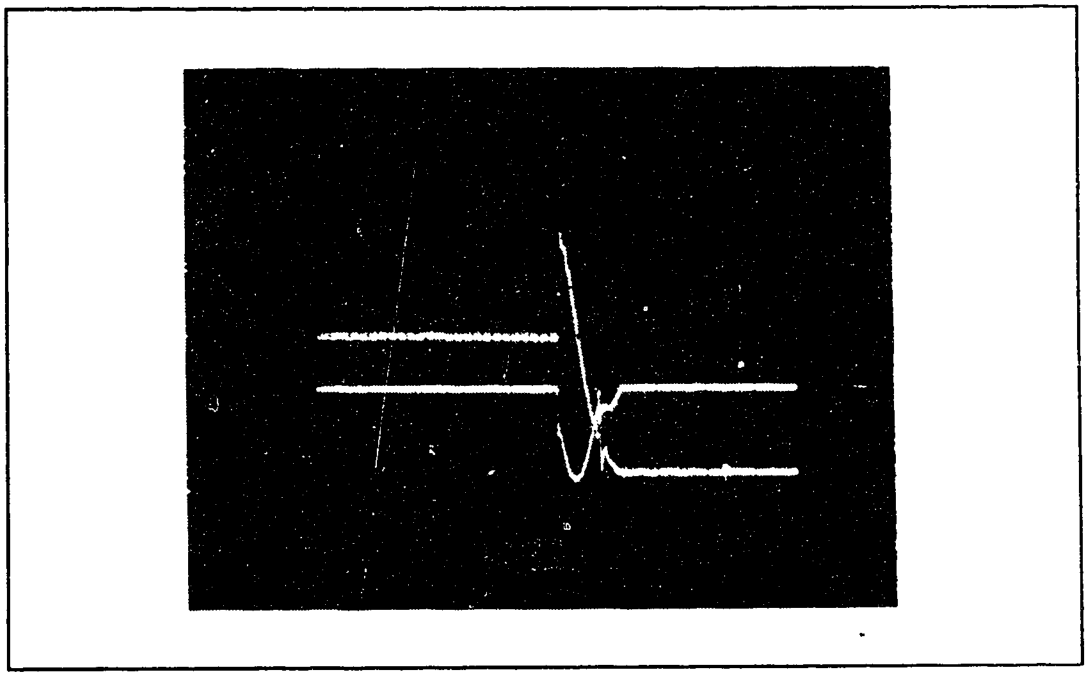

Photograph 2.7.1: SCR T1 voltage and commutation current during commutation cycle. VT1: 100V/div, Icc: not calibrated, t: 50μsec/div.

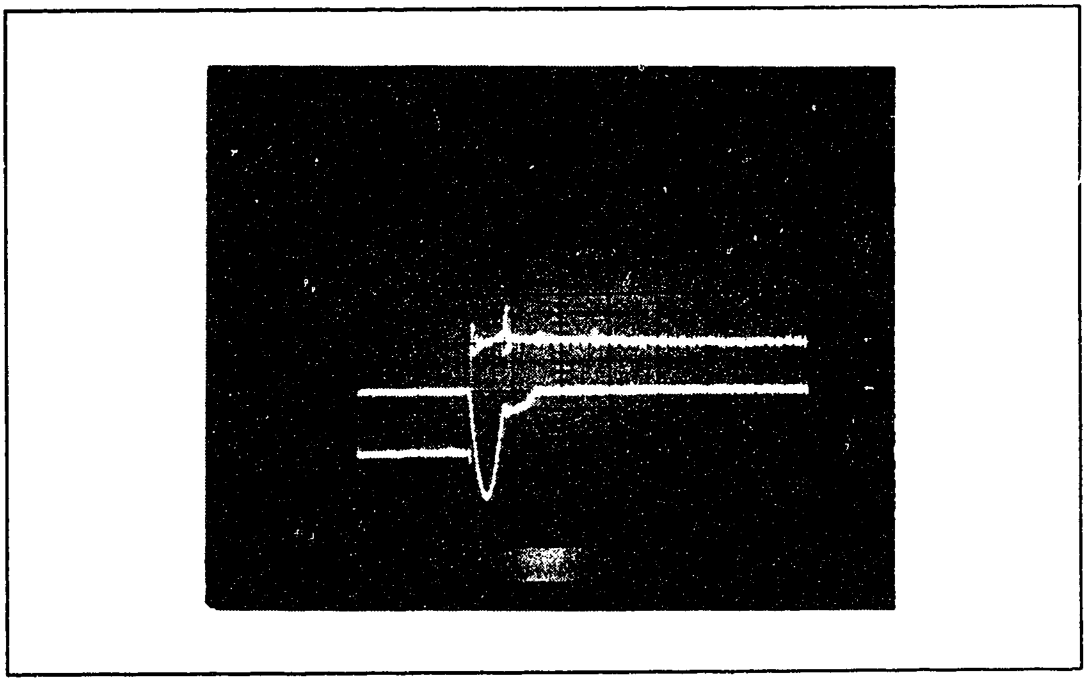

Photograph 2.7.2: SCR T2 voltage and commutation current during commutation cycle. VT2: 100V/div, Icc: not calibrated, t: 50μsec/div.

Photographs 2.7.1 and 2.7.2 show the voltages present on the two main devices during the commutation cycle. The polarities of the waveforms are reversed from those shown in Figure 2.4.5. This is due to the connection of the instrumentation. It is clear from photo 2.7.1 that the available reverse recovery time is at the design value of 20μsec. The "lump" on the capacitor current pulse is evidence that the commutation capacitor is supplying some of the load current through T_2 as T_1 is being turned off. It was observed during this evaluation that if the 25μH output inductor was removed, the effective impedance of the load was significantly reduced such that the resonant charging loop was, in effect, being shorted. This resulted in the commutation capacitor being discharged, which led to commutation failure.

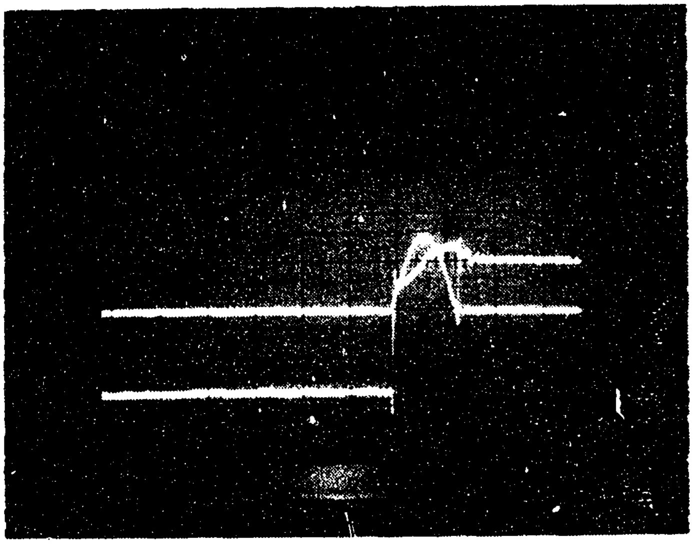

Photograph 2.7.3: SCR T1 voltage and commutation current during charge reversal cycle. VT1: 100V/div, Icc: not calibrated, t: 50μsec/div.

Photographs 2.7.3 and 2.7.4 similarly show the voltages on the main devices during the charge reversal cycle.

The pulse mode lamp voltage and current are shown in Photograph 2.7.5. The pulse width in this photo is ≈1 msec in order to clearly demonstrate the rise

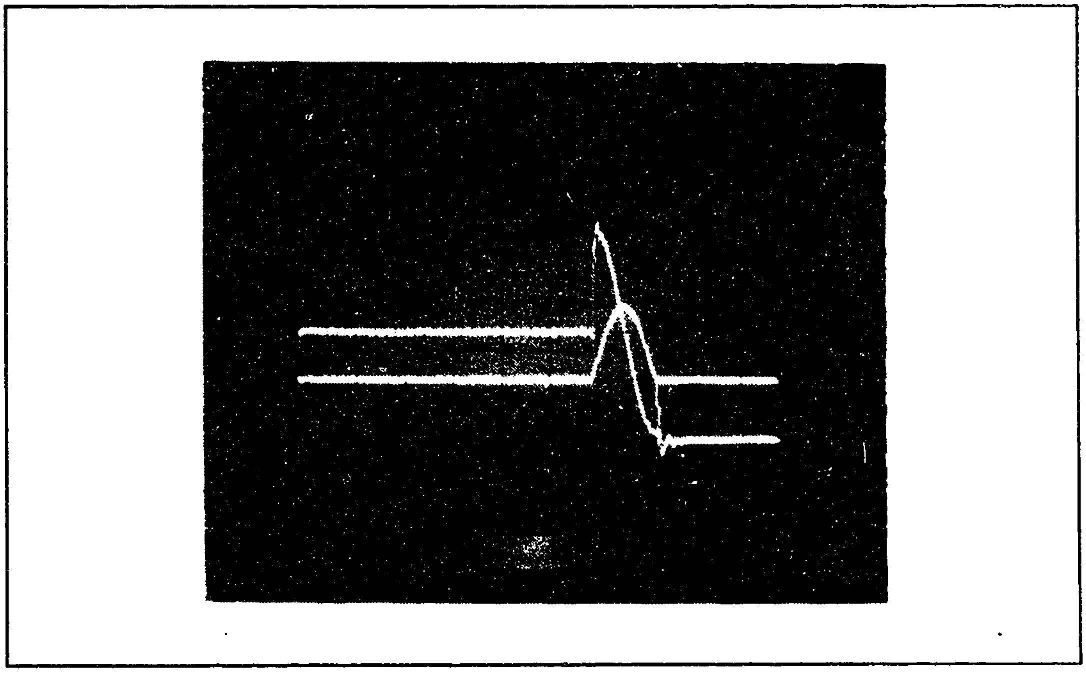

Photograph 2.7.4: SCR T2 voltage and commutation current during charge reversal cycle. VT2: 100V/div, Icc: not calibrated, t: 50μsec/div.

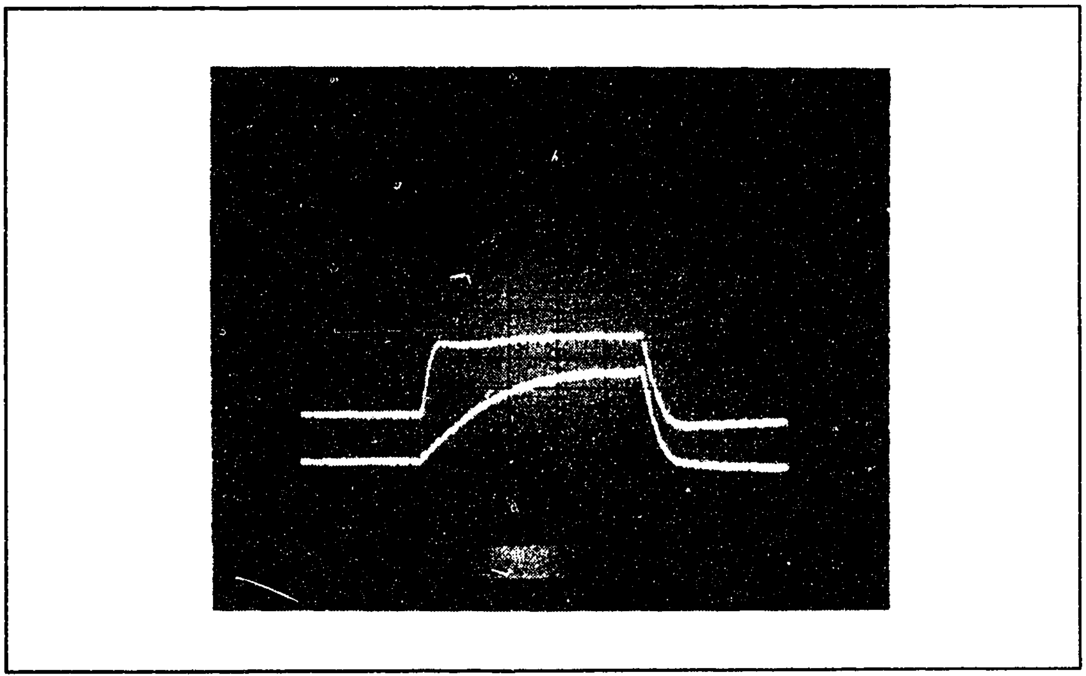

Photograph 2.7.5: pulse mode lamp voltage and current. Vl: 200V/div, Il: 80A/div, t: 200μsec/div.

time of the current through the lamp. The ripple in the capacitor bank voltage is shown in Photograph 2.7.6. In this case the pulse width is 2 msec at a pulse repetition rate of 45 Hz.

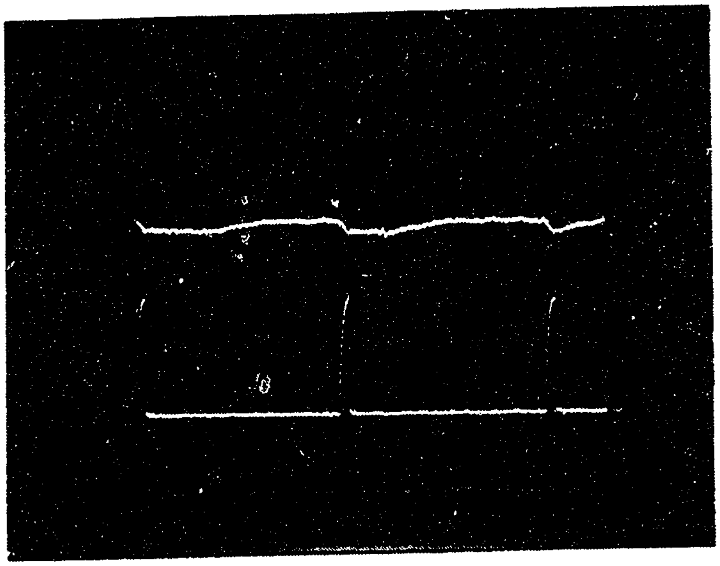

Photograph 2.7.6: pulse mode bank voltage and current. V: uncal., I: 80A/div, t: 5 msec/div.

The above photographs were acquired using a Gould model OS1420 digital storage oscilloscope and a Tektronix A6902 isolator. The current waveforms were obtained with a Tektronix A6303 current probe with an AM503 amplifier.

The continuous mode operating range of the power supply is illustrated in Figure 2.7.2. The maximum rated current for the L-2733 lamp is 45 Adc, which corresponds to a duty cycle of approximately 55%. Comparison with Figure 2.7.1 shows that the operation of the power supply in continuous mode closely follows the predicted response of the lamp. The apparent intercept at 20% duty cycle is a result of the fact that the minimum duty cycle in continuous mode is limited by the minimum "on-time" constraint of 200μsec. The operation of the power supply in regards to overall laser system performance will be discussed in more detail in

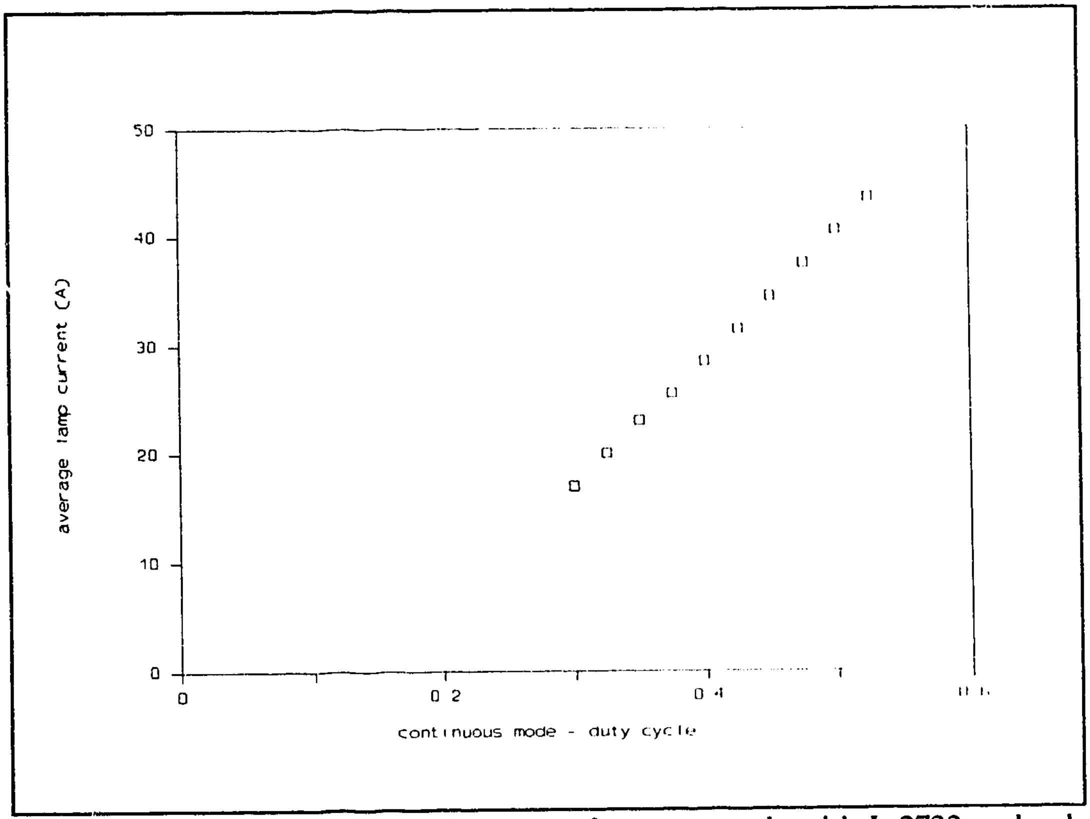

Figure 2.7.2: continuous mode response of power supply with L-2733 as load

a later chapter.

3. Control Electronics

3.1 Introduction

The various parts of the power supply system described in the preceding chapter are, for the most part, large, heavy-duty components capable of controlling the flow of significant current. Their control, however, depends on a series of low-level signals being generated in response to the user's specified criteria. In addition, the range of these signals should be internally limited to guarantee safe operation of the system and as well, protect the user against failure of critical components in the system.

3.2 Design Considerations

In order to operate the chopper power supply discussed in the previous chapter, it is necessary to generate the appropriate low-level timing signals to indicate which thyristor is to be turned on. These signals must be of the correct frequency and duty cycle to produce the desired average output voltage or pulse width, depending on the chosen mode of operation. As described in the chapter dealing with the chopper, a "cold-start" procedure must also be followed to guarantee that the commutation capacitor has attained the full charge required on initialization. The signals must finally be transformed to the proper levels to actuate the change of state of the device under control. In addition, the status of the chopper and its associated support sub-systems must be monitored to safely

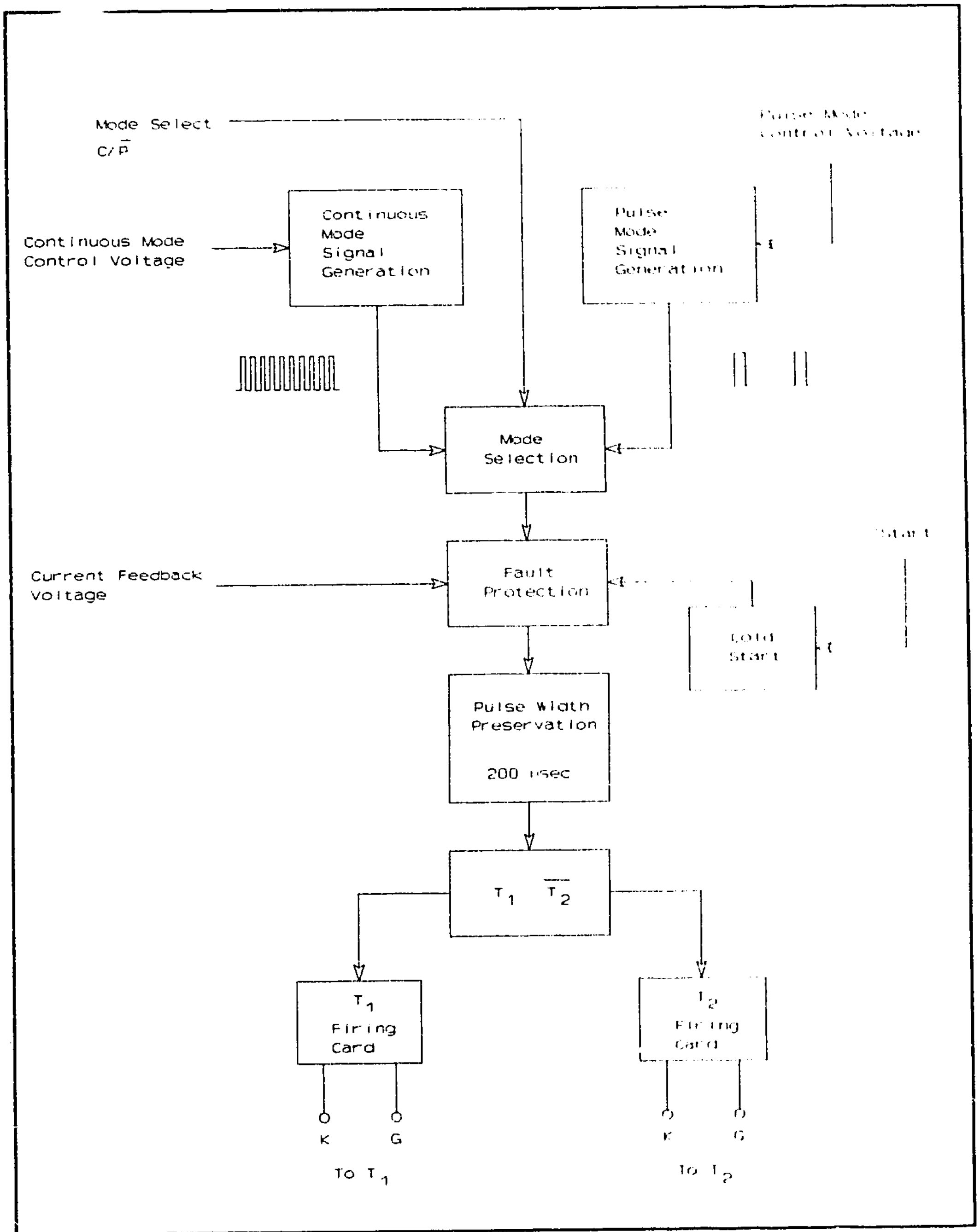

Figure 3.2.1: block diagram of controller section

interlock the overall operation of the system. These basic features of the controller are represented in block diagram form in Figure 3.2.1. Each of the specific modules are discussed in detail in the following sections.

3.2.1 Continuous Mode Signal Generation

As specified in the chapter dealing with the power supply design, the design frequency for continuous operation was chosen to be 1 kHz. It is also specified that in order to comply with the recovery time constraints on the commutating SCRs, the minimum time that the chopper control signal can be in either the "ON" or the "OFF" state is 200 μsec. These criteria will result in a continuous mode signal of the form:

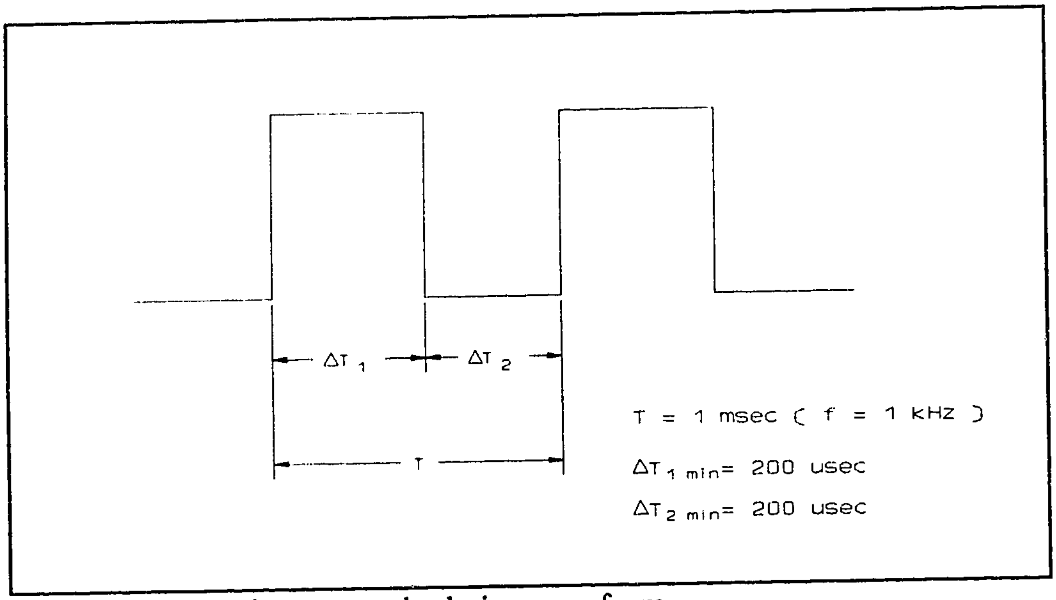

Figure 3.2.2: continuous mode design waveform

This stage is to be driven by a 0 - 12 Vdc analogue voltage which is proportional to the desired duty cycle. The output from this stage, T_{CONT}, must be TTL compatible to interface with the stages which follow.

3.2.2 Pulsed Mode Signal Generation

The pulsed mode signal was chosen to have a fixed duty cycle of 1:10 (ON time:OFF time), and variation in chopper output was to be attained by modulation of the pulse repetition frequency (PRF). This variable frequency was constrained by a working minimum "ON" time of 2 msec and a working maximum "ON" time of 20 msec. This would correspond to an operating frequency range of 4.5 - 45 Hz. This leads to a pulse mode signal:

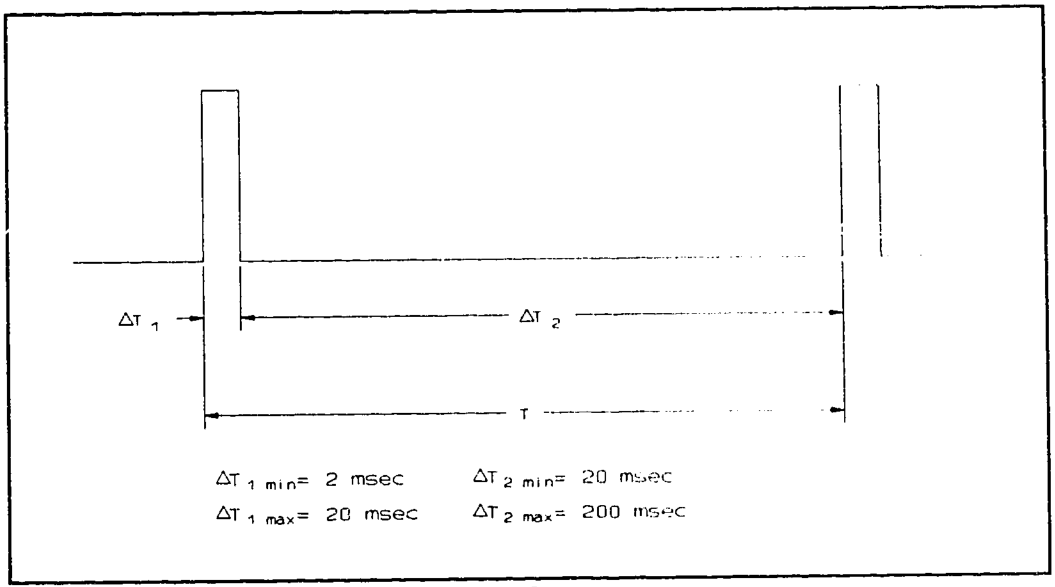

Figure 3.2.3: pulse mode design waveform

Once again, the input to this stage must be driven by the 0 - 12 Vdc analogue voltage and the output, designated as T_{PULS}, is to interface with TTL circuitry.

3.2.3 Operating Mode Selection

This stage of the controller selects the drive signal to be passed on to the next stage as determined by a digital input line C/P^*. The output of this stage is designated as T_{SEL} and is a TTL signal.

3.2.4 "Cold-Start" Hold-Off

An internal signal is generated in this stage which maintains the drive to

T_1 as "OFF" and T_2 as "ON" for approximately 5 msec to allow the commutation capacitor to completely charge to the required initial voltage when the chopper is first started. This signal, together with the output from the fault protection section, (see below) forms T_{OK} which is passed along to the Pulse Width Preservation stage.

3.2.5 Fault Protection

This stage, combined with the cold-start stage described above, provides the signal T_{OK} that is a "safe" signal which is in the chosen operating mode. In this context safe means only that the commutation capacitor is charged and a fault condition does not exist. For the controller version for this experimental system, the only fault condition considered was an overcurrent failure of the chopper. Provision was made for future expansion of this stage to accommodate any number of possible "interlock" inputs.

3.2.6 Pulse Width Preservation

As previously mentioned, there are constraints placed on the minimum allowable "ON" or "OFF" times in all operating modes including an emergency shutdown situation. If the chopper is ordered to turn off without enough time for T_1 to fully recover, there is a danger of a commutation failure which is more severe during an emergency shutdown.

Therefore, if a pulse passing through this stage is too narrow, it will be lengthened to the minimum allowable pulse width. This stage follows the fault protection stage so that in the event of a narrow pulse occurring due to a fault condition, there is no danger of commutation failure.

3.2.7 Firing Card Interface

In order to finally deliver the drive signals to the chopper thyristors, it is necessary to isolate the low voltage waveform generation circuitry from the high voltages present on the SCRs as well as provide a "boosting" of the drive current as required. This final stage accomplishes this task.

3.3 Circuit Description

3.3.1 Continuous Mode Signal Generator

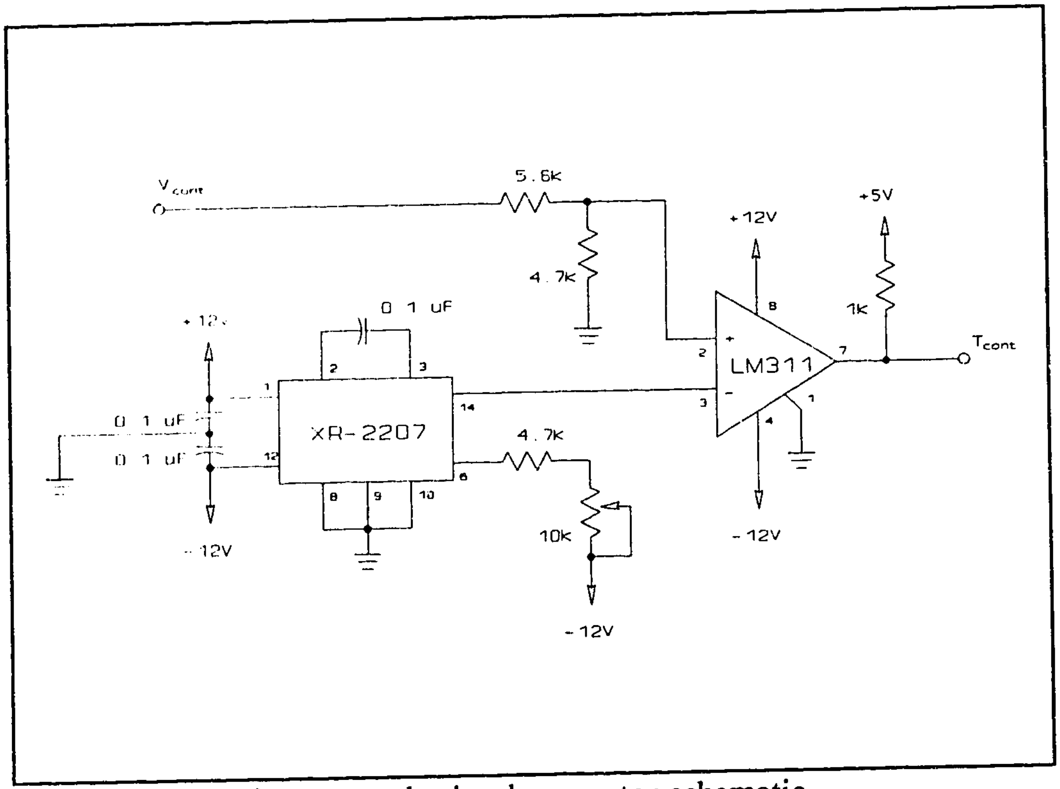

Figure 3.3.1: continuous mode signal generator schematic

An XR-2207 voltage-controlled oscillator forms the heart of this section. It produces a triangular wave at a frequency of 1 kHz with 100% symmetry. This device is configured as per the manufacturer's data sheet with the values of the timing capacitor and resistor being determined as follows:

$$f=1/RC \qquad (3.1)$$

choose

$$C = 0.1\ \mu F$$

so that

$$R=10k\Omega$$

The actual resistor R_1 is made up of a 4.7k resistor and a 10k trim pot in series to provide for accurate tuning of the frequency. This triangle wave is compared to an analogue control voltage via an LM311 Voltage Comparator, producing the pulse width modulated timing signal T_{CONT}.

3.3.2 Pulsed Mode Signal Generator

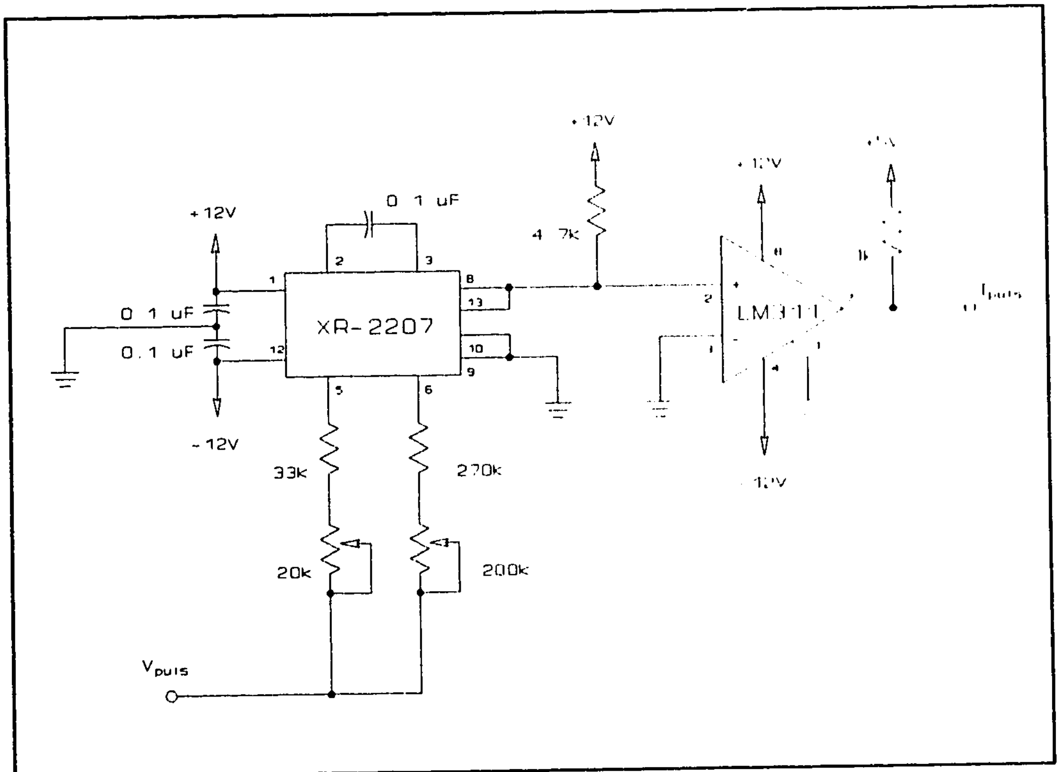

Figure 3.3.2: pulse mode signal generator schematic

Once again an XR-2207 VCO is used to provide the basic timing signal in this section. In this case though, a square wave of varying frequency and fixed duty cycle is required. The timing equations determining the maximum frequency and the duty cycle are:

$$f_{max} = 2/C\ [1/(R_2+R_3)] \tag{3.2}$$

$$\text{duty cycle} = R_2/[R_2+R_3] \tag{3.3}$$

From these equations, and the design parameters of f_{max} = 45 Hz and a duty cycle of 1:10, component values of C = 0.1μf, R_2 = 36kΩ, and R_3 = 360kΩ were selected. Once again the resistors are adjustable to provide for accurate tuning of the frequency and duty cycle. As with the continuous mode timing signal, TTL compatibility is provided by a LM311 Voltage Comparator.

3.3.3 Mode Selector

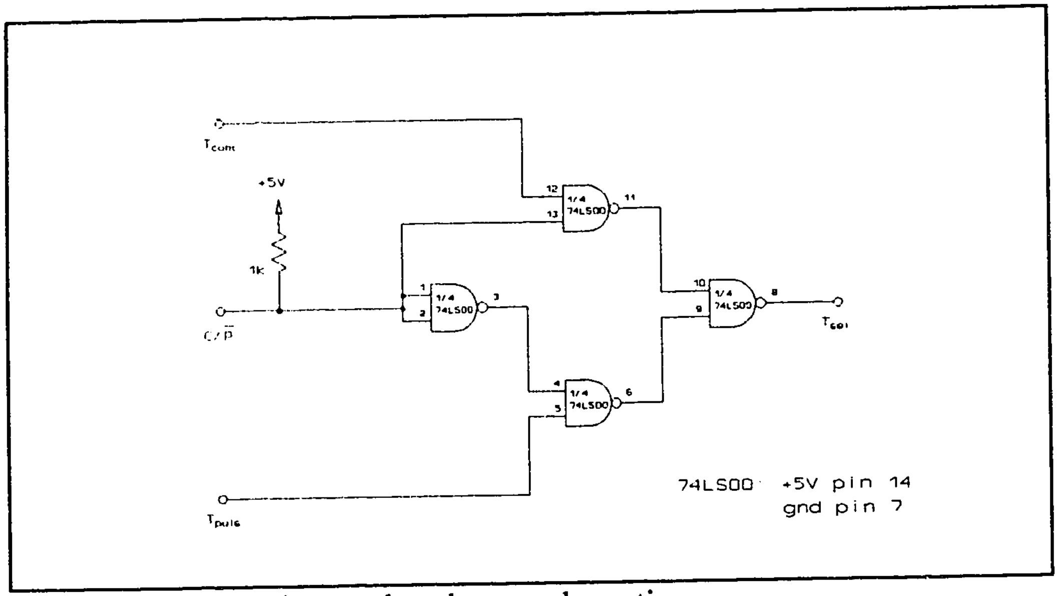

Figure 3.3.3: operating mode selector schematic

This section produces the logical selection of the two timing signals based upon the state of the digital control input C/P^*. The output is selected as:

$$T_{SEL} = T_{CONT}\ C/P^* + T_{PULS}\ (C/P^*)^*$$

The circuit uses all four NAND gates in a single 74LS00 package.

3.3.4 "Cold-Start" and Fault Protection

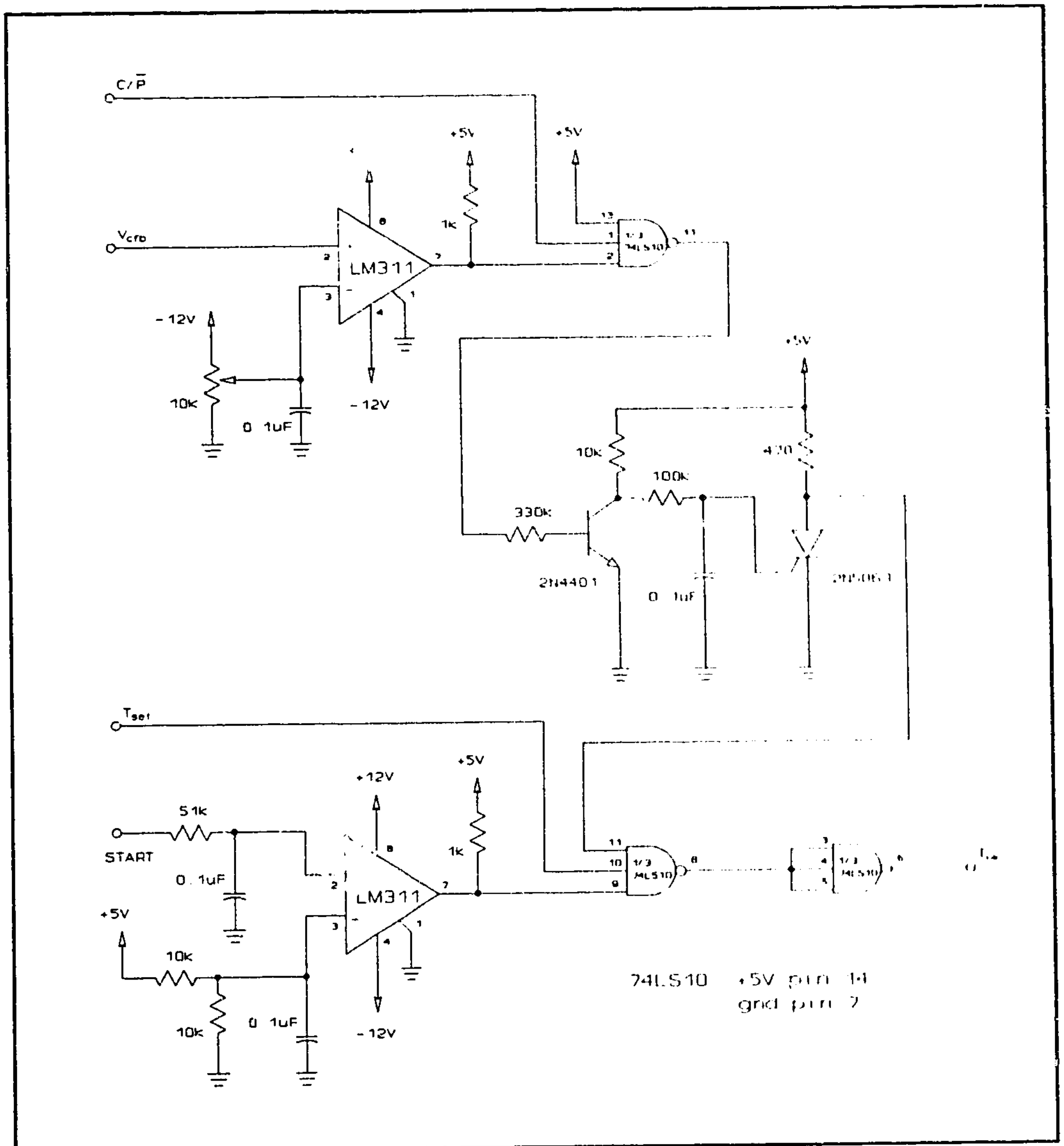

Figure 3.3.4: "cold-start" and fault protection section schematic

Overcurrent fault protection is provided by the comparison of a signal proportional to the output current to a reference value which is proportional to the maximum output current allowed. The output current feedback signal is generated by a Hall Effect current probe located at the output of the chopper as shown in Figure 3.3.5.

Since the peak output current is required to be much higher than the

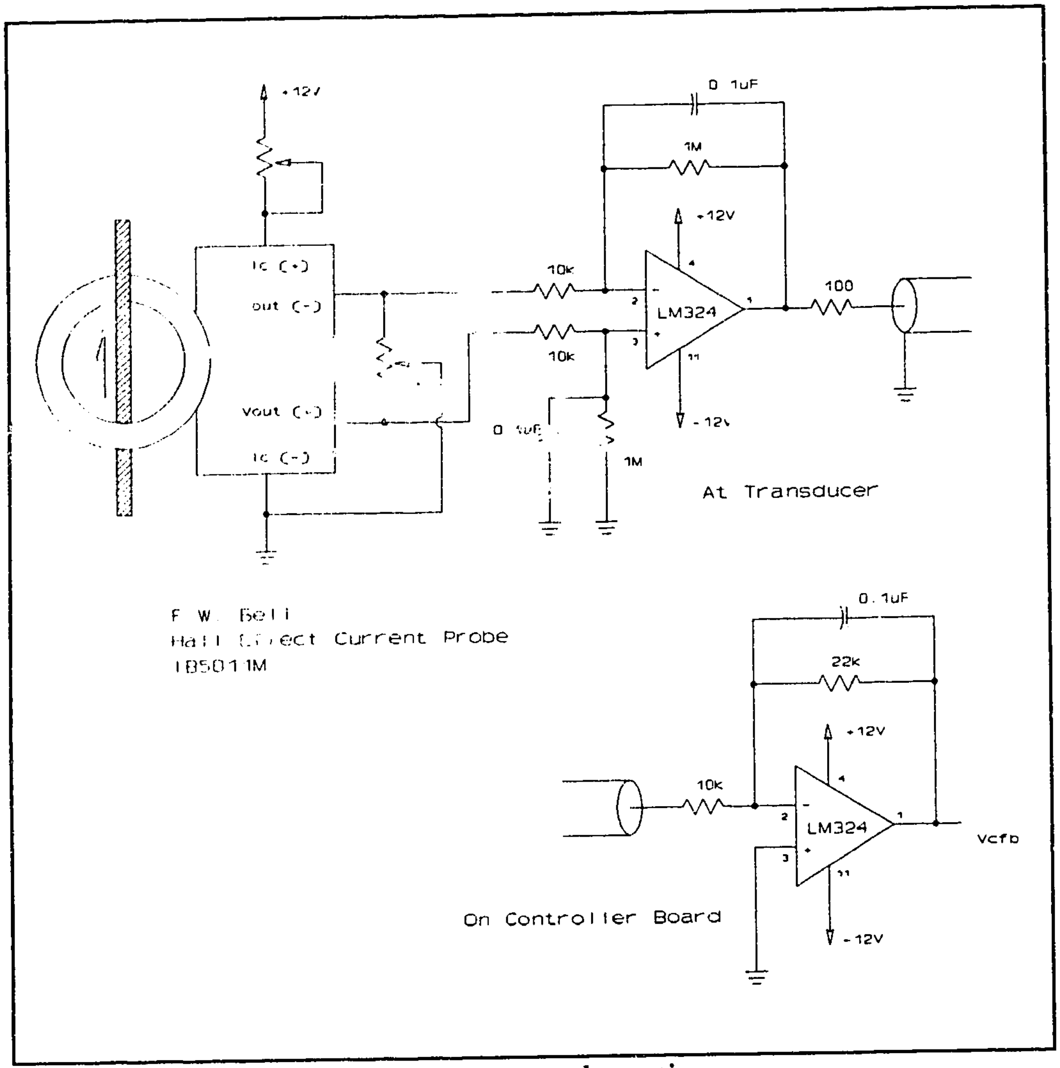

Figure 3.3.5: Hall effect current sensor schematic

maximum allowable average output current in pulsed operation mode, overcurrent faults are monitored only in the continuous operating mode. Thus if the current feedback signal is higher than the reference voltage, the output of the LM311 Comparator goes high. If this occurs with the controller in the continuous operating mode, the output of the first NAND gate will go low gating the SCR "ON". This disables the output until the system is restarted, at which time the fault will presumably have been cleared.

The "cold-start" is achieved by essentially delaying the application of the start signal by a specific amount. When the start signal goes high, the positive terminal of the LM311 will rise as dictated by the RC pair. Here RC = 5msec. When this voltage reaches about 1/2 of its final value the output of the comparator jumps high and if there is no fault detected, the selected timing signal is passed on to the next stages.

3.3.5 Pulse Width Preservation

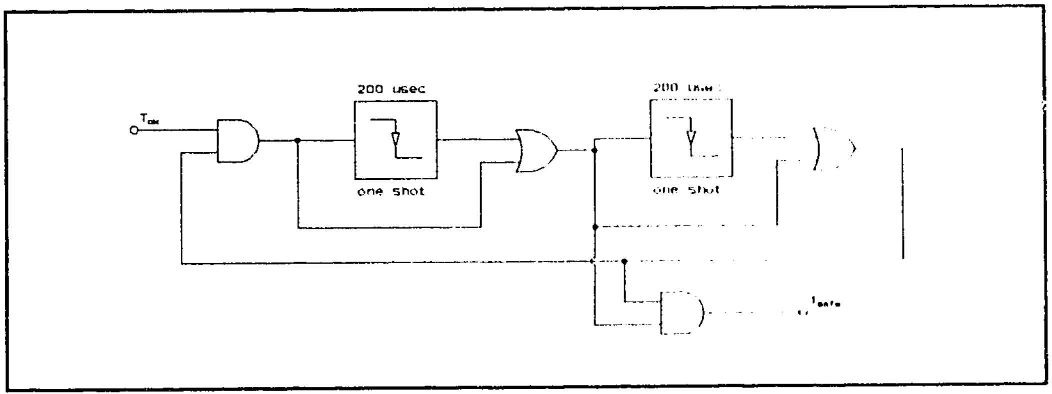

Figure 3.3.6: pulse width preservation section block diagram

This section of the circuit is made up of two nearly identical subsections, one of which guarantees a minimum "ON" time of 200 μsec and the other which guarantees a minimum "OFF" time of 200 μsec. Each subsection performs the same function on a different part of the incoming signal.

The incoming signal is fed through an edge detector circuit which generates a pulse to start a 74LS123 one-shot running at 200 μsec. The output of the one-shot is then OR'ed with the original input so that the longer of either the original pulse or the 200 μsec pulse is passed. By connecting two of these subcircuits together in series, and ensuring that only one can be operating on the incoming timing signal at any given time, the minimum allowable "ON" or "OFF"

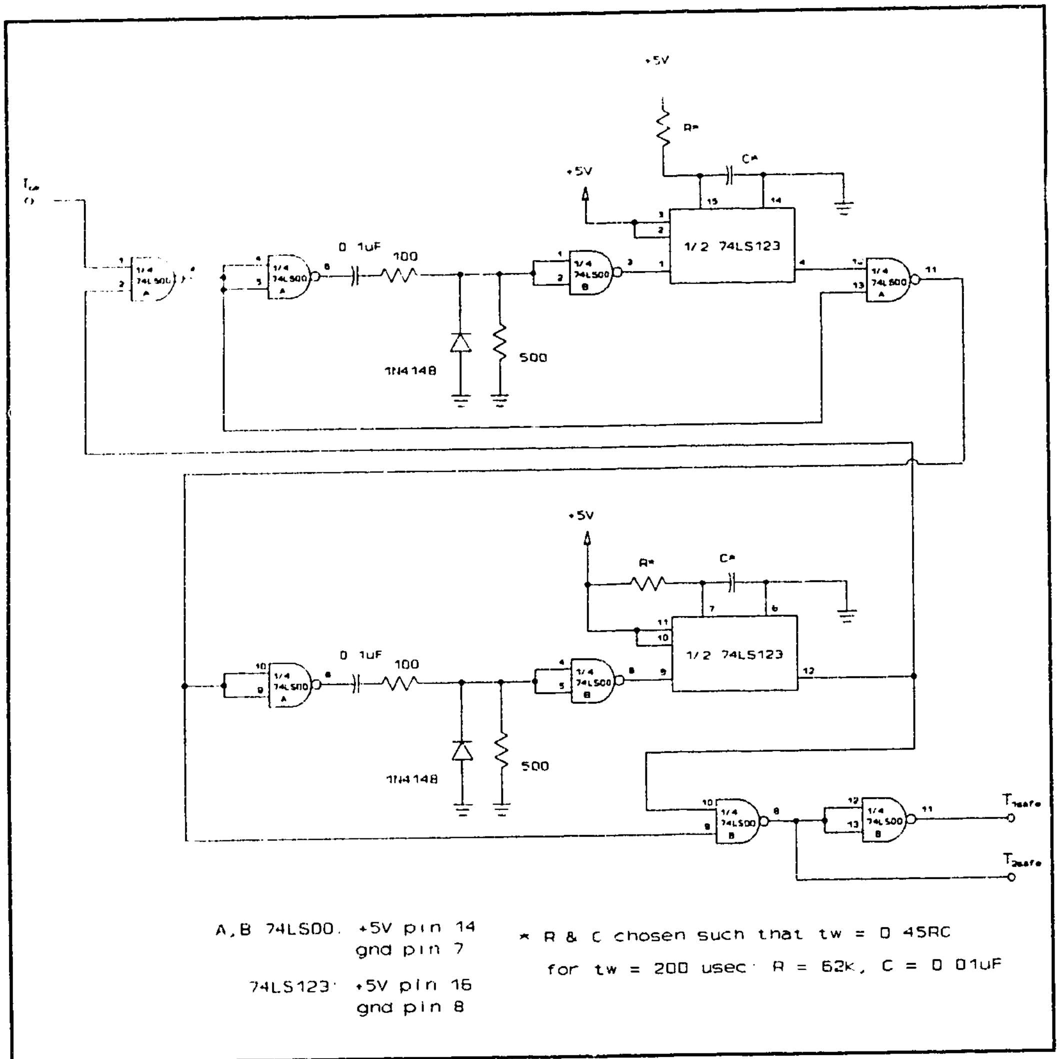

A,B 74LS00: +5V pin 14
gnd pin 7
74LS123: +5V pin 16
gnd pin 8

* R & C chosen such that tw = 0.45RC
for tw = 200 usec: R = 62k, C = 0.01uF

Figure 3.3.7: pulse width preservation section schematic

time can be maintained.

3.3.6 Firing Card

The final section of the control circuit provides the actual gate drive to each of the two SCRs. The appropriately generated control signals are fed into this circuit where they are "mixed" with a high frequency clock signal. The composite signal is then amplified and transferred through an isolation

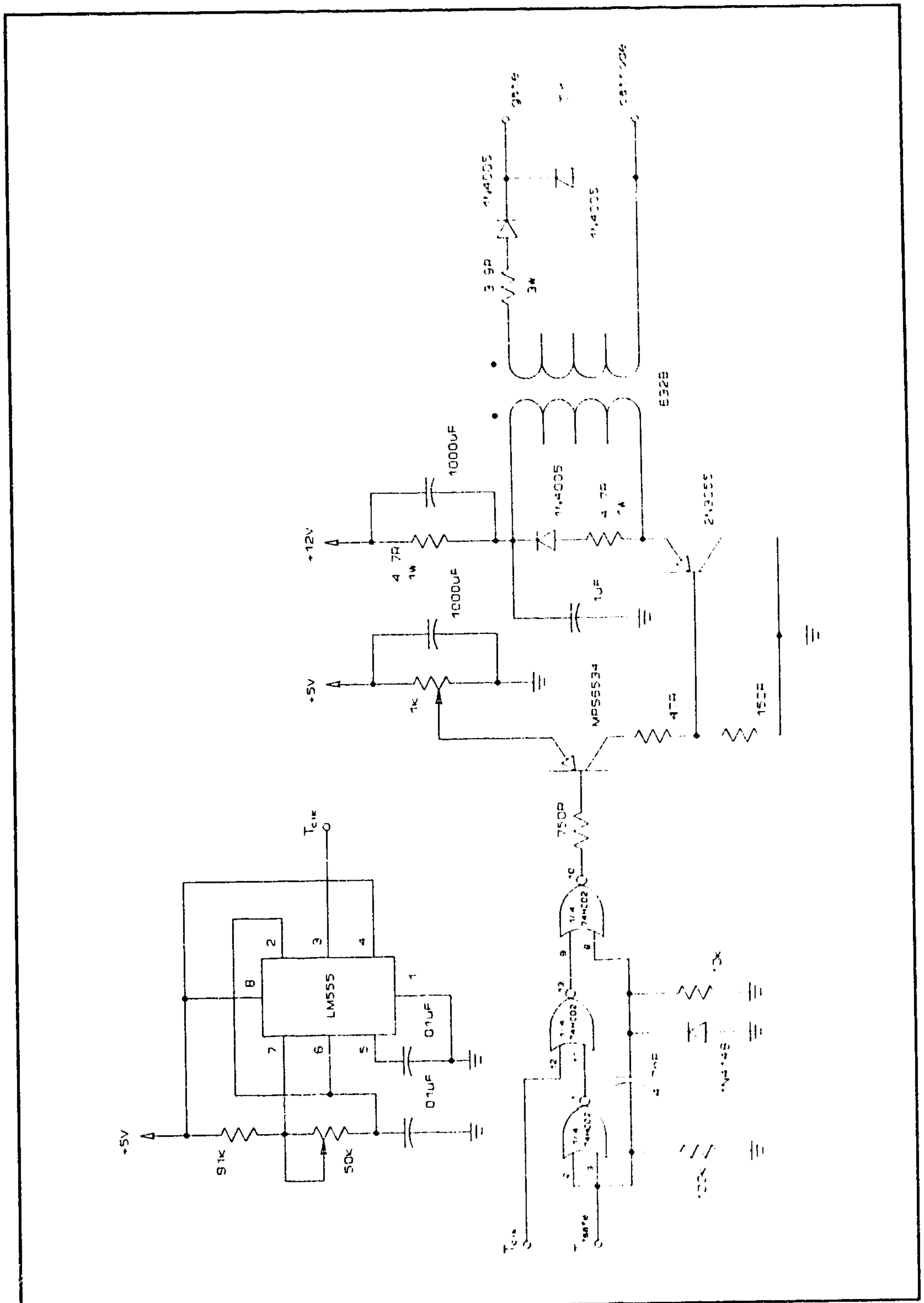

Figure 3.3.8: firing card and clock signal generation schematic. (note: only one channel of the firing card is shown; an identical circuit is required to drive T2)

transformer directly to the gate of the particular SCR being driven. Figure 3.3.8 shows one channel of the firing card and the clock signal generation. The clock signal is generated by an LM555 timer running as an astable oscillator. The frequency of this oscillator is 1 kHz with a duty cycle of approximately 4:5 as determined by the adjustable RC combination. This TTL level signal is then combined with the control signal from the pulse-width preservation section by a 74HC02 quad NOR gate. Since the clock is generated asynchronously of the control signals, an edge detector circuit is employed to supply an artificial "first pulse" to the clocked control signal so that the SCR is triggered by the change of state of the control signal and not by the first available clock pulse. The two-transistor stage then provides the necessary current drive to this modulated control signal which is then passed through a 1:1 signal transformer to the gate and cathode of the SCR.

Photograph 3.3.1 shows the actual firing card as mounted in the system. Both channels are built on this single card, the clock signal is generated at the main control board. The rectangular blocks on the board are the signal transformers which provide that isolation between the high voltage and the control sections. The card cage housing the control circuitry can be seen to the left of the firing board.

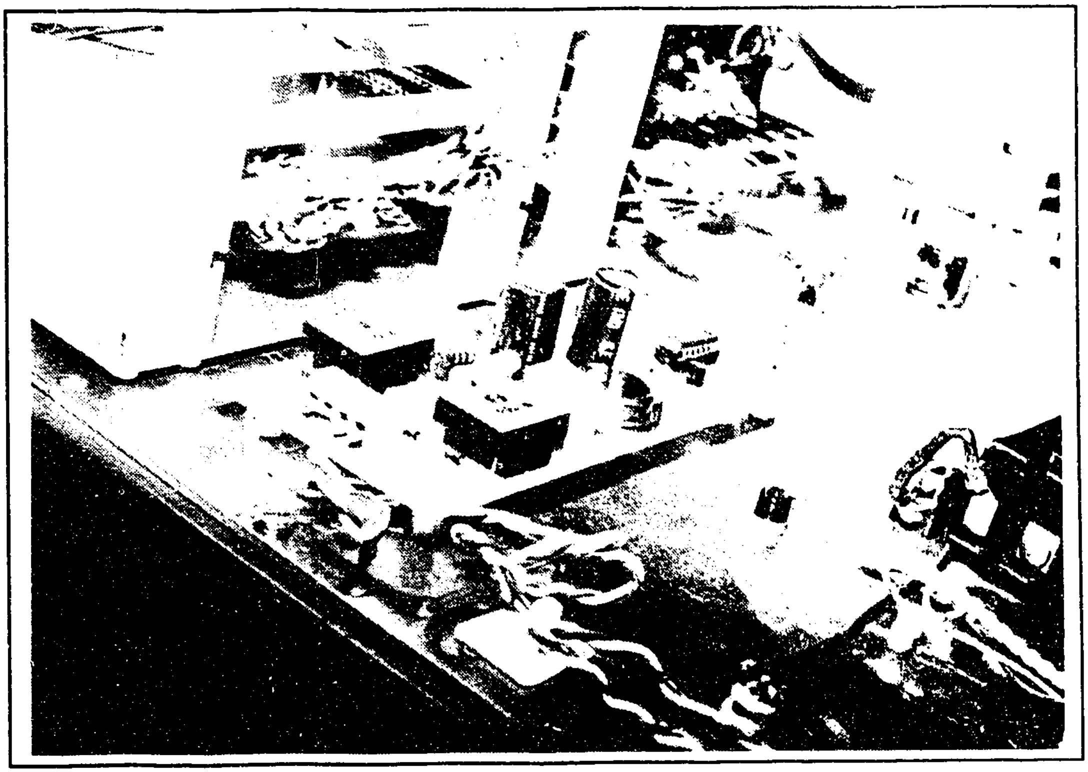

Photograph 3.3.1: firing card

4. Support Subsystems

4.1 Introduction

In addition to the major electrical systems described in the preceding chapters, there are other subsystems which are important, in fact indispensable. However, the details of their operation are not of primary significance to the specifics of this project. For the most part they are standardized subsystems which are found in every Nd:YAG laser system currently available. These subassemblies are discussed in this chapter.

4.2 Cooling Subsystem

Cooling is a very important consideration in a system such as the experimental laser developed in this project. Each of the two main components in the system produce large amounts of heat which must be dissipated. The laser head which contains the Nd:YAG laser rod and the Krypton arc lamp generates the majority of this heat. In addition, the semiconductor switching elements of the power supply must be adequately cooled to ensure reliable operation. This chapter will address the cooling of each of the two subsystems and then describe the cooling strategy implemented to achieve those requirements.

4.2.1 Cooling of the Laser Head

Due to various inefficiencies in the conversion of the electrical power to radiation produced by the arc lamp and then to the actual laser radiation generated in the laser material, any solid-state laser will generate an appreciable amount of heat. This heat will produce a number of unwanted effects. One major problem which will arise with excessive heating is that of thermal stresses being applied to the mechanical components of the head. This may cause distortions in the head which can lead to misalignment, leaking of the coolant and possibly, complete mechanical failure of the head assembly. These thermal stresses can also reduce the lifetime of the arc lamp. This reduction in lifetime can be as dramatic as to fractions of a second if the heating is allowed to reach the extreme case.

Another problem with heating in the laser head is that of optical distortion in the laser rod. This phenomenon is often referred to as thermal lensing. In this situation, the stresses on the cylindrical rod which is heated internally and cooled at the circumferential surface, will cause a distortion of the laser beam. It is interesting to note that this distortion is almost completely due to the temperature and stress-related variations in the refractive index of the laser rod. Mechanical elongation and associated end-face curvature of the rod due to thermal expansion accounts for only a small amount of the thermal lensing action. Optical compensation of this effect is possible with the addition of negative focal length mirrors or a negative curvature on the end-faces of the rod itself. However, due to the thermal time constants involved, this solution is effective only in CW or high rep-rate operation. In pulsed operation with the pulse widths and rates used in this project, optical compensation was determined to be inappropriate.

Finally, due to the high voltages and currents present in the laser head, it is important to keep the conductivity of the cooling fluid as low as possible.

4.2.2 Cooling of the Power Supply

The internal junction temperature of a semiconductor device influences nearly all of its operating characteristics. As such, care must be taken to ensure that this temperature does not exceed acceptable limits. Therefore the device manufacturer's recommendations were followed in heatsinking these devices. Since water cooling was required for the cooling of the laser head it was decided that water cooling would be used for the power supply as well. This greatly reduced the size of the heatsinking components.

4.2.3 Cooling System Description

As shown in Figure 4.2.1, the cooling system used in this project is comprised of two loops. The primary or internal circuit is a closed system containing double distilled, de-ionized water. The secondary, external loop is connected to a separate water source which in the case of this project, is the building tap water.

As mentioned in the preceding section dealing with the laser head, it is important to keep the conductivity of the cooling water as low as possible. To this end, the internal loop was constructed using only plastic or stainless steel components and fittings where possible. A 20 litre plastic "Jerry Can" was modified to be used as a cooling water reservoir. The modifications involved the addition of a fitting at the base of the container so that it could be connected to

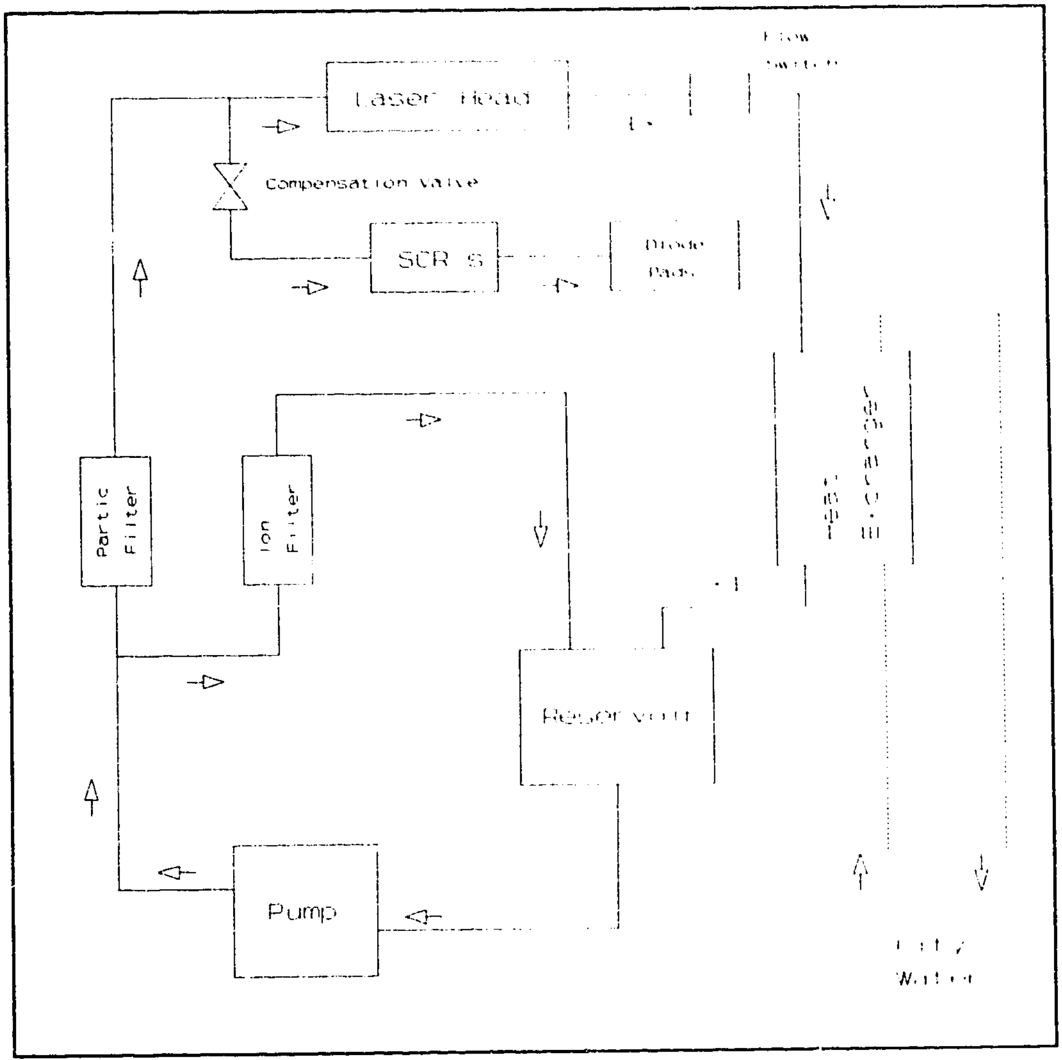

Figure 4.2.1: cooling system block diagram

the pump, a return port in the lid and securing straps for mounting. The pump is a Renown #5-MD-HC and was chosen as a match of the laser head and overall system pressure flow characteristics shown in Figure 4.2.2.

The water from the pump is then filtered to prevent both particulate contamination and high ion content from degrading cooling system performance. The particulate filter is a Filtration Technology #12116 pleated cartridge-type filter and is connected in the main branch of the circuit. A Cole Parmer #R-

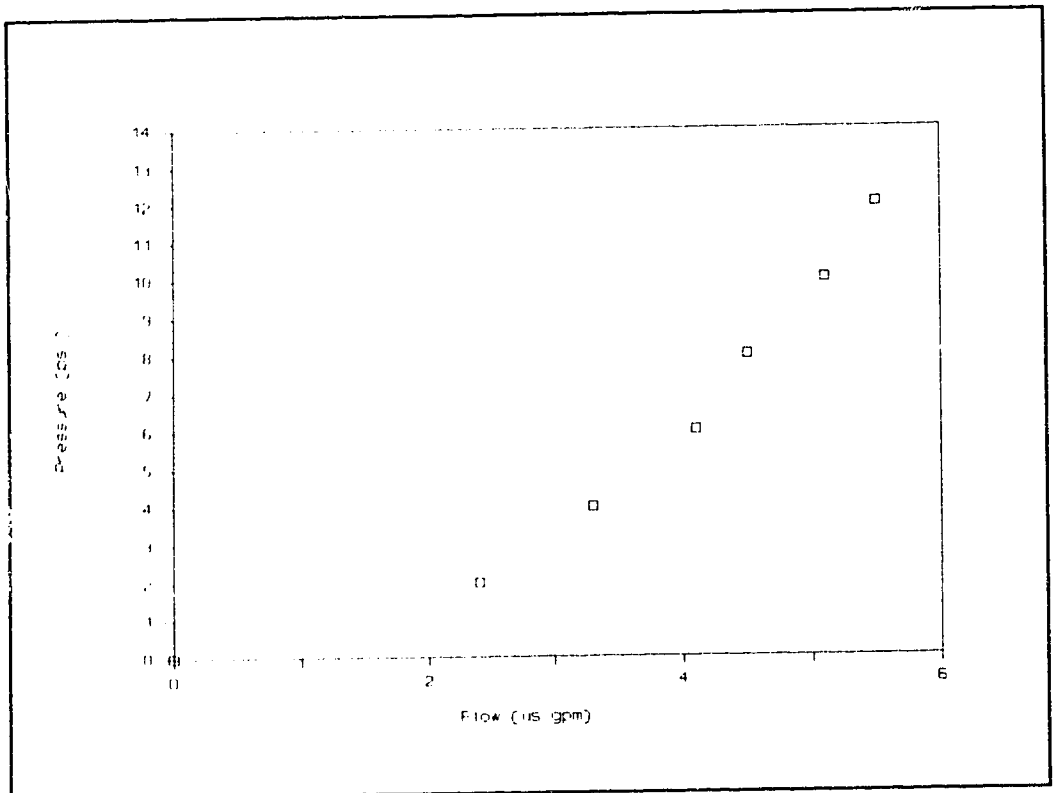

Figure 4.2.2: cooling system pressure-flow relationship

1506-25 ion filter is connected in parallel with the pump as per the manufacturer's instructions. The circuit now branches to supply cooling water to each of the two main systems. Flow is controlled by means of a metering valve in the power supply branch. All water returning to the reservoir passes through an American Standard #5-160-03-014-005 stainless steel heat exchanger which transfers the excess heat to the city water loop. Disconnect valves on the tap water circuit allow for removal of the connecting hoses for transport of the system. System flow integrity is monitored via a Proteus 150C flow switch located downstream of the laser head.

Photographs 4.2.1 and 4.2.2 show the water cooled heatsinks provided for the main semiconductors in the power supply. The heatsinks in photo 4.2.1 are

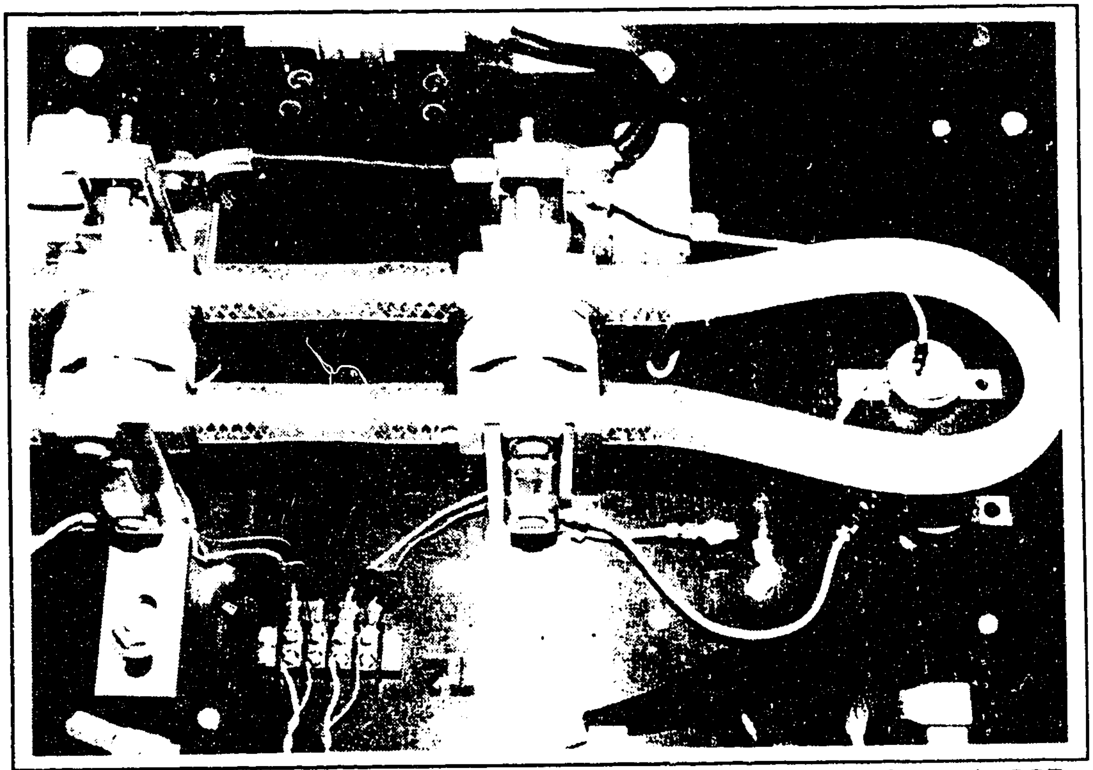

Photograph 4.2.1: commercially available water cooled heatsink for main SCRs.

Photograph 4.2.2: custom-made water cooled heatsink plate.

commercial units purchased with the devices installed, from Westinghouse. In photo 4.2.2 the custom made cooling plates are shown. These are 1/4" thick copper plates machined flat with stainless steel tubes soldered to the sides. Each pair of commutation loop and free-wheeling diodes were mounted on such a plate.

Photograph 3.2.3 gives an overall view of the cooling and high voltage systems. The particulate filter is shown at the back centre of the photo with the ion filter to the right. At the left of the picture is the flow monitor, with the "paddle wheel" visible.

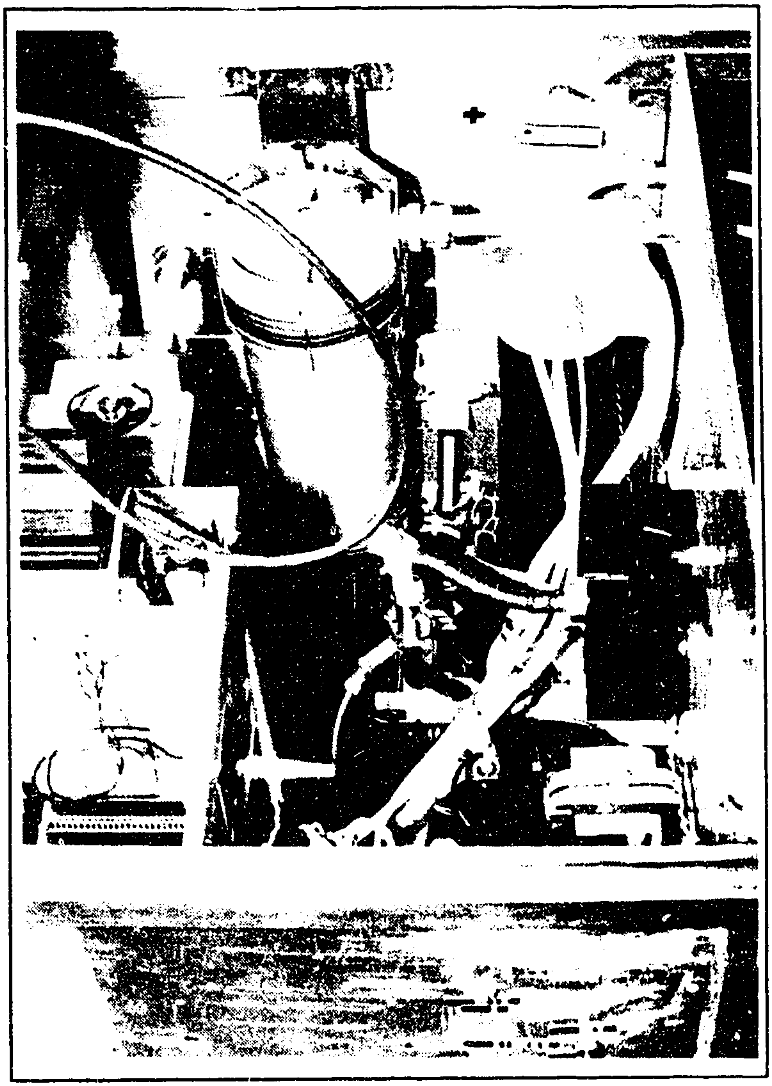

Photograph 4.2.3: view of cooling and H.V. subsystems.

4.3 High Voltage Subsystem

In order to establish a discharge in the Krypton arc lamp, it is necessary to impose upon it a high voltage pulse. In addition, to keep the lamp operating while the main power supply is not running, a relatively low current D.C. power supply is required. The circuit described in this section was adapted from a Lasermetrics 95100 industrial Nd:YAG laser. Figure 4.3.1 represents in block form the four main elements in this subsystem. Figure 4.3.2 is the schematic diagram of this subsystem.

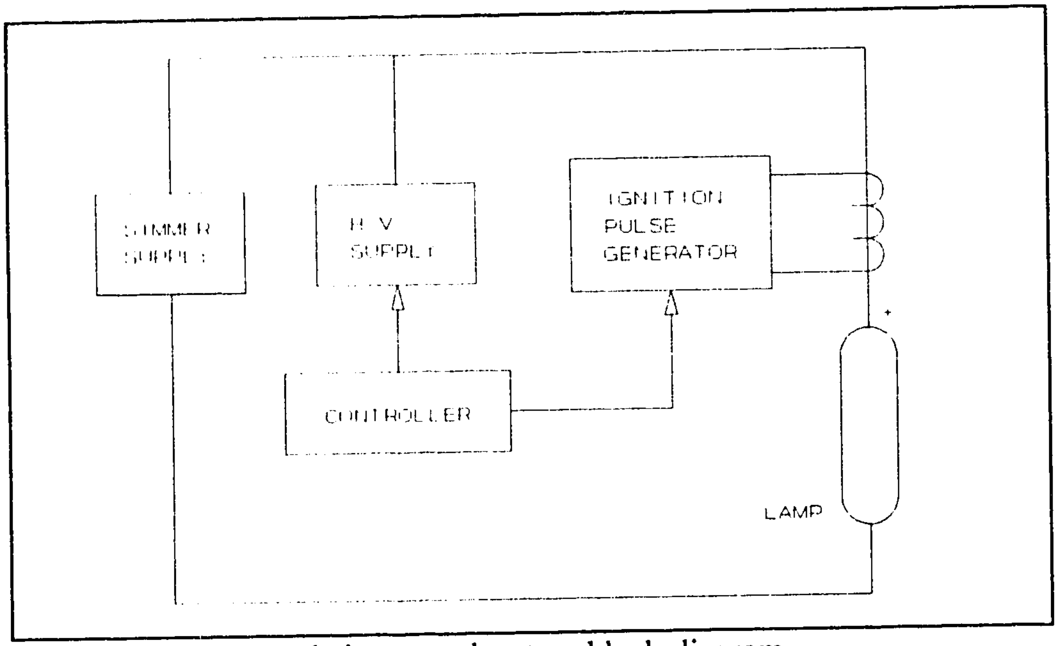

Figure 4.3.1: H.V. and simmer subsystem block diagram

The simmer supply is simply a 1 kW, filtered linear D.C. power supply capable of delivering about 10 A. A multiple tap isolation transformer provides for control of the operating voltage in order to compensate for variations in the V-I characteristics of different lamp types. This A.C. is rectified by the diode bridge BR1 and is then filtered by the 3000 μF capacitor bank. Isolation from the

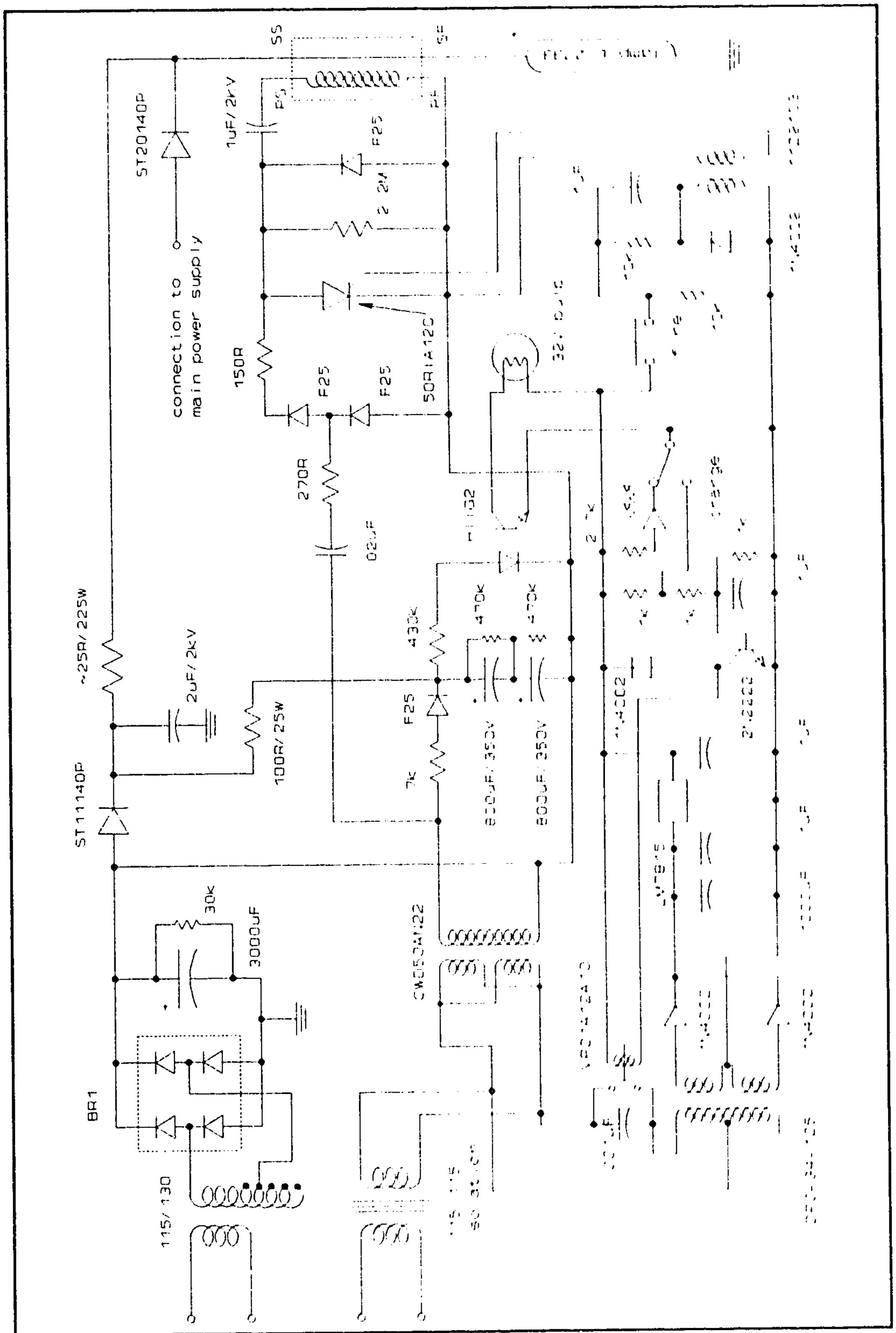

Figure 4.3.2: high voltage and simmer schematic

ignition pulse is achieved with an S.T.Semicon #ST11140P high P.I.V. diode.

The high voltage supply consists of a transformer which steps the line voltage up to 440 Vrms. This A.C. voltage is then half-wave rectified to charge the 700V capacitor bank. Current surge is limited by the 7kΩ resistor. When this bank has fully charged, the optoisolator turns on and a control signal is sent to the control board. The H.V. bank voltage is series connected to the simmer bank supply and this holds the anode of the arc lamp at approximately 700 Vdc.

A voltage doubler circuit is connected to the secondary of the H.V. transformer. When the control signal to "FIRE" the lamp is generated at the control board, the SCR is triggered and the 1μF/2kV capacitor is discharged through the primary windings of the EG&G T-136B series injection transformer. This produces a current pulse which combined with the high voltage present on the anode causes an arc to form in the lamp. Once this arc has been established, the simmer supply provides enough current to keep the lamp operating. The 25 ohm power resistor provides ballast so that the lamp is ensured of operating in the positive resistance region.

As previously mentioned, this subsection is an adaptation of a commercially available circuit. A possible future enhancement to the system would be an automated, switch mode power supply which could perform these functions and which would conceivably require less physical space.

5. Optical Bench

5.1 Introduction

The previous chapters have all been leading up to the subject of the current chapter. The power supply and all the associated control and support systems have been designed to operate the Nd:YAG laser head. The laser head is responsible for the conversion of the electrical energy delivered by the power supply to the optical output energy. This chapter will endeavour to outline some of the more basic laser physics which are relevant to this project. This will be followed by a discussion of how the actual laser system performed.

5.2 Some Laser Basics

An atom can exist only at discrete energy levels, referred to as quantum states. A change of state from a high energy level to a lower level can result in the production of a photon with energy as described by:

$$\Delta E = E_2 - E_1 = h\nu \tag{5.1}$$

where E_2 is a higher energy level than E_1, ν is the frequency of the emitted photon and h is Planck's constant (6.626×10^{-34} Js). This event is called spontaneous emission when the state change is naturally initiated. Similarly, if the atom absorbs a photon at frequency ν, it will jump to energy state E_2, a process

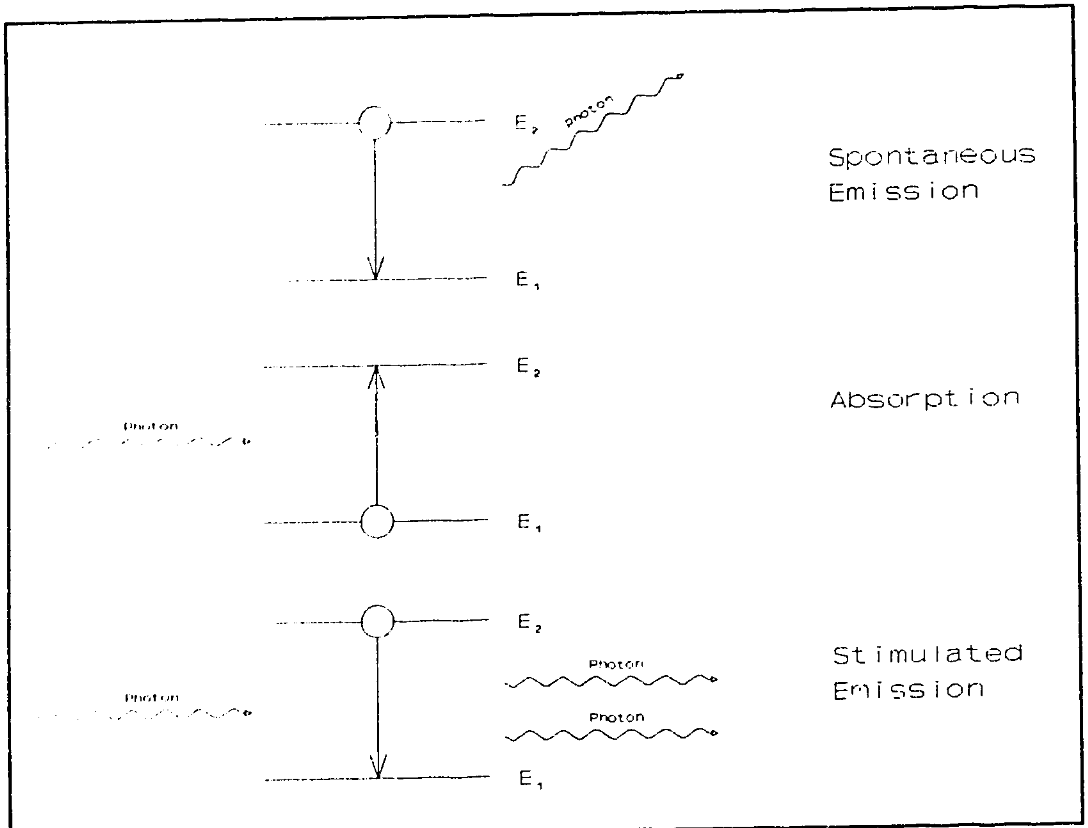

Figure 5.2.1: representation of atomic interaction with radiation

referred to as absorption. However, if the atom is in state E_2 when it is "hit" by a photon of energy $h\nu$, it may drop to E_1 and second photon of the same energy *and the same phase* will be emitted. This phenomenon is called stimulated emission and is crucial to the concept of the laser. (In fact, the term LASER is an acronym for Light Amplification by Stimulated Emission of Radiation.)

For a simple atomic system which has N_1 atoms with energy E_1, N_2 atoms with energy E_2 which is in an energy field described by $\rho(\nu)$, the rates at which these events occur can be expressed as follows. in the case of spontaneous emission:

$$\frac{dN_2}{dt}\bigg|_{spont} = -A_{21}N_2 = -\frac{dN_1}{dt}\bigg|_{spont} \tag{5.2}$$

where $A_{21} = \tau_{21}^{-1}$, the reciprocal of the spontaneous decay time. As the name implies, this process is independent of the surrounding radiation field. For the situation of absorption, the rate will be:

$$\frac{dN_2}{dt}\Big|_{abs} = B_{12}N_1\rho(\nu) = -\frac{dN_1}{dt}\Big|_{abs} \tag{5.3}$$

And in the reverse of absorption, the rate of stimulated emission is:

$$\frac{dN_2}{dt}\Big|_{stim} = -B_{21}N_2\rho(\nu) = -\frac{dN_1}{dt}\Big|_{stim} \tag{5.4}$$

The coefficients A_{21}, B_{12} and B_{21} are called the Einstein coefficients.

Since the total number of atoms in the system is fixed, the overall transition rate of the system is:

$$\frac{dN_2}{dt} = -A_{21}N_2 + B_{12}N_1\rho(\nu) - B_{21}N_2\rho(\nu) = -\frac{dN_1}{dt} \tag{5.5}$$

At thermal equilibrium, the rate of change with respect to time must be zero so:

$$\frac{N_2}{N_1} = \frac{B_{12}\rho(\nu)}{A_{21} - B_{21}\rho(\nu)} \tag{5.6}$$

Boltzman statistics predict that in thermal equilibrium, at temperature T(K), the ratio of the numbers of atoms in each state is given by:

$$\frac{N_2}{N_1} = \frac{g_2}{g_1}e^{\frac{-h\nu}{kT}} \tag{5.7}$$

where g_2, g_1 represent the number of ways that a particular atom can exist in state E_2 and E_1 respectively and, are referred to as the degeneracy of the states. Also, k is Boltzman's constant (1.38×10^{-23} J/K). Equating the above two equations and rearranging yields:

$$\rho(\nu) = \frac{A_{21}}{B_{21}}\left(\frac{B_{12}g_1}{B_{21}g_2}e^{\frac{-h\nu}{kT}} - 1\right)^{-1} \tag{5.8}$$

which when compared to the classical Planck formula for black body radiation:

$$\rho(\nu) = \frac{8\pi n^3\nu^2}{c^3}\,\frac{h\nu}{e^{\frac{-h\nu}{kT}} - 1} \tag{5.9}$$

produces the following relationships between the Einstein coefficients:

$$\frac{B_{12}g_1}{B_{21}g_2} = 1 \quad , \quad \frac{A_{21}}{B_{21}} = \frac{8\pi n^3 h\nu^3}{c^3} \tag{5.10}$$

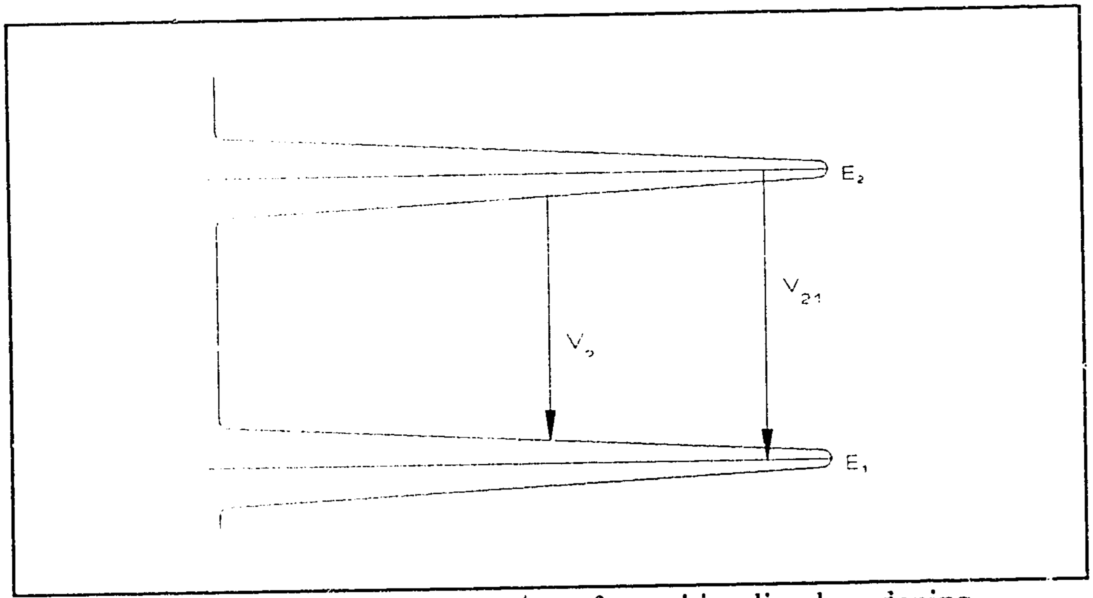

Figure 5.2.2: exaggerated representation of transition line broadening

The "discrete" energy levels described above are at best, an idealization of the actual behaviour of an atomic system. In fact, due to collisions, thermal effects or, random inhomogeneities in the system, the energy levels of the atoms can better be thought of as narrow, peaked bands centered at some specific energy. Now, there will be a range of frequencies over which a transition will occur between these broadened energy levels. The highest probability of transition will be between the peaks of the levels, that is, at ν_{21}. The overall probability that a transition will take place involving an photon of frequency between ν and $\nu + d\nu$ is expressed as $g(\nu)d\nu$. Here, $g(\nu)$ is called the line shape of the transition. Clearly, if an atom leaves one state it must arrive at another, so:

$$\int_{0}^{\infty} g(\nu)d\nu - 1 \qquad (5.11)$$

There are basically two distinct line shapes to consider. The first results from a homogeneous broadening of the transition. That is, every atom in the system has the same frequency response. The line shape for such a transition is represented as a normalized lorentz distribution:

$$g(\nu) - \frac{\Delta\nu}{2\pi}[(\nu-\nu_o)^2+(\frac{\Delta\nu}{2})^2]^{-1} \qquad (5.12)$$

where ν_0 is the center frequency and $\Delta\nu$ is the F.W.H.M. width of the transition. The peak value for the transition is:

$$g(\nu_o) - \frac{2}{\pi\Delta\nu} \qquad (5.13)$$

In the second case, that of inhomogeneous broadening, individual atoms in the system have different frequency responses. This leads to a broadening the overall system. The line shape for an inhomogeneously broadened transition is represented by a normalized gaussian distribution:

$$g(\nu) - \frac{2}{\Delta\nu}\sqrt{\frac{\ln 2}{\pi}}e^{-(\frac{\nu-\nu_o}{\Delta\nu/2})^2 \ln 2} \qquad (5.14)$$

with a peak of:

$$g(\nu_o) = \frac{2}{\Delta\nu}\sqrt{\frac{\ln 2}{\pi}} \tag{5.15}$$

It is now possible to express the transition rate in terms to reflect this broadening. The combined rate equation becomes:

$$\begin{aligned}\frac{dN_2}{dt} &= -A_{21}N_2g(\nu)+B_{12}N_1\rho(\nu)g(\nu)-B_{21}N_2\rho(\nu)g(\nu)\\ &= (B_{12}N_1-B_{21}N_2)\rho(\nu)g(\nu)-A_{21}N_2g(\nu)\end{aligned} \tag{5.16}$$

multiplying both sides by hν gives:

$$h\nu\frac{dN_2}{dt} = h\nu(B_{12}N_1-B_{21}N_2)\rho(\nu)g(\nu)-h\nu A_{21}N_2g(\nu) \tag{5.17}$$

here, the left side represents the change in the rate of change of energy with respect to time or, the change in intensity I(ν). It is convenient then to express the surrounding incident field in terms of intensity as $\rho(\nu)$ = n/c I(ν). So:

$$\Delta I(\nu) = h\nu(B_{12}N_1-B_{21}N_2)g(\nu)\frac{n}{c}I(\nu)-h\nu A_{21}N_2g(\nu) \tag{5.18}$$

Now, for a slab of material with thickness Δz, consisting of atoms in states E_1 and E_2 there will be only $\Delta N_1 = N_1 \Delta z$ and $\Delta N_2 = N_2 \Delta z$ atoms available to interact with the incident radiation. Thus,

$$\begin{aligned}\Delta I(\nu) &= h\nu(B_{12}\Delta N_1-B_{21}\Delta N_2)g(\nu)\frac{n}{c}I(\nu)-h\nu A_{21}\Delta N_2g(\nu)\\ &= \Delta z h\nu(B_{12}N_1-B_{21}N_2)g(\nu)\frac{n}{c}I(\nu)-h\nu A_{21}\Delta z N_2g(\nu)\end{aligned} \tag{5.19}$$

or:

$$\frac{\Delta I(\nu)}{\Delta z} \rightarrow \frac{dI(\nu)}{dz} = h\nu\frac{n}{c}(B_{12}N_1 - B_{21}N_2)g(\nu)I(\nu) - h\nu A_{21}N_2 g(\nu) \tag{5.20}$$

which, when the previous relationships between the Einstein coefficients are introduced, becomes:

$$\frac{dI(\nu)}{dz} = A_{21}\frac{\lambda^2}{8\pi n^2}g(\nu)[N_2 - \frac{g_1}{g_2}N_1]I(\nu) - h\nu A_{21}N_2 g(\nu) \tag{5.21}$$

The contribution of the last term in the above equation is independent of the incident intensity and is thus considered to be "background noise" and is dropped. This spontaneous emission term, while not directly important to the processes of absorption and amplification in the medium, represents a process which is crucial to the initiation of oscillation in the medium and should not be forgotten. Therefore, the final form of the expression for the change in intensity per unit thickness of an atomic system is:

$$\frac{dI(\nu)}{dz} = A_{21}\frac{\lambda^2}{8\pi n^2}g(\nu)[N_2 - \frac{g_1}{g_2}N_1]I(\nu)$$

$$= \sigma_e \Delta N \, I(\nu) = \gamma_o I(\nu) \tag{5.22}$$

$$\sigma_e = A_{21}\frac{\lambda^2}{8\pi n^2}g(\nu) \quad ; \quad \Delta N = N_2 - \frac{g_1}{g_2}N_1$$

where σ_e is called the "stimulated emission cross-section" and is an indication of the relative probability that a transition will occur. The dimensions of σ_e are in terms of area per atom (cm^2). ΔN is referred to as the "inversion" and describes the overall numbers of atoms in the upper and lower levels. γ_o is defined as the "small signal gain coefficient". Examination of this differential form of the gain suggests that if $N_2 < (g_1/g_2)N_1$, the material will effectively attenuate the incident radiation. On the other hand, if ΔN can be made positive that is, $N_2 > (g_1/g_2)N_1$ the material will be an amplifier. Therefore, to achieve a small signal gain of 0.1 cm^{-1} (10%) with in a material with a cross-section of 10^{-19} cm^2, an inversion of 10^{18} atoms/cm^3 is required. For the specific lineshapes mentioned previously, the peak cross-sections can be determined by substituting the peak value for the lineshape for $g(\nu)$.

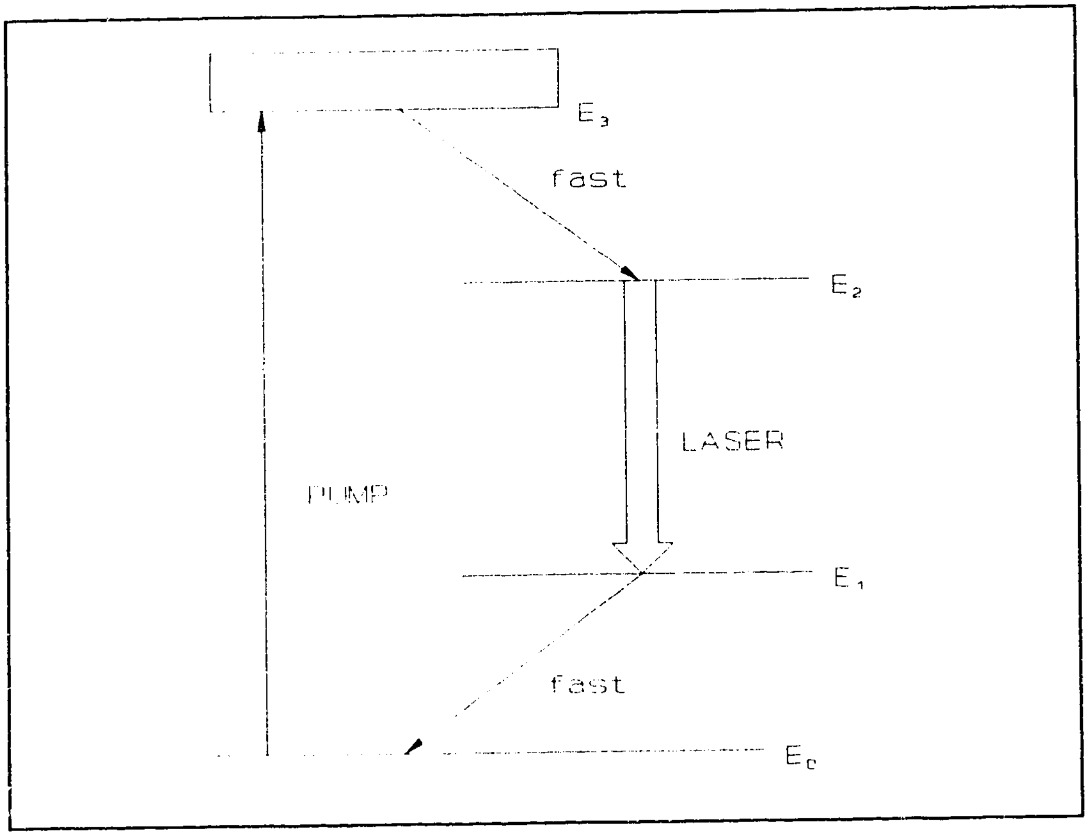

Figure 5.2.3: 4-level laser approximation

The foregoing has dealt with an idealized two level representation of a laser. This is, of course, an extreme simplification of the actual situation. For a solid-state laser material, there are many atomic energy levels with complex processes of excitation and cascaded transitions resulting in laser action. In the case of Nd:YAG and, in fact, the majority of solid-state lasers, it is sufficient to expand the model to a four level approximation. In this case, as shown in Figure 5.2.3 the lowest or ground state is indicated as state E_0. The highest state is E_3 referred to as the pump band and laser action takes place between the intermediate levels E_2 and E_1. The laser process proceeds as follows: applied energy is absorbed by the system causing the atoms to be excited to level E_3. The atoms then relax to state E_2 in a non-radiative transition. In this inverted state, laser action can occur on the transition E_2 ► E_1. From state E_1, the atoms return, via a non-radiative transition, back to the ground state. In the best case, the transitions E_3 ► E_2 and E_1 ► E_0 are much faster than the spontaneous emission rate τ_2. Since the lower laser level is essentially empty due to the fast transition E_1 ► E_0, and similarly, the pump level empties rapidly into the upper laser level, a population inversion can be obtained even for very small pumping powers. In this situation, the rate calculations can be performed as if only E_2 and E_1 are involved. Care must be taken then, so that thermal population of the lower laser level from the ground state does not occur. This population is described by:

$$N = N_o e^{\frac{-\Delta E}{kT}} \tag{5.23}$$

where ΔE is the energy gap between the lower laser level and the ground state and T is the crystal temperature. In many lasers the medium must be cooled to prevent this.

Integration of the previous differential equation of the gain (5.22), yields:

$$I(\nu)- \; I_o(\nu)\; e^{\gamma_o(\nu) z} \tag{5.24}$$

or more simply:

$$I- \; I_o\; e^{\gamma z} \tag{5.24'}$$

Consequently, an electromagnetic wave at an appropriate frequency passing through a medium with a sufficient number of atoms in state E_2, will experience a net increase in energy. Consider the simple laser resonator shown in Figure 5.2.4. The condition of threshold operation means that after a complete round trip, the returning radiation will have the same intensity as it had initially. That is:

$$I_5 = I_1$$

$$I_2 = I_1 e^{\gamma l}$$

$$I_3 = I_2 R_1 = I_1 R_1 e^{\gamma l}$$

$$I_4 = I_3 e^{\gamma l} = I_1 R_1 e^{2\gamma l}$$

$$I_5 = I_4 R_2 = I_1 R_1 R_2 e^{2\gamma l}$$

So, at threshold:

$$R_1 R_2 e^{2\gamma l} = 1 \tag{5.25}$$

If the loop gain $G = R_1 R_2 e^{2\gamma l}$ is greater than one, the radiation will build up on each pass until it is so large that the upper level becomes depleted and the value of the single pass gain coefficient, γ, is reduced. Steady state conditions are reached when the gain per pass is exactly equal to the total round

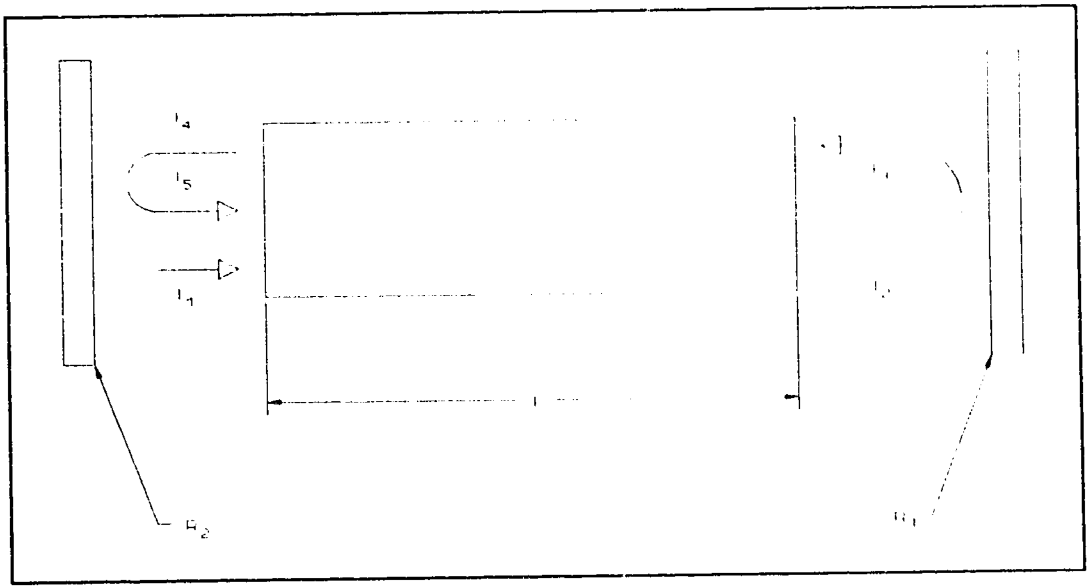

Figure 5.2.4: simple laser resonator

trip losses. The absorption coefficient per unit length, α, is introduced to account for all of the non-output losses. These losses include absorption losses in the laser media, mirrors, and any other resonator elements, as well as scattering, reflection, and diffraction losses. The condition for oscillation is now:

$$R_1 R_2 \exp[2(\gamma - \alpha)l] = 1 \tag{5.26}$$

or,

$$2\gamma l = 2\alpha l - \ln(R_1 R_2) \tag{5.27}$$

The single pass gain is related to the average power density of the radiation, I, in the resonator as:

$$\gamma = \gamma_0/(1 + I/I_s) \tag{5.28}$$

where γ_o is the small-signal gain and I_s is the saturation intensity. I_s is defined as the intensity at which the gain is reduced to 1/2 of the small-signal value. In terms of the physical constants of the medium, the saturation parameter has been determined to be:

$$I_s \approx h\nu/\sigma_e\tau_u \tag{5.29}$$

where τ_u is the upper state lifetime, such that, $\tau_u^{-1} = \tau_{21}^{-1} + \tau_{20}^{-1}$.

The expression for the single pass gain can be substituted back into the above equation for the loop gain. This gives the condition for steady-state laser operation above threshold:

$$2l\gamma_o(1 + I/I_s)^{-1} = 2l\alpha - \ln(R_1 R_2) \tag{5.30}$$

It is possible now, along the lines of the method originated by Rigrod [1,3], to develop a model for the output power of the laser. This results in:

$$P_{out} = A\, I\, (1 - R_1)\, R_1^{-1/2} \tag{5.31}$$

Here, A is the cross sectional area of the laser rod, and I is the geometric mean of the intensity inside the resonator.

$$I = I_s\, [2l\gamma_o/(2\alpha l - \ln(R_1 R_2)) - 1] \tag{5.32}$$

Differentiation of the expression for P_{out} with respect to R_1 and equating to zero would result in an optimum value of R_1.

An alternative method of modelling a solid-state laser has been developed[1,24] which is based on the more readily measurable threshold input power. This model provides an equation for the threshold input power as:

$$P_{th} = K^{-1} [\alpha l - \ln(R_1 R_2)]/2 \qquad (5.33)$$

where K is defined as:

$$K = \eta \sigma_e \tau_{21} /(h\nu A) \qquad (5.34)$$

This term is referred to as the pumping coefficient. η is simply the product of the various efficiencies involved in converting the electrical energy delivered to the lamp into the fluorescent power in the laser rod. Again, A is the cross-sectional area of the rod.

The method also combines all cavity losses into a single parameter. For a (nearly) 100% reflective rear mirror and relatively small cavity losses, with the approximation $\ln(1-L_m) \approx -L_m$, the total cavity losses can be described by:

$$L = 2\alpha l - L_m \qquad (5.35)$$

Here, L_m is a single loss parameter combining miscellaneous cavity losses including scattering, diffraction losses and leakage from the rear mirror.

So, the expression for the threshold power above can be rewritten as:

$$2KP_{th} - L = -\ln(R_1) \tag{5.36}$$

If several values of threshold power are determined for various output mirror reflectivities, the values of K and L can be determined from this simple linear equation.

With this method, it is also possible to calculate an optimum output mirror reflectance from K and L for a given input power:

$$R_{1opt} \approx 1 - [((2KP_{in}L)^{1/2} - L)/(1 + L)] \tag{5.37}$$

5.3 Nd:YAG Laser Properties

Neodymium doped yttrium aluminum garnet ($Nd^{3+}:Y_3Al_5O_{12}$ or Nd:YAG) possesses many physical and optical properties which have made it one of the most popular solid-state laser materials. Undoped, YAG is a transparent, colourless crystal. In the doping process, the trivalent yttrium atoms are replaced by the trivalent neodymium atoms. Due to the differing radii of the two atoms, doping levels greater than about 1% cannot be achieved without putting serious stress on the crystal lattice. When doped with neodymium, YAG takes on a pinkish violet colour. Nd:YAG is a hard crystal with good thermal conductivity and like all garnets, has a cubic crystalline structure which leads to narrow linewidths.

Melting Point [°C]	1970
Density [g cm^{-3}]	4.56
Knoop Hardness	1215
Rupture Stress [kg cm^{-2}]	$1.3 - 2.6 \times 10^3$
Thermal Conductivity [W cm^{-1} K^{-1}]	0.11 - 0.14
Specific Heat [$cm^2 s^{-1}$]	0.59
Index of Refraction	1.82 @ 1.0 μm
Relaxation Time $^4I_{11/2} - {}^4I_{9/2}$	30 nsec
Spontaneous Fluorescence Lifetime	230 μsec

Table 5.3.1: some physical and optical properties of Nd:YAG

The absorption spectra for Nd:YAG is characterized by several strong bands in the 750 nm, 810 nm, and to a lesser degree the 850 - 900 nm regions. Thus, krypton arc lamps are ideally suited for pumping this crystal. A simplified energy level diagram for Nd:YAG is shown in Figure 5.3.1.

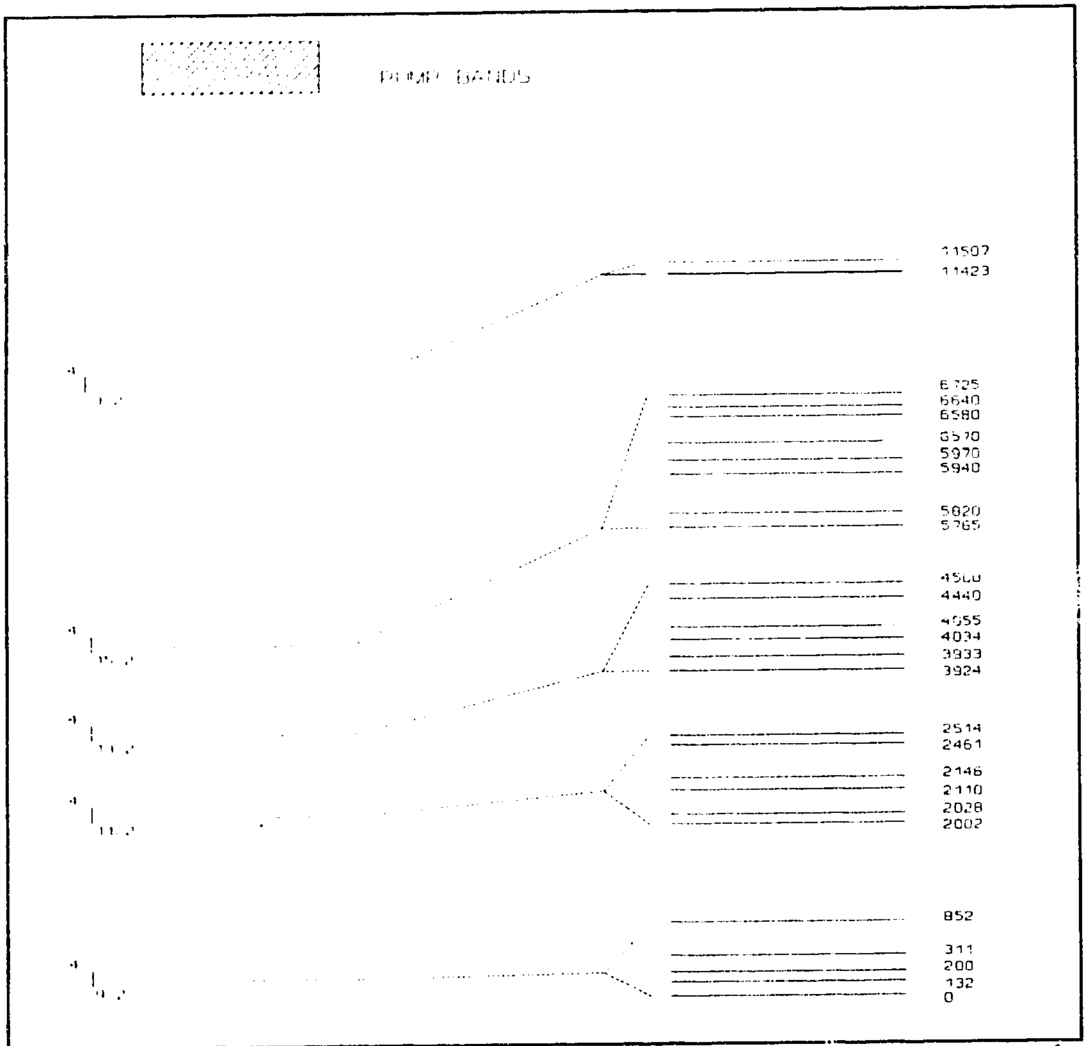

Figure 5.3.1: simplified energy level diagram. energy levels indicated in cm^{-1}

As described previously, Nd:YAG operates on a 4-level scheme. The upper laser level is designated as ${}^4F_{3/2}$ and is split into two components. Laser transitions can take place from this upper level to one of the three lower laser levels classified as ${}^4I_{15/2}$, ${}^4I_{13/2}$ and, ${}^4I_{11/2}$. Each of these levels is split into many components. The ground state, $^4I_{9/2}$, is split into 5 components. The highest energy level in this manifold is ≈ 850 cm^{-1} and the lowest energy level in the $^4I_{11/2}$ state is ≈ 2000 cm^{-1} so that 300 K, thermal population of the lower laser level is not a problem. This leads to an easily achievable threshold condition.

Transition	λ [μm]	σ_e [10^{-19} cm^2]
$^4F_{3/2} \blacktriangleright {}^4I_{11/2}$	1.0521	0.95
	1.0549	0.06
	1.0615	2.5
	1.06414	3.0
	1.0644	1.45
	1.0682	0.6
	1.0737	1.65
	1.0779	0.77
	1.1055	0.16
	1.1119	0.36
	1.1158	0.42
	1.1225	0.4
$^4F_{3/2} \blacktriangleright {}^4I_{13/2}$	1.3187	0.95
	1.3203	0.23
	1.3335	0.44
	1.3351	0.54
	1.3381	1.0
	1.3419	0.36
	1.3533	0.28
	1.3572	0.73
	1.4150	0.2
	1.4271	0.08
	1.4320	0.13
	1.4444	0.28

Table 5.3.2: summary of Nd:YAG laser transitions and stimulated emission cross sections (300 K). [2], adapted

The strongest transition takes place between the highest energy level in the $^4F_{3/2}$ manifold (11502 cm^{-1}) to the 2111 cm^{-1} level in the $^4I_{11/2}$ manifold. This transition produces radiation at a wavelength of 1.06415 μm which is the most common Nd:YAG laser wavelength. A summary of laser transition wavelengths and associated stimulated emission cross sections is presented in Table 4.3.2.

5.4 Laser System Performance

The laser head module in this experimental system is based upon a commercially available Lasermetrics 95100 head. It contains a 4" (102 mm) x 1/4" diameter Nd:YAG rod and, as previously mentioned, a 6 mm bore x 4" arc length Krypton arc lamp. The lamp and rod are mounted inside a gold plated copper elliptical cavity. This cavity assembly is installed in a black delrin block which has been machined to provide the required water cooling flow paths. A mount is provided on the base of the head so that it can be positioned on an optical rail.

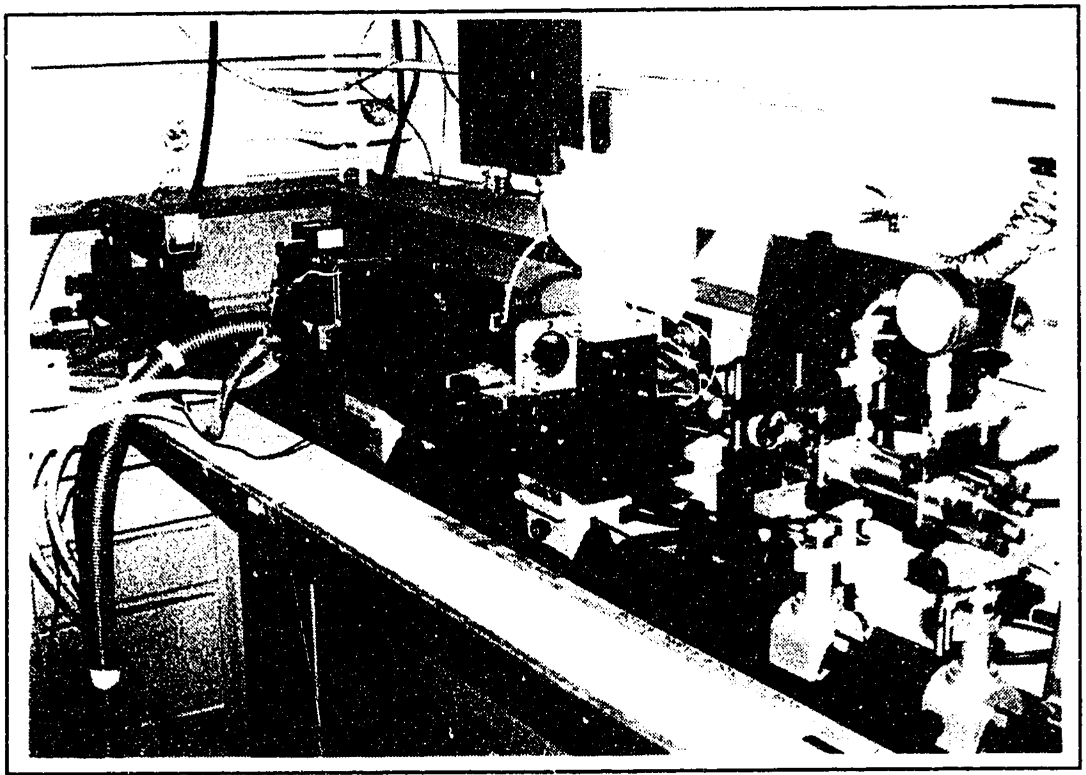

Photograph 5.4.1: the experimental laser system head shown on the optical rail. the vessel at the right is an experiment which is not part of this project.

In a similar fashion, the mirror holders are made in such a way as to be rail mounted. The complete head subsystem is shown in Photograph 5.4.1. The head is located in the centre of the picture and the front mirror mount is clearly shown. A HeNe alignment laser can be seen at the back left of the photo.

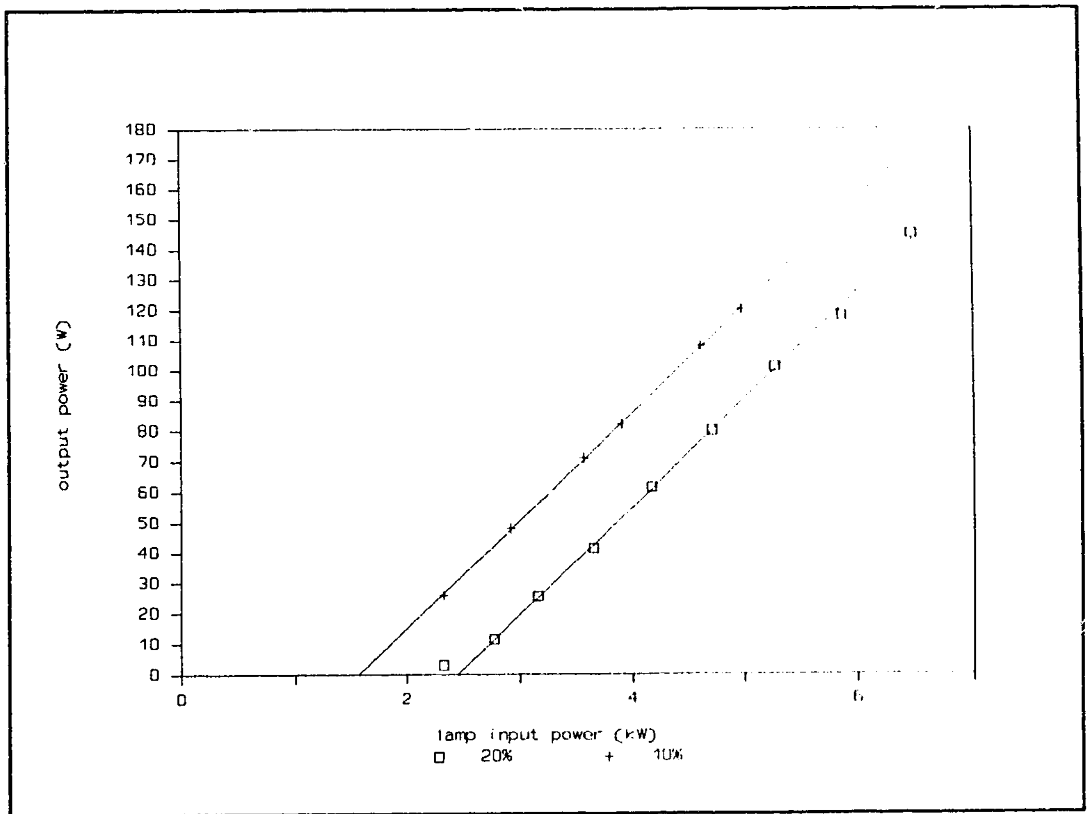

Figure 5.4.1: continuous mode, 1.06μm output vs input curves for the experimental laser system with R_1 = 80%R and 90%R.

The input power versus output power curves for the experimental laser system are presented in Figure 5.4.1. From the Figure it can be seen that the threshold input powers are 1568 W and 2447 W at 10%T and 20%T respectively. From these values, using the previously described method the model parameters are:

$$K = 67 \times 10^{-6} \, W^{-1}$$

$$L = 0.1047$$

The graphical representation of how these values are determined is given in Figure 5.4.2.

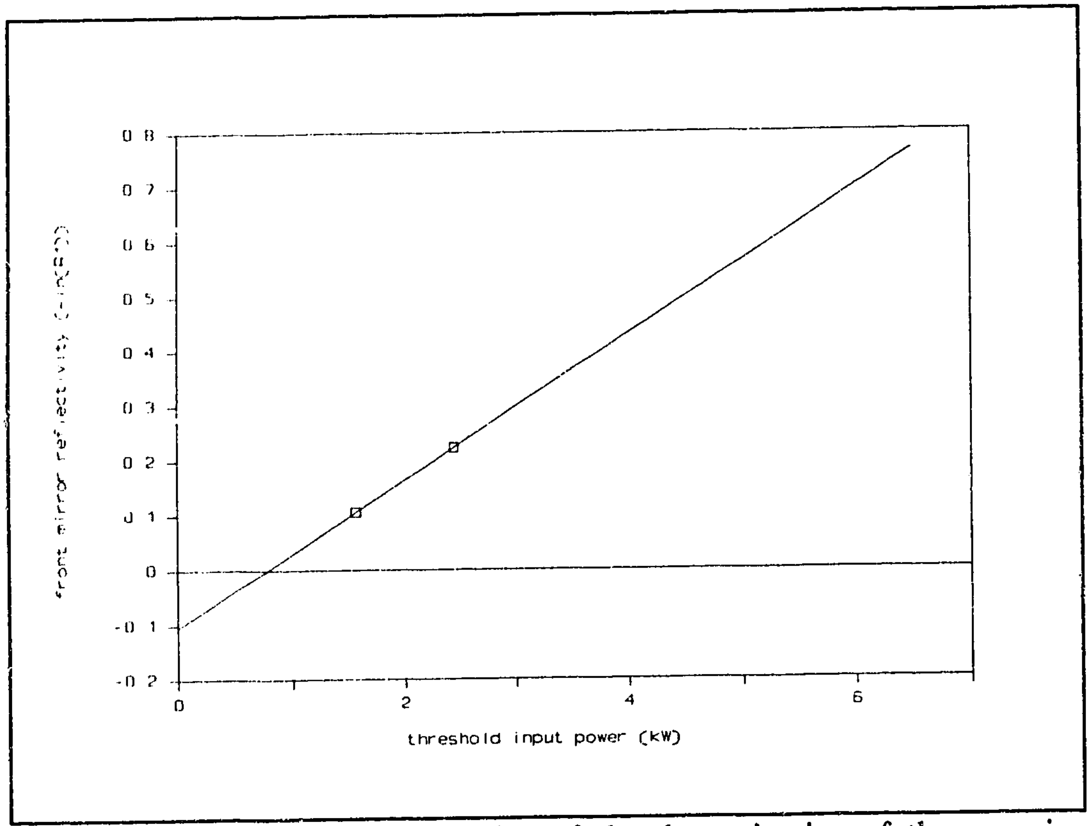

Figure 5.4.2: graphical representation of the determination of the pumping coefficient, K, and the loss parameter, L.

The values of K and L also give:

$$R_{1opt} = 82.2\% \text{ @ } 6.5 \text{ kW input}$$

In pulsed mode operation, the laser can be thought of as functioning in a quasi-cw manner. This is due to the fact that for the operating range chosen, the pulse widths are much greater than the laser fluorescent lifetime, $\tau_{12} = 230\mu\text{sec}$

and the minimum T_{on} = 2msec. Laser performance in pulse mode is given in Figure 5.4.3.

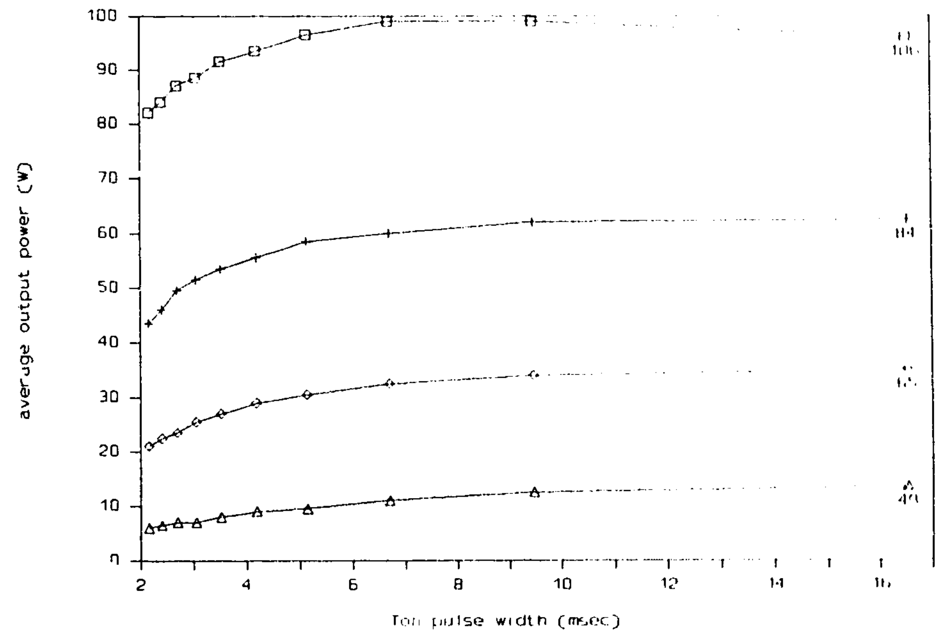

Figure 5.4.3: 1.06μm pulsed mode operation performance, peak input power is indicated to the right of the curves: □ 106 kW, + 84 kW, ◇ 65 kW, △ 49 kW.

The power delivered to the laser head was controlled by means of a three phase variac connected to the input of the main power supply. The nonlinear portion of the curves for pulse widths of 5msec and less can be attributed to the decrease in input power due to the relatively slow rise time of the current in the lamp. This rise time is shown in the chapter dealing with the power supply performance. For the highest input power curve, the reduced output power observed for long pulse widths is a result the increased discharge of the main capacitor bank.

One experiment of particular importance involved the generation of longer wavelength radiation from Nd:YAG on this system. Investigation of the literature indicated that a laser line at 1.44μm existed. While this line was relatively weak, it was determined that with the peak input powers available this line could be made to oscillate. The stimulated emission cross section provides an indication as to the relative strength of this transition:

$$@\ 1.064\mu m:\ \sigma_e = 3.0 \times 10^{-19}\ cm^2$$

$$@\ 1.444\mu m:\ \sigma_e = 0.28 \times 10^{-19}\ cm^2$$

So, for an equivalent population inversion, the gain at threshold is approximately ten times less at 1.44μm. If a minimum gain at 1.44μm is chosen as 10% then:

$$g_{1.44}\, l = \gamma_{1.44} = \ln(1.1) = 0.095$$

this indicates that the gain coefficient at 1.06μm will be:

$$\gamma_{1.06} = \gamma_{1.44}(\sigma_{1.06} / \sigma_{1.44}) = 1.018$$

Therefore, to reduce the loop gain to below threshold at 1.06μm the reflectivity of the mirrors at 1.06μm must be reduced to at least:

$$R_1 R_2 e^{1.018} < 1$$

or,

$$R_1 R_2 < 0.362$$

For standard broad-band high reflectors, the value of R_2 will contribute only slightly to this reduced reflection at 1.06μm. Thus, a front mirror with something less than 35%R at 1.06μm and in the order of 85-95%R at 1.44μm was chosen. Several mirrors were fabricated in an attempt to achieve these criteria. Two mirrors were selected with the following specifications (the nomenclature #2 and #5 are as a result of the coating procedure and have been retained):

Mirror #2: 12%R @ 1.06μm, 94%R @ 1.44μm
Mirror #5: 18%R @ 1.06μm, 86%R @ 1.44μm

The output obtained from the laser with these two optics is presented in Figure 5.4.4. From these data, the model described above was applied yielding:

$$K = 5.4 \times 10^{-6}\ W^{-1}$$

$$L = 0.1424$$

which gives,

$$R_{1opt} = 90.7\%R \text{ @ } 40kW \text{ input}$$

The spectral content of the output radiation obtained with each of the two mirrors was verified with a monochrometer. In each case there was no indication of any 1.06μm radiation present.

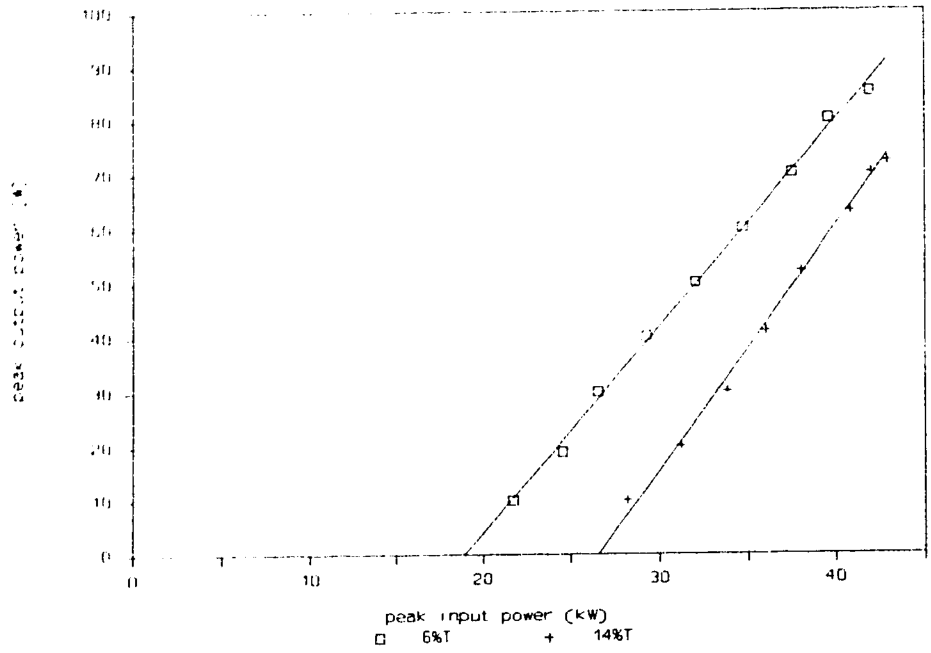

Figure 5.4.4: pulse mode @ 1.44μm, output vs input power curves with R_1 = 86%R and 94%R.

6. Summary and Conclusions

This project set out to develop a flexible experimental Nd:YAG laser system. The primary purpose for such a study was to provide a tool which would allow for further research into new medical uses of the Nd:YAG laser. Any instrument to do this must offer some significantly different operating modes from existing systems. High peak power pulsed output was chosen as the primary alternative to conventional CW operation. As a result of this new capability, it was possible to experiment with the production of longer wavelength laser radiation from some of the weaker transitions in Nd:YAG. The three stages involved in the development of this experimental Nd:YAG laser system have been presented in this thesis. Design, construction, and testing of each of the main subsections are detailed in the preceding chapters.

The major component in the system, the power supply, received the most detailed attention. This module provides the means by which the high peak power pulses were delivered to the lamp. At the same time, the conventional continuous wave mode of operation was maintained. A chopper converter of this type is customarily used to supply the drive for a DC motor. As such, the chopper is operated in the higher frequency range with the motor windings being a largely inductive load. This is exactly the case in continuous mode for the laser system operation whereby and L-C filter is connected to the output. In the pulsed mode, though, by reducing the inductance and modifying the pulse width and repetition rate, high current DC pulses can be delivered. However, it was determined that if the output inductance was reduced beyond some minimum value, chopper performance was drastically reduced. In the initial testing stages the chopper was operated in this critically low inductance situation and commutation failure was experienced. When this failure occurred, the primary current carrying SCR would latch on" and the main capacitor bank would be discharged directly through the load. This resulted in currents well beyond the acceptable maximum being delivered to the lamp. While this produced some rather spectacular laser output powers, it was at the expense of a serious reduction in the lamp lifetime; in fact, the lamp would eventually shatter after a few of these current surges. This would require a thorough cleaning of the entire cooling system to remove any glass pieces that could damage the pump or cause a flow restriction. With the addition of a small output inductor, this problem was corrected and the chopper proved to be quite reliable.

Audio noise was a slight problem at the 1 kHz operating frequency used in continuous mode. Future versions of the power supply will incorporate potted inductors to reduce this condition, which although annoying, did not cause any reduction in system performance. Rather, it was claimed that it was an effective indicator that the laser was in operation.

Further experimentation with the system eventually indicated that higher output power pulses were required. In an effort to accomplish this, a higher source voltage was used to feed the VICC chopper. A three-phase voltage doubler was eventually developed [2] to raise the main capacitor bank voltage to nearly 600V. Only slight modifications were required to the commutation circuit

---

[2] - While this modification was outside the scope of this thesis, it is mentioned here to illustrate the flexibility of the system.

to accommodate this. The three-phase doubler operated in a satisfactory manner for initial experimentation but proved to be too unbalanced for evaluation outside of the laboratory. Currently research is being performed on a new power supply which uses Insulated Gate Bipolar Transistor (IGBT) technology now available at the required power levels.

The control circuitry developed for the experimental system functioned with very few difficulties. With the large current being switched by the main power supply there were, of course, some problems with electrical noise. This was most severe in the pulse preservation stage of the controller due to the edge detector circuitry required. Shielding and standard de-coupling techniques reduced this problem to acceptable levels. Planned future development of the system includes the computerization of most of the control system. All of the timing signals for the commutation circuit as well system monitoring could be performed by a central microprocessor. It would then also be possible to incorporate a "user friendly" interface to select the desired operating parameters. However, for the initial experiments carried out on the system, "switch and knob" technology was certainly adequate.

The development of the cooling system presented few challenges. The only serious problem encountered was the presence of some boiling of the cooling water at the lamp. It was at first suggested that this was due to inadequate flow through the head. This turned out ,in fact, not to be the case. Rather, it was a situation where the turbulence in the reservoir caused by the returning water was causing bubbles to be introduced into the system. These bubbles were poor conductors of heat, and when they encountered the temperatures present in the head, localized boiling resulted. This problem was solved with the addition of a simple baffle at the return connection in the reservoir to reduce the turbulence.

In the case of the high voltage system necessary to ignite and sustain the arc lamp, development consisted only of installing a duplicate of an existing system. A future version of the system should use a smaller more efficient switching power supply to perform this task.

The optical bench is another very important component of the system. While it was based on a standard commercially available head, some modifications were required. Due to the high peak powers being delivered to the lamp, high losses were observed at the electrical connections to the head. These connections were basically threaded posts which sealed against the main housing with o-rings, and were attached to the base of the lamp holder. At the highest operating powers, the losses were severe enough to cause heating and, as a result, a softening of the head material. This led to slight leaking of water. This problem was corrected by increasing the diameter of the feedthroughs to decrease the effective resistance.

The front and rear cavity mirrors in the original head were 3/4" in diameter. Due to the availability of substrates for the fabrication of the custom mirrors, modifications were made to the mounts to accommodate 1" diameter optics. These mounts were interchangeable with the originals to maintain the standard wavelength operation. A system of movable optics has since been developed which allows multiple wavelength operation without actually removing the mirror mounts. The system has also now been adapted to accommodate a fibre optic delivery system.

The production of longer wavelength radiation from a Nd:YAG laser has proven to be a significant development. In general, the Nd:YAG laser has become popular as a medical instrument due to its excellent photocoagulative properties. However, it has been considered a poor photovaporizer of tissue. Animal studies based on this experimental laser system, have now shown that the 1.44μm laser source provides greater photoevaporative effects than the 1.06μm Nd:YAG laser. This increase in photovaporation is most likely because there is a relatively strong absorption peak for water at 1.44μm. Currently, a production version of a medical multiwavelength Nd:YAG laser system is being developed, based on the experimental system described in this thesis.

Bibliography

1. W.Koechner, *Solid-State Laser Engineering, 2ed*, Springer-Verlag, 1988

2. A.Kaminskii, *Laser Crystals, 2ed*, Springer-Verlag, 1990

3. J.T.Verdeyen, *Laser Electronics, 2ed*, Prentice Hall, 1989

4. D.Divan, "Synchronous Choppers in High Performance AC/DC Converters", Ph.D. Thesis, University of Calgary, August 1983.

5. J.E.Geusic, H.M.Marcos, L.G.Van Uitert, "Laser Oscillations in Nd-Doped Yttrium Aluminum, Yttrium Gallium and Gadolinium Garnets", *Appl. Phys. Lett.*, vol.4, no.10, pp.182-184, May 1964.

6. J.A.Koningstein, J.E.Geusic, "Energy Levels and Crystal-Field Calculations of Neodymium in Yttrium Aluminum Garnet", *Phys. Rev.*, vol.136, no.3A, pp.711-716, Nov 1964.

7. J.A.Koningstein, "Crystal-Field Studies of Excited States of Trivalent Neodymium in Yttrium Gallium Garnet and Yttrium Aluminum Garnet", *J. Chem. Phys.*, vol.44, no.10, pp.3957-3968, May 1966.

8. A.A.Kaminskii, "Stimulated Radiation from YAG:Nd Crystals", *Sov. Phys. JETP*, vol.24, no.1, pp.33-39, Jan 1967.

9. T.Kushida, H.M.Marcos, J.E.Geusic, "Laser Transition Cross Section Fluorescence Branching Ratio for Nd:YAG", *Phys. Rev.*, vol.167, no.2, pp.289-291,Mar 1968.

10. R.K.Watts, "Branching Ratios for YAG:Nd", *J. Opt. Soc. of Amer.*, vol.61, no.1, pp.123-124, Jan 1971.

11. S.Singh, R.G.Smith, L.G.Van Uitert, "Stimulated-Emission Cross Section Fluorescent Quantum Efficiency of Nd:YAG at Room Temperature", *Phys. Rev. B*, vol.10, no.6, pp.2566-2572, Sep 1974.

12. R.G.Smith, "New Room Temperature CW Laser Transitions in YAG:Nd", *IEEE J. Quantum. Electron.*, vol QE-4 pp. 505-506, Aug 1968.

13. U.Deserno, D.Ross, G.Zeidler, "Quasicontinuous Giant Pulse Emission of $^4F_{3/2}$ to $^4I_{13/2}$ Transition at 1.32 μm in YAG:Nd", *Phys. Lett.*, vol.28A, no.6, pp.422-423, Dec 1968.

14. R.W.Wallace, "Oscillation of the 1.32 μm Line in Nd:YAG", *IEEE J. Quantum.Electron.*, vol QE-7, pp.203-204, May 1971.

15. J.Marling, "1.05-1.44 μm Tunability and Performance of the CW Nd:YAG Laser", *IEEE J. Quantum. Electron.*, vol QE-14, no.1, pp.56-62, Jan 1978.

16. J.Marling, "1.05-1.44 μm Tunable High-Power Laser Emission on 18 CW Transitions in Nd:YAG", *IEEE J. Quantum. Electron.*, vol QE-13, no.9, pp.94D-95D.

17. J.E.Geusic, "Solid-State Maser Research (Optical)", Contract DA-36-039-AMC-02333(E), U.S. Army Electronics Material Agency, Final Report (1965).

18. J.R.Thorton, W.D.Fountain, G.W.Flint, T.G.Crow, "Properties of Neodymium Laser Materials", *Appl. Opt.*, vol.8, no.6, pp.1087-1102, Jun 1969.

19. A.Slack, D.W.Oliver, R.M.Chrenko, S.Roberts, "Optical Absorption of YAG from 10 to 55000 (1/cm) Wave Numbers", *Phys. Rev.*, vol.177, no.3, pp.1308-1314, Jan 1969.

20. M.A.Acharekar, "Spectrophotometric Analysis of Nd:YAG Laser Rods", *Laser Focus*, Nov 1982, pp.63-68.

21. J.Hecht, "The Neodymium Laser", *Lasers and Applications*, Nov 1983, pp.57-62.

22. J.D. Foster, L.M.Osterink, "Thermal Effects in a Nd:YAG Laser", *J. Appl. Phys.*, vol.41, no.9, pp.3656-3663, Aug 1970.

23. W.Koechner, "Thermal Lensing in a Nd:YAG Laser Rod", *Appl. Opt.*, vol.9, no.11, pp.2548-2553, Nov 1970.

24. W.Koechner, "Analytical Model of a CW YAG Laser", *Laser Focus*, Apr 1970,(reprint)

25. E.W.Rapp, "Water Cooling of Lasers: Design Considerations and Techniques", *Lasers and Applications*, March 1985, pp 91-93

26. W.L.Bond, "Measurement of the Refractive Indices of Several Crystals", *J. Appl. Phys.*, vol.36, no.5, pp1674-1677, May 1965.

27. J.F.Ready, *Effects of High-Power Laser Radiation*, Academic Press, 1971.

28. T.Halldorsson, J.Langerholc, L.Senatori, H.Funk, "Thermal Action of Irritation in Biological Material Monitored by Egg-White Coagulation", *Appl. Opt.*, vol.20, no.5, pp.822-825, Mar 1981.

29. A.A.Goosens, "Current Status of the Nd:YAG Medical Laser", *Neodymium-YAG Laser in Medicine and Surgery*, S.N.Joffe, ed., Elsevier Science Publishing Co. Inc., 1983, pp 225-228

30. S.Morden, et.al., "Pulsed Nd:YAG Laser: Study With an Infrared Camera", *Neodymium-YAG Laser in Medicine and Surgery*, S.N.Joffe, ed., Elsevier Science Publishing Co. Inc., 1983, pp 272-276

31. V.A.Fasano,MD, F.Benech,MD, R.M.Ponzio,MD, "Observations on the Simultaneous Use of CO_2 and Nd:YAG Lasers in Neurosurgery", *Lasers in Surgery and Medicine*, vol.2, pp.155-161, 1982.

32. S.K.Davi, "Laser Applications in Microsurgery", *Lasers and Applications*, Oct 1983, pp.73-78.

33. R.Martiniuk, J.A.Bauer, J.D.S.McKean, J.Tulip, B.W.Mielke, "New Long-Wavelength Nd:YAG Laser at 1.44 μm: Effect on Brain", *J. Neurosurg.*, vol.70, pp.249-256, Feb. 1989.

34. J.W.Motto Jr, *Introduction to Solid-State Power Electronics*, Westinghouse Electric Corporation, 1977.